

Development of Reusable, Flexible Electrostatic Lenses for Nanopantography

by
Prithvi Basu

A dissertation submitted to the Department of Electrical and Computer
Engineering,
College of Engineering
in partial fulfillment of the requirements for the degree of

Doctor of Philosophy
in Electrical and Computer Engineering

Chair of Committee: Paul Ruchhoeft
Committee Member: Dmitri Litvinov
Committee Member: Jiming Bao
Committee Member: Vincent M. Donnelly
Committee Member: Demetre J. Economou

University of Houston
August 2020

Copyright 2020, Prithvi Basu

Acknowledgements

I would foremost like to thank my advisor, Dr. Paul Ruchhoeft, for all his guidance and support towards the completion of my Doctorate degree. I would also like to thank my collaborators Dr. Vincent Donnelly, Dr. Demetre Economou, Ryan Sawadichai and Ya Ming for their invaluable advice and help on numerous problems in this project. I would also thank my committee members Dr. Jiming Bao and Dr. Dmitri Litvinov for being a part of my defense committee. I would also like to acknowledge Dr. Long Chang for all of his training and assistance in the cleanroom which formed a core part of this entire work. Finally, I would like to thank my parents: Bhaskar Basu and Shikha Basu for many years of both emotional and financial support.

Abstract

Nanopantography is a method for forming large arrays of nano-sized patterns using a broad beam of ions. In this process, a near-monochromatic ion beam illuminates an array of micron-scale electrostatic lenses, and ions entering each lens converge to a small focal point on the substrate. By tilting the substrate with respect to the ion beam, the spot can be moved across the surface to write a periodic pattern. In a previous demonstration, openings as small as 3 nm in diameter were etched into silicon using a lens array containing 300 nm diameter lenses, creating a fairly straight-forward path to defining nano-scale patterns from much larger structures. Lenses previously consisted of a silicon dioxide dielectric layer sandwiched between a metal lens array and the silicon wafer, and so they were not re-useable, and patterns could only be etched into silicon. To make the system more flexible, we are developing removable and reusable electrostatic lenses that are designed to pattern any conducting surface. Our lenses consist of a free-standing epoxy (SU-8) membrane with etched openings and an electrode on one side. We have successfully etched 30 nm features using removable lenses and carried out simulations that agree with the experimental results. In order to manufacture the lenses, we used the helium atom beam lithography tool to pattern the lens substrates. The helium atom beam lithography tool uses stencil masks for patterning, and manufacturing these stencil masks is another aspect of this project. We are using 250 nm free-standing SU-8 membranes to make lithography masks and at first we are using copper as a hard mask to fabricate these masks. This process involves ion milling of the copper using an argon plasma and this led to an increase in the linewidth of the etched features into SU-8. In order to overcome this challenge, we shifted to using tungsten as a hard mask and the tungsten was reactive ion etched using SF₆ plasma. We have demonstrated that we can form

stencil masks with 50 nm, 75 nm and 100 nm etched openings with tungsten as the hard mask.

Table of Contents

Acknowledgements	iii
Abstract	iv
Table of Contents	vi
List of Figures	vii
Chapter 1 Introduction and Organization	1
Chapter 2 Nanopantography: Parallel Patterning Technique	4
2.1 Introduction and Background	4
2.2 Removable Lens Arrays using Copper as the Hard Mask	12
2.3 Removable Lens Arrays using Tungsten as the Hard Mask	20
2.4 Current Voltage Characterisation of Lens Substrates	23
2.5 Electrostatic Clamping and Capacitance Measurement	28
2.6 Patterning With Removable Lenses and the Lens Model	32
2.7 Conclusion	41
Chapter 3 Atom Beam Lithography Stencil Masks for the Development of Reusable Electrostatic Lenses	46
3.1 Introduction and Background	46
3.1.1 Silicon Nitride Masks	48
3.1.2 Other Notable Works on Stencil Masks	62
3.2 Fabrication of PMMA Stencil Masks	64
3.3 SU-8 Stencil Masks	68
3.3.1 Fabrication of 500 nm SU-8 Stencil Masks	69
3.3.2 Fabrication of 250 nm SU-8 Stencil Masks	73
3.4 Conclusion	90
Chapter 4 Summary and Future Work	94
References	99

List of Figures

Figure 2.1	Schematic diagram of nanopantography principle.	5
Figure 2.2	Schematic diagram of ion assisted plasma etching.	5
Figure 2.3	Schematic diagram of equipotential lines.	6
Figure 2.4	Focusing of ions due to the electrostatic field as a result of the equipotential lines.	6
Figure 2.5	Plot showing the variation of different parameters in a pulsed plasma source.	7
Figure 2.6	Schematic diagram of the ICP source.	9
Figure 2.7	Top down SEM image of a small portion of an array of 650 nm diam lenses, showing 200 nm long trenches taken from [2].	9
Figure 2.8	SEM image of nanotrench 150 nm long and 45 nm deep in 250 nm diameter lenses taken from [2].	10
Figure 2.9	SEM images of T-shaped features with linewidth of 50 nm in 650 nm diameter lenses taken from [2].	10
Figure 2.10	SEM image of 80 nm deep hole in silicon using chlorine plasma etching taken from [4].	12
Figure 2.11	SEM image of 200 nm long trench with 12.5 nm width using chlorine plasma etching taken from [4].	12
Figure 2.12	SEM image of large area UH logos taken from [4].	13
Figure 2.13	SEM image of (a) low magnification (b) high magnification image of the 5 μm cubes etched in SF_6 plasma.	14
Figure 2.14	SEM image of (a) low magnification (b) high magnification image of the 5 μm cubes etched in O_2 plasma.	15
Figure 2.15	Process flow diagram of SU-8 lens using copper as the hard mask.	16
Figure 2.16	SEM image of (a) top down (b) side view image of the 1 μm SU-8 lens openings.	17

Figure 2.17 Effect of mung paste being applied entirely on the back of the substrate.	18
Figure 2.18 Temperature rise of the sample carrier after 30 minutes of ion milling.	19
Figure 2.19 Silicon substrate with mung paste applied entirely on its back.	20
Figure 2.20 Schematic diagram for tungsten and PMMA rate measurement experiment.	21
Figure 2.21 Plot showing (a) the rate of tungsten and PMMA at 30 W in SF ₆ and (b) the selectivity of tungsten and PMMA at 30 W in SF ₆	22
Figure 2.22 Plot showing (a) the rate of tungsten and PMMA at 15 W in SF ₆ and (b) the selectivity of tungsten and PMMA at 15 W in SF ₆	22
Figure 2.23 Schematic diagram showing the (a) experimental set up and (b) circuit diagram of the set up.	24
Figure 2.24 I-V characteristics of an unreleased and un-patterned lens substrate where (a) is sample 1 and (b) is sample 2.	25
Figure 2.25 I-V characteristics of an unreleased and un-patterned lens substrate from 0-100 V and back where (a) is sample 1 and (b) is sample 2.	26
Figure 2.26 Plot showing the stability of an unreleased un-patterned lens sample at 70 V and with changing polarity.	27
Figure 2.27 Schematic diagram for capacitance measurement.	29
Figure 2.28 Plot showing the measured oscilloscope voltage with different known capacitors for different frequency sweeps.	30
Figure 2.29 Schematic diagram of the effect of dust particle between the membrane and substrate.	31
Figure 2.30 Plot showing the change of capacitance with air gap.	32
Figure 2.31 Experimental set up with removable lenses	33

Figure 2.32 SEM image of (a) side view and (b) top view of 100 nm etched features on silicon.	34
Figure 2.33 Schematic of the simulation domain, showing two trajectories of the ions can take to enter a lines in the SimIon domain.	35
Figure 2.34 Histograms of the ions at the base of the lens as a function of lens potential for 1 μm diameter lenses.	42
Figure 2.35 Histograms of the ions at the base of the lens as a function of lens potential for 500 nm diameter lenses.	43
Figure 2.36 Histograms of the ions at the base of the lens as a function of lens potential for 300 nm diameter lenses.	44
Figure 2.37 The FWHM of the images formed by the three lenses as a function of lens potential.	45
Figure 2.38 SEM images of (a)low magnification and (b) high magnification 28 nm etched features on silicon.	45
Figure 3.1 Schematic diagram of the atom beam lithography tool and the actual instrument in the lab.	48
Figure 3.2 Schematic diagram of a stencil mask, taken from [5].	49
Figure 3.3 Fabrication of a grid support stencil mask, taken from [6].	52
Figure 3.4 Diagram of a grid support stencil mask, taken from [6].	53
Figure 3.5 Diagram showing the ion scattering effect through a stencil mask, taken from [7].	54
Figure 3.6 Diagram of the etch profile of GaAs in Cl_2 through a stencil mask, taken from [8].	56
Figure 3.7 Diagram of the etch profile of GaAs in Cl_2 through a stencil mask at a gap of 6 μm , taken from [8].	57
Figure 3.8 SEM image of (a) front side (b) back side of silicon nitride mask showing 700 nm square patterns.	60

Figure 3.9 SEM image of (a) front side (b) back side of silicon nitride mask showing 300 nm square patterns.	61
Figure 3.10 SEM image of (a) front side (b) back side of silicon nitride mask showing 200 nm square patterns.	61
Figure 3.11 Initial flow diagram of PMMA stencil mask fabrication.	65
Figure 3.12 Effect of backscattered electrons on PMMA PMGI bilayer.	66
Figure 3.13 Final flow diagram of PMMA stencil mask fabrication.	67
Figure 3.14 SEM image of (a) front side and (b) back side of a 500 nm PMMA mask showing 200 nm plus sign with an aspect ratio of 4.	68
Figure 3.15 SEM image of (a) front side and (b) back side of a 500 nm PMMA mask showing 300 nm plus sign with an aspect ratio of 4.	68
Figure 3.16 SU-8 mask fabrication process flow using copper as hard mask.	70
Figure 3.17 SEM image of (a) front side and (b) back side of a 500 nm SU-8 mask showing 200 nm plus sign with an aspect ratio of 12 written at a current of 1nA.	71
Figure 3.18 SEM image of (a) front side and (b) back side of a 500 nm SU-8 mask showing 100 nm plus sign with an aspect ratio of 12 written at a current of 10nA.	71
Figure 3.19 SEM image of (a) front side and (b) back side of a 500 nm SU-8 mask showing chiral patterns written at a current of 10nA.	72
Figure 3.20 SEM image of (a) front side and (b) back side of a 500 nm SU-8 mask showing chiral patterns written at a current of 10nA after proper rinsing.	72
Figure 3.21 The (a) front side and (b) back side of 250 nm SU-8 mask showing 100 nm plus sign pattern with aspect ratio of 12.	74
Figure 3.22 The (a) front side and (b) back side of 250 nm SU-8 mask showing 50 nm plus sign pattern with aspect ratio of 4.	74

Figure 3.23	The (a) front side and (b) back side of 250 nm SU-8 mask showing 75 nm plus sign pattern with aspect ratio of 10.	75
Figure 3.24	Printed image of (a) 75 nm plus sign pattern with aspect ratio of 12 and (b) 100 nm plus sign pattern with aspect ratio of 12 using a 250 nm SU-8 mask in the atom beam lithography tool after removing PMMA and evaporating 20 nm gold.	76
Figure 3.25	Diagram showing the formation of blur in helium atom beam proximity lithography.	77
Figure 3.26	SEM image of 100 nm plus sign pattern with aspect ratio of 12 after (a) lithography and development (b) argon milling (c) RIE in oxygen and (d) 100 nm gold evaporation.	78
Figure 3.27	Schematic diagram showing the effect of increase in linewidth by ion milling.	79
Figure 3.28	Flow diagram of SU-8 stencil mask fabrication using tungsten as the hard mask.	79
Figure 3.29	SEM image of (a) chiral patterns after 40 seconds of SF ₆ and (b) 100 nm plus signed patterns after 40 seconds of SF ₆ etch.	80
Figure 3.30	SEM image of (a) chiral patterns after 50 seconds of SF ₆ and (b) 100 nm plus signed patterns after 50 seconds of SF ₆ etch.	81
Figure 3.31	Schematic diagram showing the micromasking effect.	82
Figure 3.32	SEM image of 100 nm plus sign patterns (a) with 1 minute intermediate argon milling step (b) with 30 seconds intermediate argon milling step (c) with 1 minute intermediate argon milling step and tilting the sample and (d) with 30 seconds intermediate argon milling step and tilting the sample.	83

Figure 3.33 SEM image of e beam written and etched (a) 50 nm plus sign patterns with an intermediate argon milling step for 30 seconds (b) 75 nm plus sign patterns with an intermediate argon milling step for 30 seconds and (c) 100 nm plus sign patterns with an intermediate argon milling step for 30 seconds.	84
Figure 3.34 SEM image of front side of SU-8 mask with 700 nm circles tilted at an angle of 30 degrees.	85
Figure 3.35 (a) Rate of PMMA and tungsten in SF ₆ RIE at 15 W (b) Rate of PMMA and tungsten in SF ₆ RIE at 15 W for another set of experiments (c) Selectivity between PMMA and tungsten in SF ₆ RIE at 15 W for (a) (d) Selectivity between PMMA and tungsten in SF ₆ RIE at 15 W for (b).	86
Figure 3.36 Schematic diagram of the step by step process flow demonstrating the SU-8 etch slowdown.	87
Figure 3.37 SEM image of back side of a SU-8 mask with (a) 200 nm circular patterns (b) 300 nm circular patterns.	87
Figure 3.38 SEM image of (a) back side the SU-8 mask with e-beam written 1 μm circles after 500% over-etch into SU-8 (b) back side the SU-8 mask with e beam written 200 nm by 3 μm rectangles after 500% over-etch into SU-8.	89
Figure 3.39 SEM image of (a) etched features showing a second image in high magnification (b) etched features showing a second image in low magnification.	90
Figure 3.40 Schematic diagram of the analysis of the second image formation in the atom beam lithography tool.	91

Figure 3.41 Schematic diagram of the (a) reflected second beam originating from the source in the atom beam lithography tool and (b) one inch aperture blocking the second beam and second image. . . . 92

Figure 3.42 SEM image of (a) printed features in atom beam lithography after shielding the second image in high magnification and (b) in low magnification. 92

Chapter 1

Introduction and Organization

The emphasis and scope of this project deals with nanopantography and helium atom beam lithography as the two techniques for obtaining high resolution patterns in the sub-100 nm regime. Nanopantography is a method for forming nano-sized patterns simultaneously over large areas. In this process, a broad beam of ions is extracted from a source and drifts towards an array of nano-scale electrostatic lenses. When a DC voltage is applied to the lens electrode, the ions entering each lens converge to a small focal point on the substrate and can form nano-scale patterns based on various well-defined experimental parameters. Similarly, helium atom beam proximity lithography is a low cost, high throughput printing technique capable of forming sub-100 nm features in a laboratory with minimal hardware requirements. In this process, a broad beam of atoms (neutrals) is extracted from a source and illuminates a stencil mask on the substrate and replicates the nano-scale stencil mask pattern openings with high fidelity. This dissertation is divided into four major chapters this chapter introduces the project and defines its scope. Chapter 2 and Chapter 3 describes the work done and the challenges associated with nanopantography and helium atom beam lithography process respectively and Chapter 4 summarizes the work and identifies directions.

The scope of Chapter 2 is divided into six subsections. Firstly, a detailed description is given on the principle of nanopantography including the plasma source that generates a mono-energetic ion beam followed by a literature review

about the previous work done with nanopantography with lenses fabricated on the substrates that resulted in sub 10 nm etched features. As our project is about nanopantography with removable and flexible electrostatic lenses, the work involving fabrication and the electrical characteristics of these reusable lenses form the bulk of this chapter. These lenses consisted of free standing membranes of 1 μm thick SU-8 (lens dielectric) supported by an acrylic frame. Two different types of fabrication techniques of the lenses and the challenges associated with them are described using copper and tungsten as hard masks. The electrical breakdown tests of the lens substrates are described and explained, where the breakdown strength of the lens dielectric SU-8 was characterised. The current vs.voltage characteristics of the SU-8 were studied under different experimental conditions. The capacitance between the lens and the substrate was measured and the effect of electrostatic clamping from the capacitance measurements is explained in the next section. Finally, we talk about the patterning with these removable lenses where we were successful in forming 30 nm features with 1 μm diameter lenses and the simulation of lenses with different diameters are also described where we see the simulation results in agreement with the experimental results.

Chapter 3 emphasizes on the helium atom beam lithography and the different types of stencil masks used to implement this technique. Chapter 3 is divided into three subsections where, firstly, we provide a literature review on the work done with different types of stencil masks and an introduction to our helium atom beam lithography tool. Next, the current work within the scope of this project is described where we are explaining the stencil masks fabricated from polymers instead of silicon nitride and silicon. Firstly, the PMMA stencil mask fabrication process is explained along with the simplicity associated with its process flow. The 500 nm thick PMMA masks are also mechanically more robust than the silicon nitride masks of same thickness and these factors give this process an

advantage over the silicon nitride process. However, this process suffers from certain drawbacks, which are explained in detail in this chapter, and hence PMMA stencil masks were abandoned in favor of SU-8 stencil masks even though the PMMA masks showed a lot of promise when this process was developed. We see that 250 nm thick SU-8 stencil masks are as mechanically robust as 500 nm thick PMMA masks and its fabrication using copper as the hard mask first is explained. But this process involves two pattern transfer steps including ion milling into the copper followed by reactive ion etching (RIE) into the SU-8. However the ion milling step produces an increase in the linewidth of the etched openings of around 80 nm and hence, this process is replaced by using tungsten as the hard mask. The fabrication process of the SU-8 stencil masks using tungsten as the hard mask is described next, and the challenges associated with it and the steps taken to overcome those form the remainder of this dissertation. Finally we reach the conclusion that using tungsten as the hard mask is the reliable and robust way to fabricate these lithography stencil masks where we can replicate the patterns faithfully using the helium atom beam proximity lithography equipment. Chapter 4 deals with the future work we plan to execute based on the results and data obtained from the current work of this project.

Chapter 2

Nanopantography: Parallel Patterning Technique

2.1 Introduction and Background

Nanopantography is a patterning method for massively parallel writing of small features over large areas. As seen in [Figure 2.1](#), billions of electrostatic lenses are first fabricated on top of a wafer. A broad-area of mono-energetic ion beam is then directed towards the wafer surface and, by applying an appropriate DC voltage to the lens array with respect to the wafer, the ion beam entering each lens converges to a fine spot focused on the wafer surface that can be several times smaller than the diameter of the lens. By controlling the tilt of the substrate with respect to the ion beam, the focused ion beamlets can write a desired pattern simultaneously in selected areas of the substrate. The physical process involved is ion assisted plasma etching. In such a process an ion bombardment of a surface induces a reaction between the adsorbed etchant and the substrate material to form volatile by-products, as seen in [Figure 2.2](#). In this process the chlorine atoms adsorb on the surface of the silicon substrate and the extracted argon beam strikes the surface of silicon to create dangling bonds which facilitates/induces the etching of the silicon and by forming silicon tetra-chloride as a by-product. In the absence of the argon beam the etch yield of silicon in chlorine is around 0.1 which increases to around 1.3 after the argon bombardment.

Nanopantography has been used to fabricate less than 5 nm sized features in

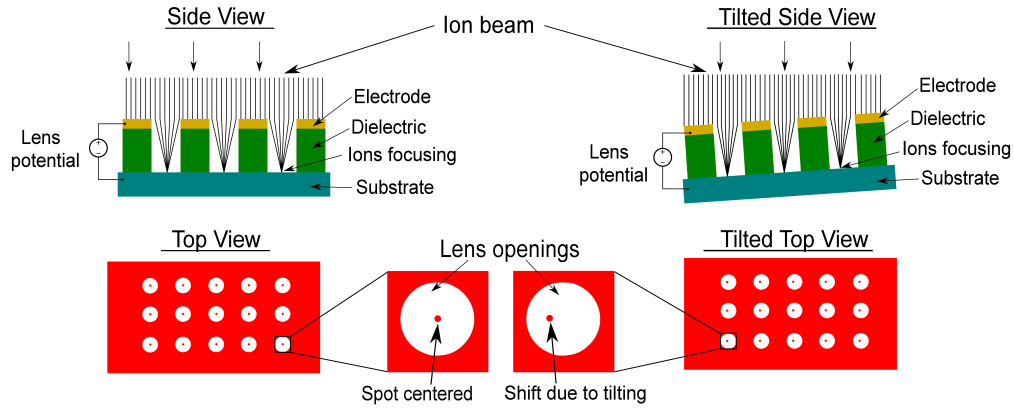


Figure 2.1. Schematic diagram of nanopantography principle.

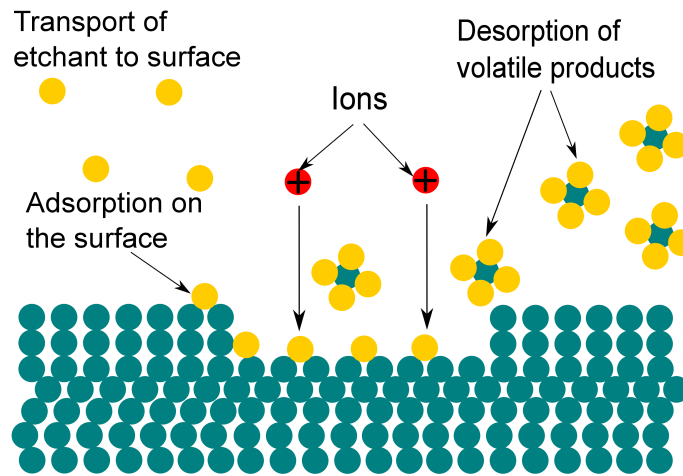


Figure 2.2. Schematic diagram of ion assisted plasma etching.

silicon by exposure to a mono-energetic Ar ion beam and chlorine gas. After the ions are extracted from the source a potential is applied to the lens electrode with respect to the substrate. Once the ions approach the lens electrode, they enter a region consisting of an electrostatic field that is depicted using equipotential lines in [Figure 2.3](#). The ions slow down due to this potential gradient (which is like an energy barrier) of the spherical curvature of the equipotential lines, but, after entering the lens opening, they accelerate and converge to a fine spot at the base of the substrate. The convergence is a result of the electrostatic forces applied by

the electric field, which are in the direction of the gradient of the electrostatic field, and can be visualized by the equipotential lines that form at the lens openings in [Figure 2.4](#).

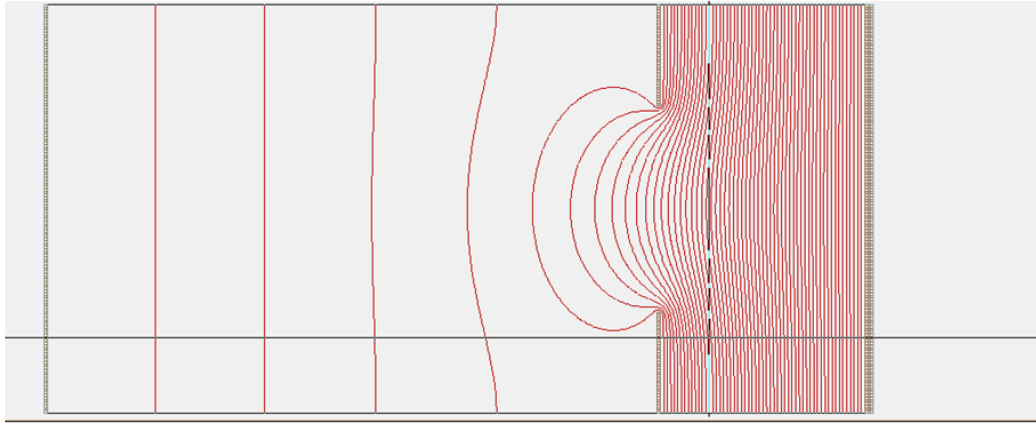


Figure 2.3. Schematic diagram of equipotential lines.

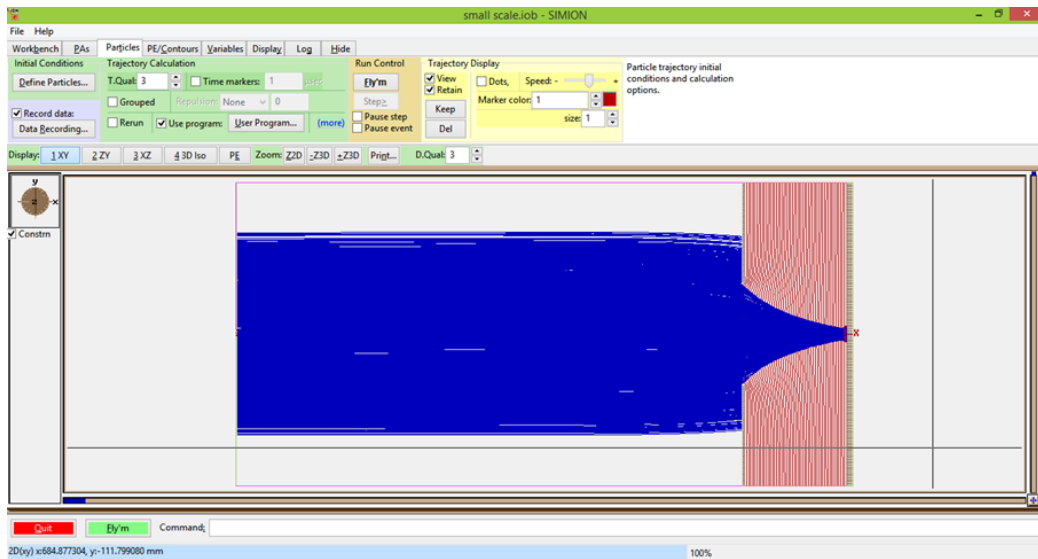


Figure 2.4. Focusing of ions due to the electrostatic field as a result of the equipotential lines.

One of the parameters that determines the size of the spot is the magnification of the lens, which is given by the expression $M = -\frac{S_2}{S_1}$ (ratio of the distance from the lens to the image and the distance of the source to the lens). In our system, where the distance from the lens to the image is $1 \mu\text{m}$ and the distance of the

source to the lens is 70 cm, the magnification is approximately 1.4×10^{-6} . However, in a thin lens model which is an aberration free lens, the angular spread itself is the formation of an image from an extended or finite source size. A finite-sized object results in an image of finite size which is the angular spread of the source. The other parameters that affect the spot size are the chromatic and spherical aberrations. The spherical aberrations are inherent to an electrostatic lens and are a result of the spherical curvature of the equipotential lines that the ions traverse through. The chromatic aberrations are caused by the ion energy spread of the ions. So, obtaining a mono-energetic [1] ion beam is essential to ensure the resolution of the final spot size. Previous work demonstrated that the ion energy distribution scales with the spatial variation in the plasma potential, which in turn scales with the electron temperature.

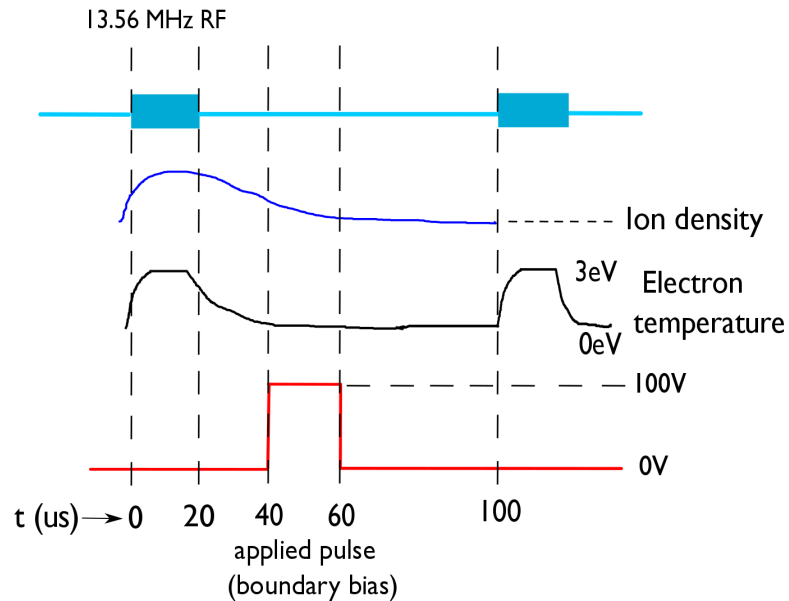


Figure 2.5. Plot showing the variation of different parameters in a pulsed plasma source.

As shown in [Figure 2.5](#) which plots the RF power, the ion density, the electron temperature and the applied boundary bias (pulse), we understand the reduction of the ion energy spread which is necessary to reduce chromatic aberrations.

For the first 20 μs , the RF power (13.56 MHz) is applied to a coil around the quartz reactor, and the plasma ignites, as is shown in the first 20 μs . The ion density and the electron temperature increase during the active glow period of the plasma, which is shown in the next two plots. The electron temperature rises because the average kinetic energy of the electrons increases. A potential is applied to the boundary electrode 20 μs after the RF power is turned off, in the late afterglow, when the plasma cools down substantially. As a result of this the electron temperature drops as the high velocity electrons leave the plasma. However, the ion density also drops in the late afterglow, which is a slow process compared to the plasma cooling, so that lowering the ion energy distribution results in a small reduction of ion current. Thus the ions are extracted in the late afterglow of the plasma when the electron temperature drops and a nearly mono-energetic ion beam is extracted. [Figure 2.6](#) shows the schematic diagram of the ICP source from where the mono-energetic ion beam is extracted. In the figure, we see an inductive coil around the plasma reactor where the RF power is applied to ignite the plasma and the applied pulse on the boundary electrode to extract the mono-energetic ion beam as shown

In one of the previous works, a lens arrays consisted of a 150 nm thick Al layer on a 1000 nm thick thermal SiO_2 on a heavily-doped Si substrate. Each sample contained 200, 250, 300, 350, and 650 nm diameter lens openings. The substrate was at ground potential and the optimal ion-focusing voltage on the top electrode was obtained by ion trajectory simulations and through experiments. An argon beam with ion energy of 100 eV and a Cl_2 beam with a Cl_2/Ar flux ratio of 100:1 were used. The etch rate of Si is 1.3 Si atoms per Ar^+ under these conditions. In contrast, the sputtering rate without Cl_2 is much slower with 0.1 Si atoms per Ar^+ with an ion energy of 100 eV, and Cl_2 gas does not react with Si at room temperature. After etching, samples were examined under the scanning

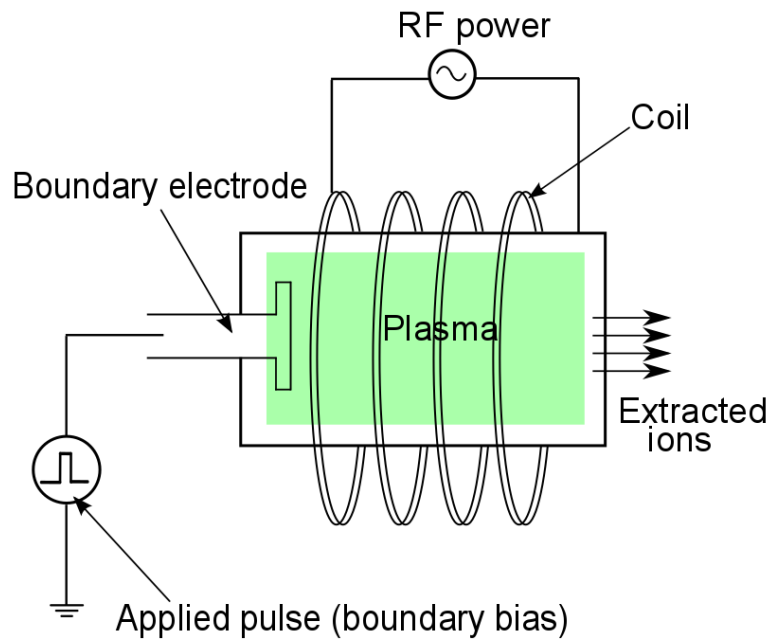


Figure 2.6. Schematic diagram of the ICP source.

electron microscope(SEM). V-shaped nanotrenches were formed in Si by tilting the lens array in one direction with respect to the substrate using a dwell time of 10 minutes at each angle.

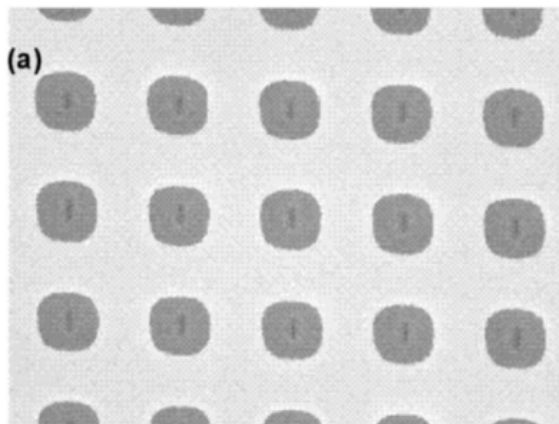


Figure 2.7. Top down SEM image of a small portion of an array of 650 nm diam lenses, showing 200 nm long trenches taken from [2].

Figure 2.7 is a top-down SEM image of a small portion of an array of 650 nm diameter lenses, showing 200 nm long trenches etched across the center of each

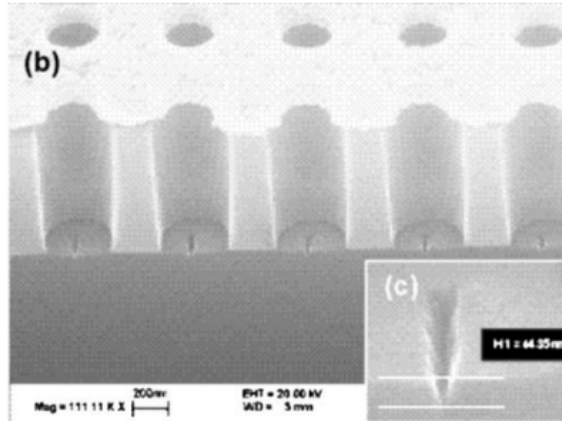


Figure 2.8. SEM image of nanotrench 150 nm long and 45 nm deep in 250 nm diameter lenses taken from [2].

lens base [2]. Figure 2.8 show a cleaved edge of a portion of 250 nm diameter lenses. Each lens produced a nanotrench 150 nm long and 45 nm deep, and widths of 30 nm at the top and 15 nm FWHM[2]. The feature sidewall is straight and somewhat tapered, with an angle of 18 °with respect to the surface normal. The line width did not vary along the length of the trench. Similarly, T-shaped features with top line-width of 50 nm in 650 nm diameter lenses were etched into Si, using a shorter dwell time 2.5 min at each point as seen in Figure 2.9[2].

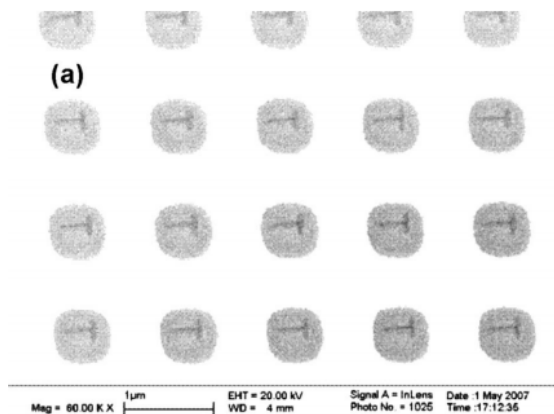


Figure 2.9. SEM images of T-shaped features with linewidth of 50 nm in 650 nm diameter lenses taken from [2].

In another publication, electrostatic lenses were fabricated on a Si substrate[3].

A 150 nm sputter deposited Al layer was separated from the p-Si substrate by 1000 nm of thermally grown oxide. The metal-oxide-silicon structure comprised of an electrostatic lens that focused the ion beamlets entering the structure. The lenses used in this work had a diameter of 650 nm and a focal length of 1150 nm. The lens array had a total of 7.5×10^6 lenses. Si substrates patterned with the electrostatic lens arrays were loaded into the nanopantography processing chamber and electrically connected to ground, while the Al layer on top was DC biased with the focusing voltage of 96.8 V with the measured ion energy of 107 eV. After chlorine plasma etching for 7 minutes, using the parameter values given above, the hole was 80 nm deep, while the rest of Si surface was masked by the native oxide. [Figure 2.10\[4\]](#) shows the SEM image of 80 nm deep hole in silicon using chlorine plasma etching. Lines were also written by nanopantography, using the optimum focusing voltage of 96.8 V and a 50 seconds dwell time per exposure step. The exposure step size was 3.4 nm. The equivalent writing speed is 4.1 nm/min. A 200 nm long trench with 12.5 nm width was obtained using chlorine plasma etching after nanopantography patterning as shown in [Figure 2.11\[4\]](#). The depth of the Si trench was 80 nm.

Also 'UH' logos were written over $225 \text{ nm} \times 250 \text{ nm}$ areas with an exposure step size of 3.4 nm and etch time of 50 seconds, as shown in [Figure 2.12\[4\]](#). The thinnest line near the crossing point of the right vertical line of letter 'U' and the horizontal line of letter 'H' is 13 nm wide. Instead of etching a 100 nm deep feature in Si, only a 1–2 nm of SiO_2 needed to be removed, and this reduced the nanopantography process time from 30 minutes to 50 seconds. However the main issue with these works were that the lenses weren't reusable, that is the lenses were fabricated on the silicon substrate directly and nanopantography was carried out on the silicon substrates. In the next sections of this chapter we will see the application of reusable lenses in nanopantography.

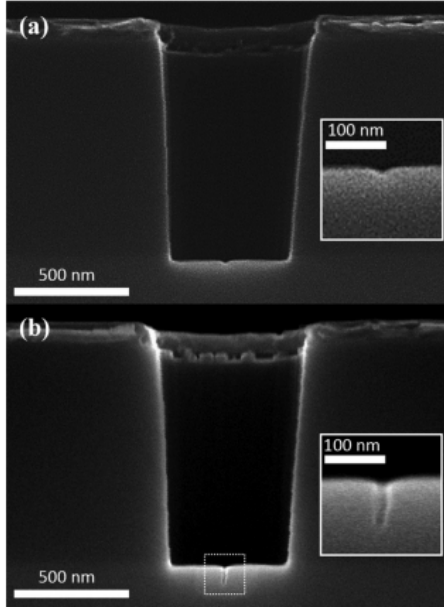


Figure 2.10. SEM image of 80 nm deep hole in silicon using chlorine plasma etching taken from [4].

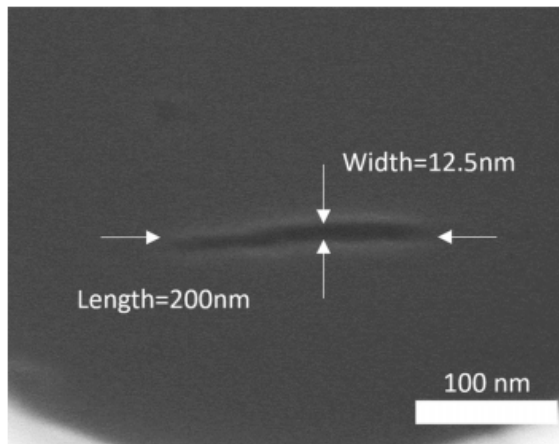


Figure 2.11. SEM image of 200 nm long trench with 12.5 nm width using chlorine plasma etching taken from [4].

2.2 Removable Lens Arrays using Copper as the Hard Mask

The previous section described the nanopantography patterning with electrostatic lenses fabricated on the silicon substrate directly. In this current work, we are fabricating re-usable electrostatic lenses and the substrate other than silicon

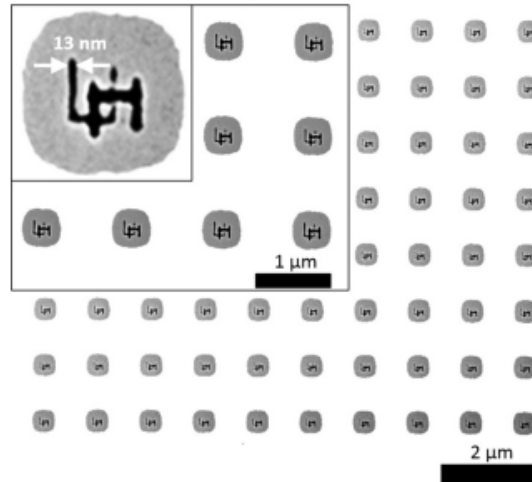


Figure 2.12. SEM image of large area UH logos taken from [4].

can be used. Removable lenses consist of free-standing membranes made from a dielectric which has a high enough dielectric breakdown strength to withstand the applied lens potentials. We chose SU-8 as the lens dielectric over other polymers such as PMMA and PMGI because SU-8 has a theoretical breakdown strength of $120 \text{ V}/\mu\text{m}$. We first investigated the etching of SU-8 using SF_6 plasma. This was done because copper was chosen as the hard mask and the selectivity between SU-8 and copper in SF_6 was found to be at least 70 from previous work involving silicon nitride etching in SF_6 . In order to investigate the etch profile of SU-8 using SF_6 , a three inch polished silicon wafer was coated with $5 \mu\text{m}$ of SU-8 and 80 nm of copper as the hard mask. In this process 200 nm of PMMA was spin-coated on the entire stack and $5 \mu\text{m}$ squares were exposed by atom beam lithography (ABL). The purpose was to form $5 \mu\text{m}$ SU-8 cubes and inspect the sidewalls of the etched features in the SEM. The first pattern transfer step consisted of milling the 80 nm copper using Ar^+ beam at a beam energy of 600 V and current of 120 mA . The milling rate of copper and PMMA were $30 \text{ nm}/\text{min}$ and $35 \text{ nm}/\text{min}$, respectively. The next pattern transfer step involved etching the patterns into the $5 \mu\text{m}$ SU-8 using SF_6 RIE at a pressure of 1 mTorr and power of 30 W . The DC bias potential

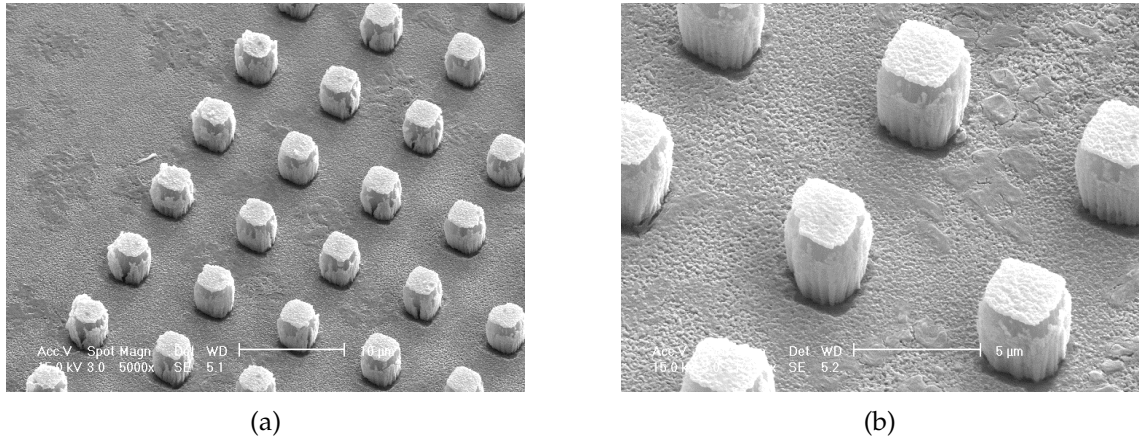


Figure 2.13. SEM image of (a) low magnification (b) high magnification image of the 5 μm cubes etched in SF₆ plasma.

was 220 V.

From [Figure 2.13\(a\)](#) and (b) we see that there is a deposition on the sidewalls (which we hypothesize to be sulphur) and the sidewalls are not straight implying that the use of SF₆ requires more development when it comes to forming straight sidewalls of SU-8. Oxygen RIE was the other choice of etchant and the entire process was carried out except that the final pattern transfer step involved an oxygen RIE into the SU-8. The selectivity between SU-8 and copper in oxygen was found to be around 17 and the results showed mask failure. However, on conditioning the RIE chamber with 1 mTorr SF₆ at 220 V and 30 watts for a couple of hours and running the entire process using oxygen RIE showed that the sidewalls of the cubes were straight and there were not any mask failures as well as seen in the SEM images in [Figure 2.14\(a\)](#) and (b). The selectivity between SU-8 and copper in oxygen after SF₆ conditioning was measured to be greater than 50 which justified the observation of not having any mask failures.

The first lens fabrication process involved making removable and reusable lenses. The lens fabrication sequence as seen in [Figure 2.15](#) consisted of coating a three-inch polished silicon wafer with a release layer PMGI, a one micron thick

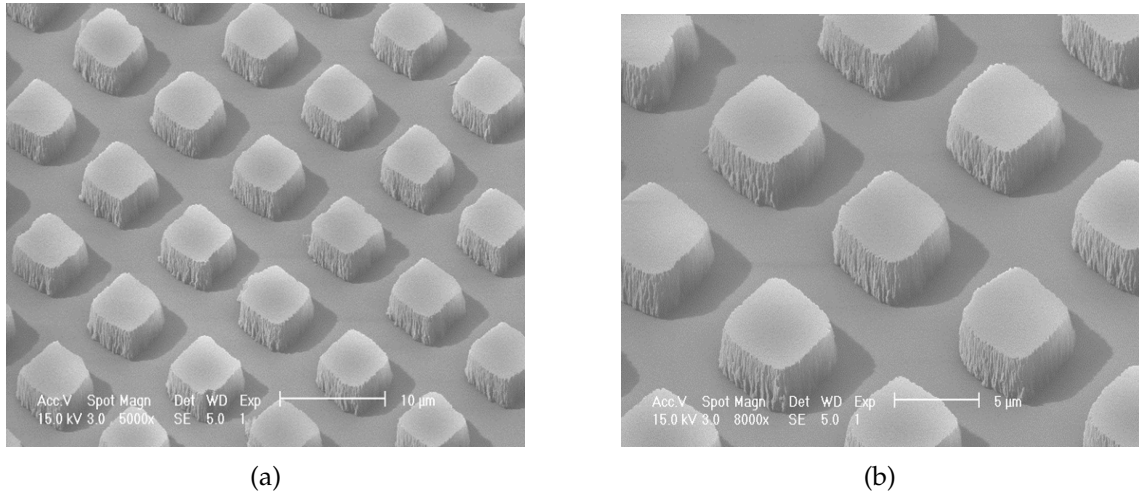


Figure 2.14. SEM image of (a) low magnification (b) high magnification image of the 5 μm cubes etched in O_2 plasma.

SU-8 layer (lens dielectric), 30 nm of copper, 30 nm of gold (lens electrode) and 100 nm PMMA as the resist (imaging layer). The thickness of the PMMA is limited by the fact that we are using the helium atom beam lithography tool to print the features. Therefore, the selectivity between milling of the copper, gold and PMMA is one of the key factors that would determine the feasibility of this process. The first step consists of patterning the PMMA (lithographic step) followed the development of the resist. An laser-cut acrylic frame was bonded on the substrate prior to the pattern transfer steps. After that the patterns were transferred into the copper and gold by an ion milling step in argon plasma and further etched into SU-8 (reactive ion etching) in an oxygen plasma. The reason for having copper as the hard mask is that the selectivity between copper and SU-8 was around 70 in the oxygen RIE after SF_6 conditioning of the RIE chamber. Also the selectivity between the PMMA and the copper and gold was roughly 1:1 in the ion milling system. The selectivity between gold and SU-8 in oxygen RIE, was however, around 17 signifying that gold cannot be used as the hard mask. The sputter rate of gold in oxygen RIE was measured to be around 4 nm/min, as opposed to approximately

1 nm/min for copper after SF₆ conditioning. After the pattern transfer is complete the free standing SU-8 membrane supported by an acrylic frame was released by dissolving the PMGI in TMAH solution. The membrane area was 0.7x0.7 cm² and the patterned area is 1 mm². The lens array patterns were formed using atom beam lithography (ABL) which is described in the next chapter.

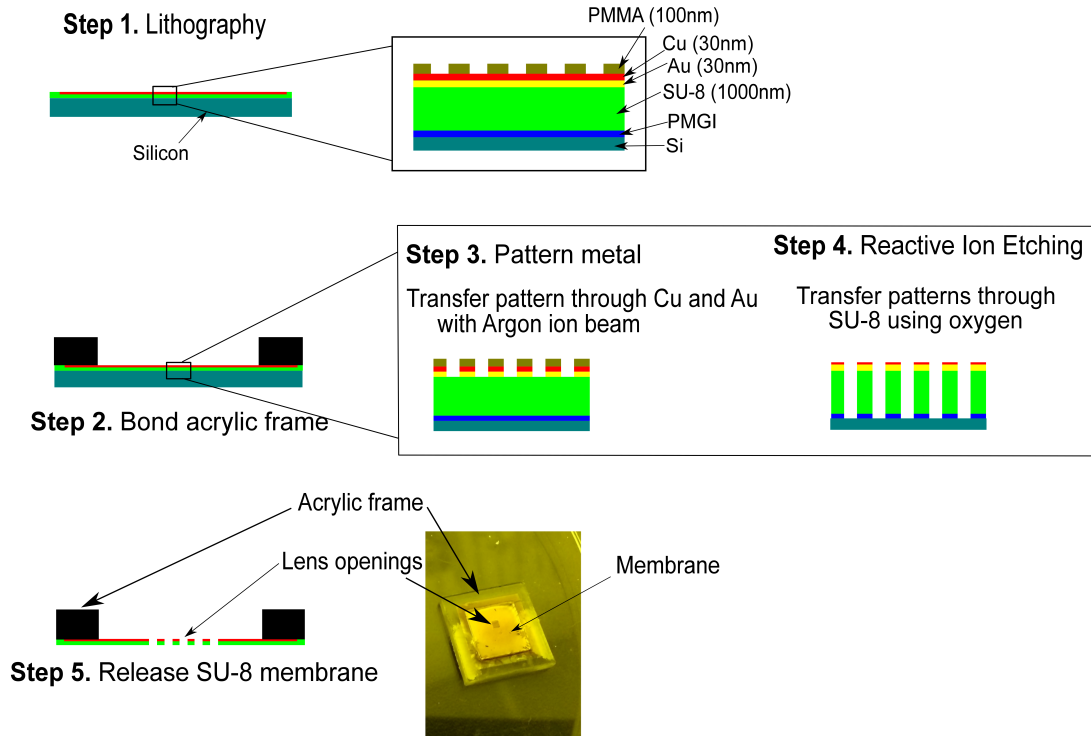


Figure 2.15. Process flow diagram of SU-8 lens using copper as the hard mask.

The SEM images of the top down and side view of the lenses are shown in [Figure 2.16\(a\)](#) and [\(b\)](#) respectively, where the lens openings in these images are 1 μm in diameter and the side view images clearly depict the straight sidewalls with the oxygen RIE into the SU-8. However, we observed that the ion milling step increased the size of the features by around 80 nm by carrying out certain experiments described in Chapter 3. The major issue with the etched patterns was the increase in the size of the features. The hypothesis was that the sample

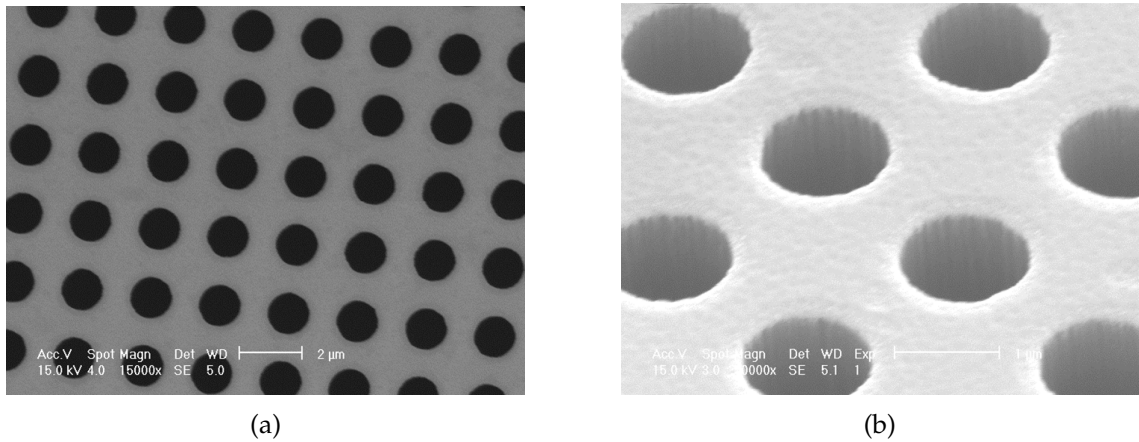


Figure 2.16. SEM image of (a) top down (b) side view image of the 1 μm SU-8 lens openings.

overheats during the ion milling step, causing the PMMA to reflow. The rise in temperature could have been due to the radiation from the neutralizer filament or from the ion beam itself. Some test experiments were carried out to detect the cause of the temperature rise of the sample.

A three inch wafer was used to test the temperature rise in the ion mill. The wafer was applied with mung paste only at one small spot on its back to replicate the method used in the mask and lens fab process. A temperature sensitive sticker was attached to the back of the wafer that could record the highest temperature between in the range of 88 °C to 140 °C. The temperature observed in the temperature sticker after the ion source was on for 5 minutes with the neutralizer filament on along with 80 seconds of Ar mill was 120 °C. The temperature with the ion source on for 5 minutes with the neutralizer filament off and 80 seconds of Ar mill was 138 °C. This indicated that the neutralizer filament did not contribute to the rise in temperature. The temperature with the ion source on for 5 minutes with the neutralizer filament on was less than 88 °C. The temperature with the ion source on for 5 minutes with the neutralizer filament off was less than 88 °C. The temperature with the ion source on for 1 minute with the neutralizer filament off and 80 seconds of Ar mill was 110 °C. From these

experiments we initially concluded that the temperature rise is due to the ion beam extracted from the source and not due to the neutralizer filament. In order to inspect that we used silicone based mung paste entirely on the back of the silicon substrate (as opposed to only one small spot) to improve thermal conductivity between the substrate and the stainless steel sample carrier. Figure 2.17 shows the effect of mung paste being applied entirely on the back of the substrate. The sample carrier, has an uneven surface, and if the mung paste is not applied entirely on the back of the substrate but only at a small spot on the substrate there are gaps/voids between some parts of the substrate and some parts of the sample carrier. However, if the mung paste is applied entirely on the back of the substrate there are not any gaps and the mung paste fills the gaps and voids which would have been there otherwise.

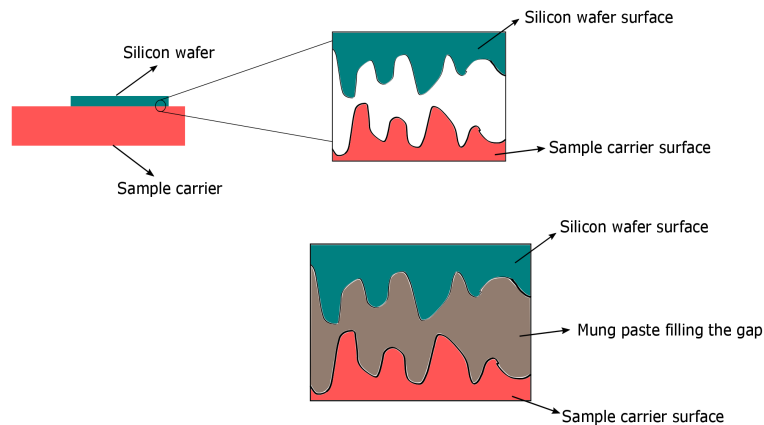


Figure 2.17. Effect of mung paste being applied entirely on the back of the substrate.

We calculated temperature rise based on the specific heat capacity and density of stainless steel (for the sample carrier) and the volume of the sample carrier. The rise in temperature for an ion milling time of 1 minute was calculated to be less than 1 °C for just the sample carrier (without any substrate on it), indicating that the sample carrier does not get heated during the one minute ion milling time. On applying the mung paste entirely on the back of the silicon substrate,

calculations were carried out for an estimated mung paste thickness of 1 mm. The rise in temperature of the silicon substrate was computed to be around 0.01 °C, implying that the rise in temperature of the substrate with mung paste entirely on its back is negligible. Therefore the increase in the size of the patterns isn't due to the reflow of the PMMA due to overheating in the milling step. This reason is explained in Chapter 3. [Figure 2.18](#) and [Figure 2.19](#) show the temperature rise of sample carrier after 30 minutes of ion milling and picture of the silicon substrate with mung paste applied entirely on its back respectively. From [Figure 2.18](#) we see that the temperature rise of the sample carrier is only around 49 °C as measured with temperature stickers.

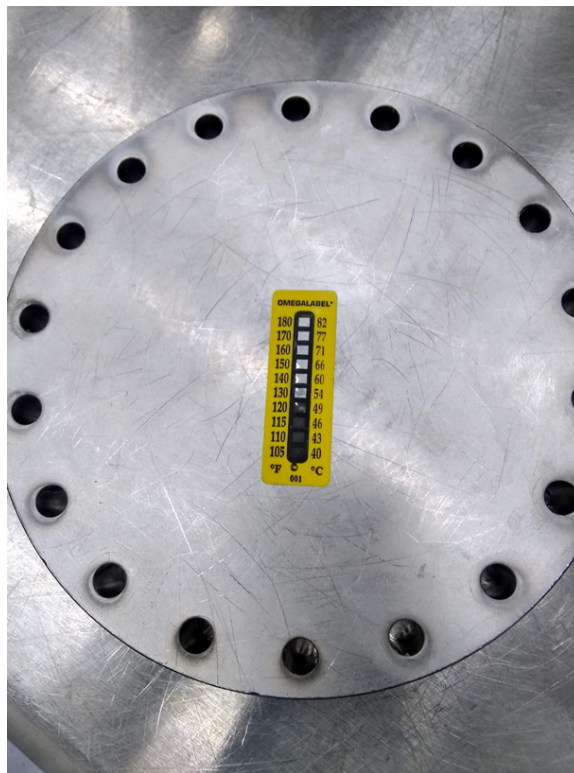


Figure 2.18. Temperature rise of the sample carrier after 30 minutes of ion milling.

With this process using copper as the hard mask we were making lenses reliably although there were yield issues associated with the release of the membrane. However, after weeks of fabrication runs that had very poor yield, we



Figure 2.19. Silicon substrate with mung paste applied entirely on its back.

noticed that the PMMA rates in the argon mill had increased from 35 nm/min to around 60 nm/min indicating the selectivity between copper and PMMA was no longer 1:1. We hypothesized that it was due to excessive water vapour and humidity that caused the PMMA rates to increase and tried several experiments such as baking the sample on the hot plate and leaving the sample pumping in the vacuum overnight. All these experiments did reduce the PMMA rate to around 45 to 50 nm/min but still left behind an unreliable and low yield process.

2.3 Removable Lens Arrays using Tungsten as the Hard Mask

Due to the drawback of the ion milling process, where the PMMA rates had increased as explained in the previous section, tungsten was chosen as the electrode. The purpose of using tungsten was to eliminate the ion milling process and to employ two RIE steps in the lens fabrication process. The new lens fabrication sequence consisted of coating a 3 inch polished silicon wafer with a release layer PMGI, a one micron thick SU-8 layer (lens dielectric), 30 nm of tungsten and

100 nm PMMA as the resist (imaging layer). The first step consisted of patterning the PMMA (lithographic step) followed the development of the resist. A laser cut acrylic frame was bonded on the substrate prior to the pattern transfer steps. After that the patterns were transferred into the tungsten by a reactive ion etch step in SF₆ plasma and further etched into SU-8 (reactive ion etching) in an oxygen plasma.

In order to correctly estimate the etch rate of tungsten and selectivity between tungsten and PMMA and tungsten and SU-8 a series of experiments was carried out at different power settings. [Figure 2.20](#) shows the schematic diagram for tungsten and PMMA rate measurement experiment. In this diagram X_{p1} is the initial thickness of the PMMA and X_{p2} is the thickness of PMMA left after etching for a certain length of time in SF₆. Similarly, X_w is the initial thickness of the tungsten sputtered on a sample of PMMA having X_{p1} thickness on a silicon substrate. X_{p3} is the thickness of the PMMA left after etching this sample in SF₆ for a certain length of time. the time to etch both the samples is T seconds and the PMMA rate is R_{PMMA} . The time to reach thickness X_{p3} in first sample is T_1 seconds and the time to etch the tungsten is calculated to be $T_w = T - T_1$ seconds. The tungsten rate is calculated to be $R_w = \frac{X_w}{T_w}$. Based on the calculations shown above a series of experiments were carried out with these two different samples and a certain set were etched in SF₆ at 15 W and 30 W respectively. The pressure of the SF₆ was fixed at 1 mTorr.

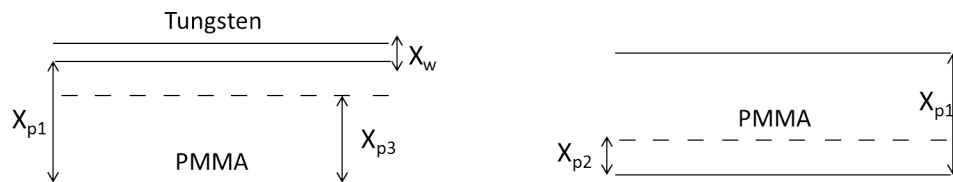
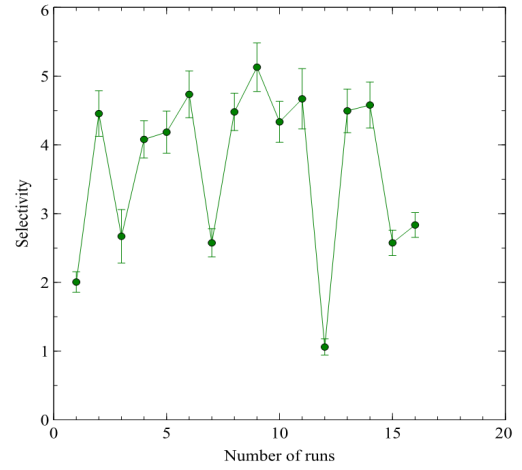
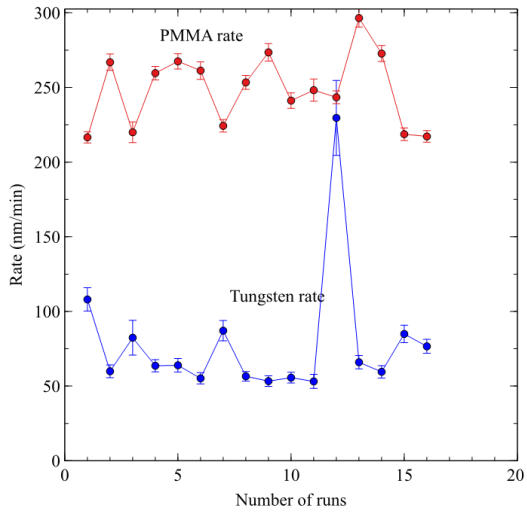


Figure 2.20. Schematic diagram for tungsten and PMMA rate measurement experiment.

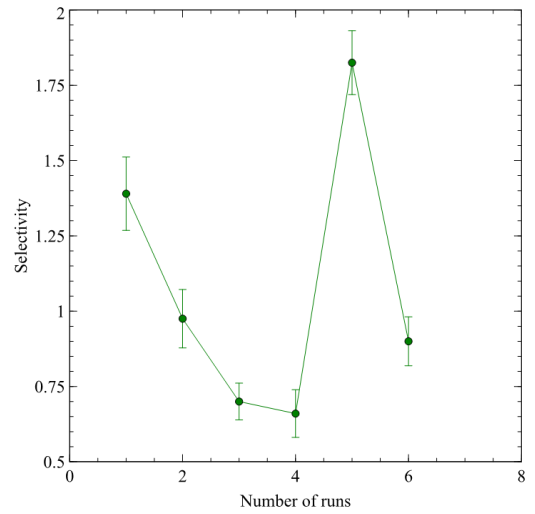
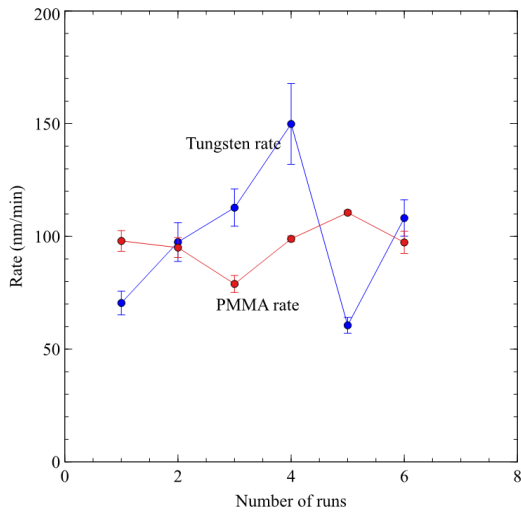
From [Figure 2.21](#)(a) and (b), we see that the selectivity between PMMA and



(a)

(b)

Figure 2.21. Plot showing (a) the rate of tungsten and PMMA at 30 W in SF₆ and (b) the selectivity of tungsten and PMMA at 30 W in SF₆.



(a)

(b)

Figure 2.22. Plot showing (a) the rate of tungsten and PMMA at 15 W in SF₆ and (b) the selectivity of tungsten and PMMA at 15 W in SF₆.

tungsten varies between 2 and 5, whereas, from [Figure 2.22\(a\)](#) and (b), we see that the selectivity does not exceed 2. This is because the PMMA rates at 30 W power is significantly greater than at 15 W power. Based on this experiment we concluded to etch the tungsten in SF₆ at 15 W power. The stencil mask process with tungsten as the hard mask also takes into account this data analysis as explained in Chapter 3. The selectivity between tungsten and SU-8 is around 240 in the oxygen RIE. After the pattern transfer is complete the free standing SU-8 membrane supported by an acrylic frame is released by dissolving the PMGI in TMAH solution. Therefore, if we want to make lenses reliably, using tungsten as the hard mask and the lens electrode could be an alternative because it gives the necessary selectivity required to faithfully transfer the patterns in the two steps and also eliminates the ion milling step which suffers from the drawback of the increment in linewidth as explained in Chapter 3.

2.4 Current Voltage Characterisation of Lens Substrates

In order to carry out nanopantography, it was essential to test the breakdown voltage of the lens dielectric SU-8. The reason we looked is that is because our original plan was to first test these lenses on the substrate before releasing them to use as membranes. Since we were applying voltages of nearly 100 V on these samples and theoretically SU-8 has a breakdown strength of 100 V per μm , SU-8 was chosen as the lens dielectric. In this set of experiments the samples were set up as shown in [Figure 2.23\(a\)](#) and [Figure 2.23\(b\)](#), which show the circuit diagram of the set up with the individual resistances of the components. In the circuit diagram, R_1 is the contact resistance of the gold electrode, R_2 is the resistance of the gold electrode, R_3 is the resistance of the SU-8 dielectric, R_4 is the contact resistance of the silicon and R_5 is the resistance of the silicon substrate. The acrylic

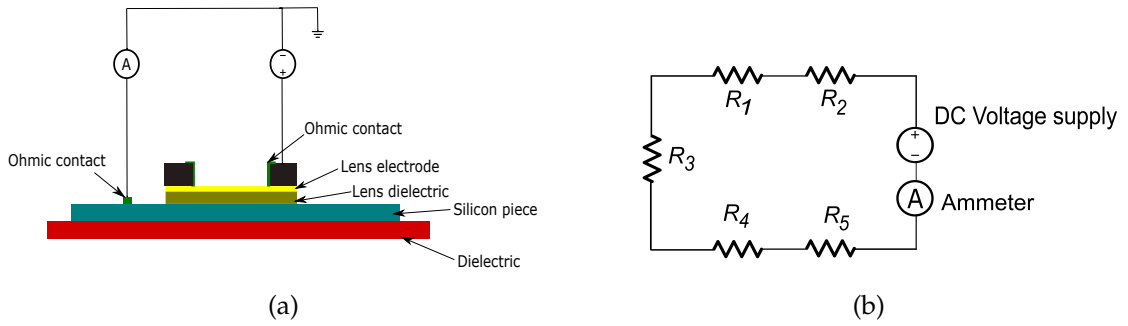


Figure 2.23. Schematic diagram showing the (a) experimental set up and (b) circuit diagram of the set up.

frame supporting the membrane was painted with silver paste and the silver paste was extended along the sidewall of the frame to the center of the membrane containing the gold electrode to make proper ohmic contact. The resistance of the gold electrode was consistently measured to be around 10 ohms and the resistance of the dielectric was measured to be around 3 to 4 M Ω and the silicon resistance was measured to be around 5 to 10 K Ω . These numbers varied with each measurement but these aforementioned resistance values were more or less consistent.

In the experiment a voltage was applied on the ohmic contact made on the frame of the lens substrate and the current was monitored. At first, few blank lens substrates were tested (not released as membranes) while ramping up the voltage from 0 to 100 V using a Keithley source meter. The samples consisted of a silicon wafer piece with PMGI as release layer, followed by 1 μm of SU-8 (lens dielectric) and 30 nm of gold as the electrode. A laser-cut acrylic frame was bonded on the stack and the experiments were carried out. From the I-V characteristics as seen in [Figure 2.24\(a\)](#), we see that on applying the voltage until 50 V the current was negligible or less than 0.25 mA. After 50 V, the current increased rapidly to 2 mA and gradually increased to 2.5 mA until we applied 100 V on the substrate. The resistance was computed to be 30 K Ω from the slope of the straight line through

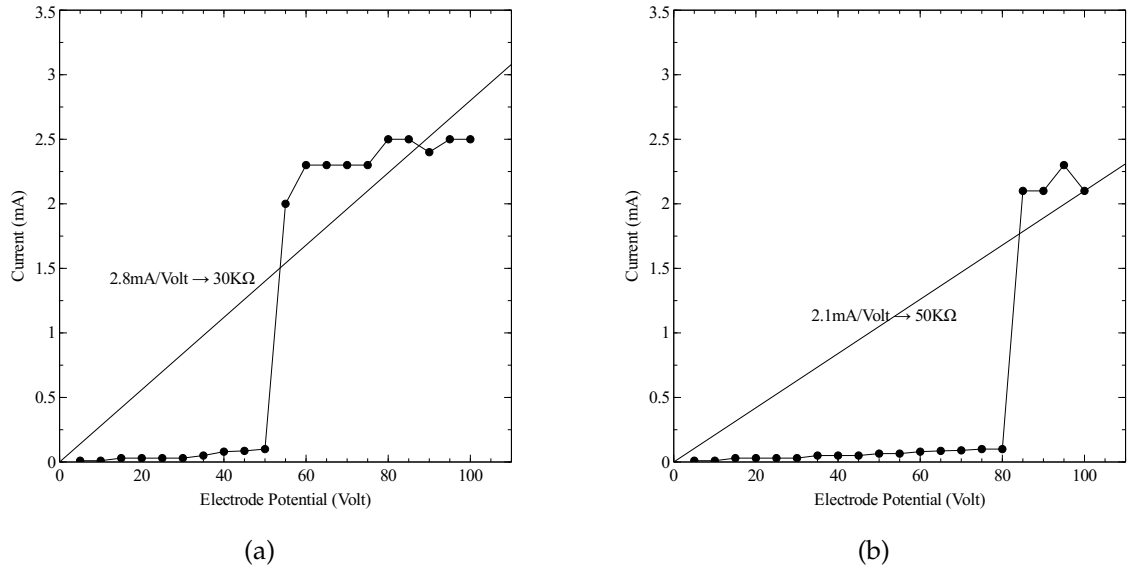


Figure 2.24. I-V characteristics of an unreleased and un-patterned lens substrate where (a) is sample 1 and (b) is sample 2.

the origin. From [Figure 2.24\(b\)](#) we see that on applying the voltage until 80 V, the current was negligible or less than 0.2 mA. After 80 V, the current shot up to 2 mA and gradually remained consistent at 2 mA until we applied 100 V on the substrate. The resistance was computed to be 50 KΩ from the slope of the straight line through the origin.

In [Figure 2.25\(a\)](#), the voltage was increased from 0 to 100 V and swept back to 0 V, as shown in the plot by increasing and decreasing potential data points. There were two sets of voltage sweeps on that particular sample and the current gradually increases to around 2 μA at 80 V and further increases to 5-6 μA at 100 V. When the voltage is swept back to 0 V the current values more or less follow the same path with identical magnitudes for each of the corresponding voltage data point. We can say that this plot resembles the I-V characteristic of a diode. In [Figure 2.25\(b\)](#) we see a completely different trend however. There were two sweeps from 0 to 100 V and back to 0 V as shown in the plot with two different colors. For the plot in black, we see that the current was almost

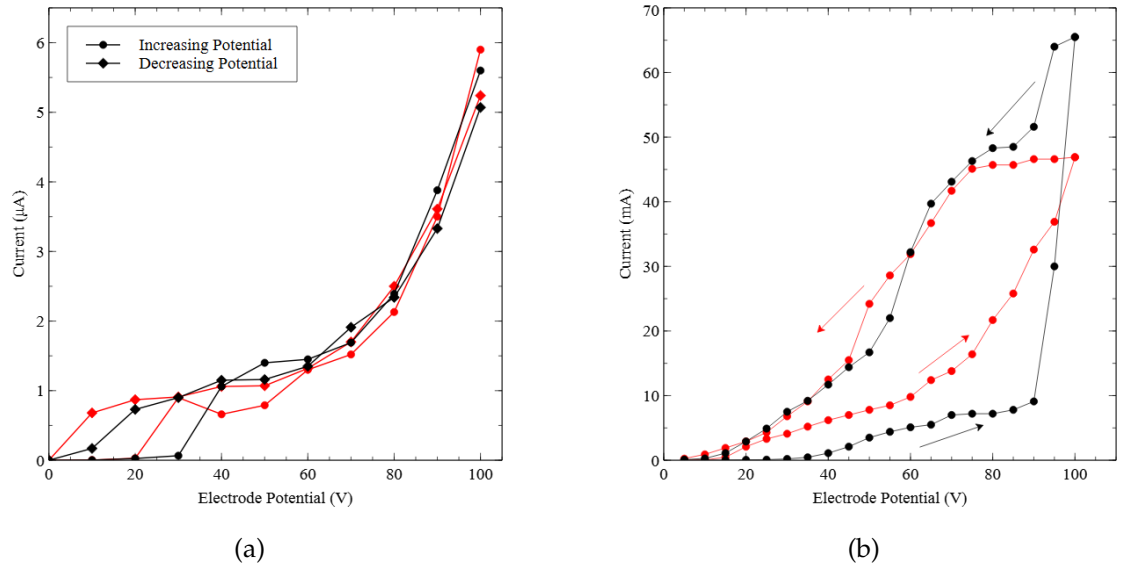


Figure 2.25. I-V characteristics of an unreleased and un-patterned lens substrate from 0-100 V and back where (a) is sample 1 and (b) is sample 2.

negligible until 40 V and it gradually increased to 10 mA at 90 V and then shot up to 70 mA at 100 V, signifying that a breakdown occurred at around 90 V. When the voltage was swept back from 100 to 0 V we see that the current values are much higher than what it was when going forward from 0 to 100 V. The plot resembles a hysteresis loop where we see high current values in the reverse direction than in the forward direction. Even the plot in red for the second sweep on the same sample follows the identical trend of a hysteresis loop where the values of current are higher in the reverse direction. From the two plots in Figure 2.25(a) and (b), we can conclude that the trends are different and the breakdown in Figure 2.25(b) is related to having defects in the dielectric and there are yield issues stemming from the fabrication steps.

Figure 2.26 shows a plot of a particular experiment that was carried out to test the stability of an unreleased lens substrate. The x-axis shows the number of hours up to which the sample was tested for while fixing the potential at 70 V. The positive potential result shows how the current varies at a fixed positive potential

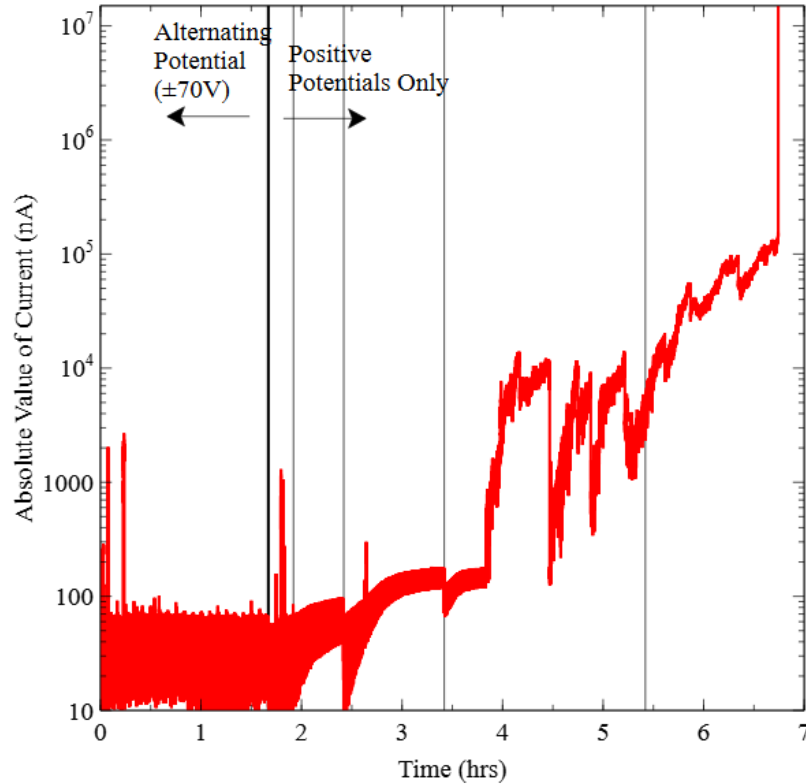


Figure 2.26. Plot showing the stability of an unreleased un-patterned lens sample at 70 V and with changing polarity.

of 70 V. The alternating potential shows the variation of current while the polarity was reversed. For the positive potentials the sample was kept at 70 V for 5 hours (from 2 to 7 hours). The current gradually increased for this sample to 100 μA after four and a half hours (6.5 hours in the plot). The current gradually increases to 100 nA in the first couple of hours and then to 100 μA in the next couple of hours. Finally it shoots up to 10 mA in the fifth hour. This experiment implied that this particular sample was defect free and it did withstand 70 V for 4 hours with negligible increase in current. The alternating potential was applied for 2 hours only and the current remained constant at 100 nA for those 2 hours. So on changing the polarity the movement of the charge carriers in the dielectric are altered in such a way that the resistance of the dielectric does not vary significantly.

After carrying out a number of experiments described above with unreleased

lens substrates, we concluded that there were yield issues associated with the lenses fabricated on the substrate. The substrates with higher defects showed breakdown below 100 V, and on sweeping back the voltage to 0 V, the current remained higher when compared to the forward voltage sweep indicating that they did not behave like a perfect resistor. Therefore we started carrying out the current voltage characteristics on 1 μm thick SU-8 released membranes. The I-V characteristics of two separate 1 μm thick SU-8 membranes showed that the current does not exceed 50 nA even after applying a potential of 150 V. The reason why the membranes had a lower leakage current was that they did not make 100% contact with the substrate and hence many of the defected areas on the membrane surface did not make contact with the substrate. As a result, we concluded that the 1 μm SU-8 membranes were more defect free and had a higher breakdown voltage as compared to the unreleased lens substrates.

2.5 Electrostatic Clamping and Capacitance Measurement

The lens membrane is electrostatically clamped to the substrate when the lens potential is applied. The membrane can be declamped or removed using a drop of water between the membrane and the substrate, making the lenses reusable. The electrostatic clamping event can be detected by measuring the capacitance between the lens and the substrate. Since the entire set up is inside a vacuum, this measurement tells the user whether the lens membrane gets electrostatically clamped on to the substrate or not and what fraction of the membrane makes contact with the substrate.

[Figure 2.27](#) shows a schematic diagram for capacitance measurement where we see that there is a DC power supply V_{DC} and the resistance of the power supply is denoted by R_S in series with the voltage source. The lens membrane

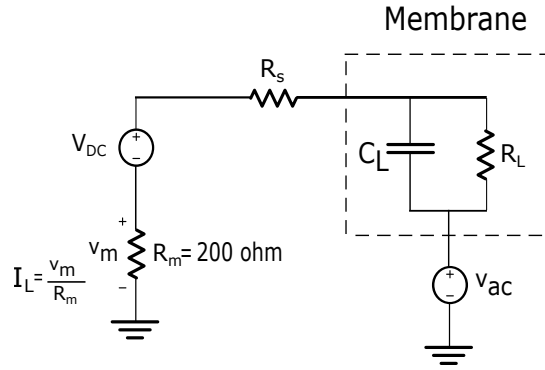


Figure 2.27. Schematic diagram for capacitance measurement.

is represented by a parallel combination of resistor and capacitor R_L and C_L respectively. A known 200 ohm resistor is connected in series with the power supply. To measure the capacitance, a high frequency AC signal is added to the DC signal, and, the current flowing through the capacitor was monitored. Certain known capacitors were used to calibrate the capacitance by measuring the output voltage across a known 200 ohm resistor with an oscilloscope. [Figure 2.28](#) shows the plot between the measured oscilloscope voltage with different known capacitors for different frequency sweeps. The capacitance of a parallel plate capacitor with a dielectric in between is given by $\frac{k\epsilon A}{d}$, where k is the dielectric constant of the medium, ϵ is the permittivity of air, A is the area of one of the plates and d is the separation between the plates. From this equation, we can see that greater the separation between the two plates, the smaller the capacitance. In our system, the dielectric is the SU-8 membrane, the capacitor plates are the gold electrode on top of the membrane and the silicon wafer. The theoretical capacitance calculated when 100 percent membrane makes contact with the substrate comes out to be 1.78nF. So from the graph the measured voltages of 23 mV, 33 mV and 55 mV for 40 KHz, 100 KHz and 200 KHz respectively correspond to nearly 100% contact.

However, if there is a dust particle between the membrane and the substrate

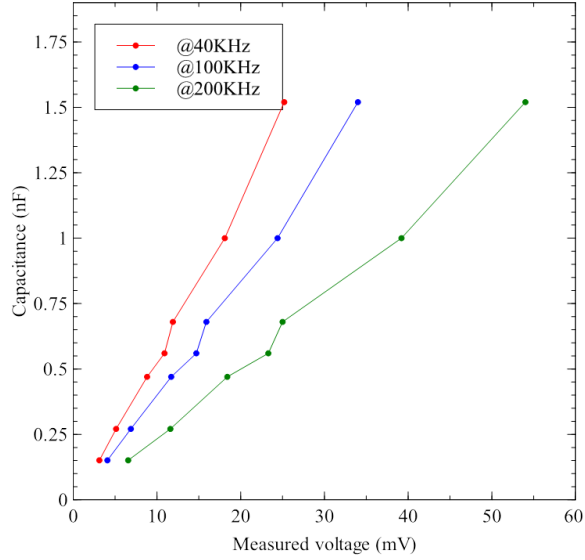


Figure 2.28. Plot showing the measured oscilloscope voltage with different known capacitors for different frequency sweeps.

it raises the membrane from the like a tent, which decreases the contact area by an amount that is much larger than the projected area of the dust particle. [Figure 2.29](#) shows the effect of dust particle between the membrane and substrate. For example, if the diameter of the raised region is $5\times$ the diameter of the diameter of the particle, then the area of the raised region will be $25\times$ the projected area of the dust particle. For a particle with an area of 5 mm^2 and a diameter of $50\text{ }\mu\text{m}$, this implies a 25% reduction in the contact area. The capacitance of the raised region and its nearby adjacent areas are significantly smaller than that of the theoretical capacitance value. The capacitance can be calculated assuming that due to the air gap the total capacitance is the same as having two dielectrics in series. The equation for the capacitance between two plates with two dielectrics in series is

$$C = \frac{k_1 k_2 \epsilon_0 A}{k_1 d_2 + k_2 d_1} = \frac{\epsilon_0 A}{d_2 + \frac{d_1}{k_1}}, \quad (2.1)$$

where k_1 is the dielectric constant of the polymer and k_2 is the dielectric of air/vacuum, which is 1, and d_1 and d_2 are the thickness of the polymer and air,

respectively, A is the cross-sectional area of the plates, and ϵ_0 is the permittivity of free space. In our model, k_1 and k_2 are the dielectric constants of the SU-8 and the air gap, respectively, and d_1 and d_2 are the SU-8 thickness and the air gap, respectively.

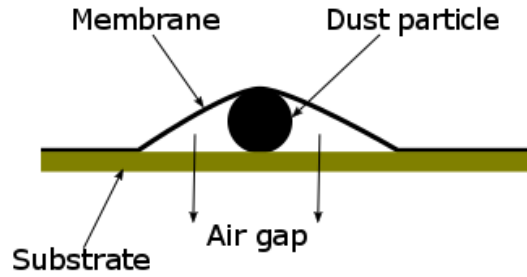


Figure 2.29. Schematic diagram of the effect of dust particle between the membrane and substrate.

The cross-sectional area of the membrane is $4.9 \times 10^{-5} \text{ m}^2$. For 100% contact between the membrane and the substrate the capacitance is calculated to be 1.78 nF, whereas for a $5 \text{ }\mu\text{m}$ air gap, the capacitance comes out to be around 82 pF and for a $10 \text{ }\mu\text{m}$ air gap, the capacitance comes out to be approximately 42 pF as shown in the plot in [Figure 2.30](#). So even at a gap of $5 \text{ }\mu\text{m}$, the capacitance drops almost 20 times from 1.78 nF to 82 pF implying that even where the gap is very small between the membrane and substrate, we see a significant drop in the capacitance. The further we move away from the dust particle the more the membrane pulls down and makes contact with the substrate and the capacitance increases with increasing contact between the membrane and the substrate. Since the whole set up will be in a vacuum, the only way to monitor whether the membrane makes contact with the substrate or not is to measure the capacitance. The measured voltage on the

oscilloscope is calibrated with the capacitance values and this gives an estimation as to what fraction of the membrane makes contact with the substrate (since the theoretical capacitance calculated when 100 percent membrane makes contact with the substrate comes out to be 1.78 nF) as was shown in [Equation 2.1](#).

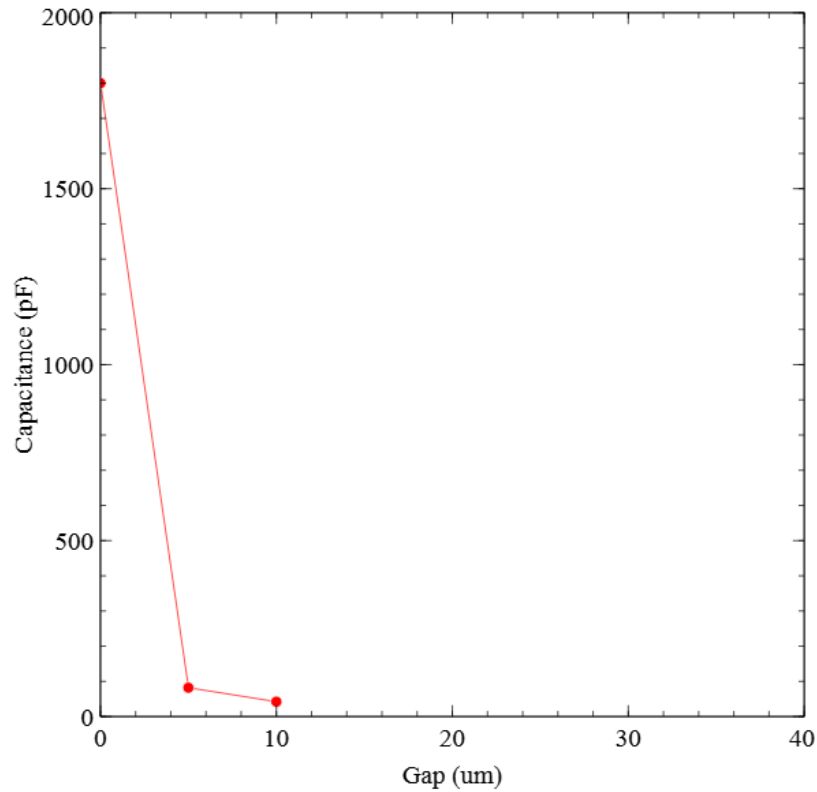


Figure 2.30. Plot showing the change of capacitance with air gap.

2.6 Patterning With Removable Lenses and the Lens Model

Patterning with removable lenses was the main objective of this project as opposed to the previous work that involved patterning with lenses on the substrate. [Figure 2.31](#) shows the experimental set up with removable lenses where the lens membrane against the silicon wafer (substrate for patterning). The acrylic frame supporting the membrane was painted with silver paste and the silver paste was

extended along the sidewall of the frame to the center of the membrane containing the gold electrode to make proper ohmic contact. The patterned area in the center of the membrane was labeled out in the figure. The experiment was run by igniting an argon plasma and feeding chlorine gas to the system. The ion energy was measured to be 99.6 eV and the focusing voltage was chosen to be 94 V and the etching was carried out for 6 minutes. The maximum leakage current measured was 10 mA for 6 minutes.

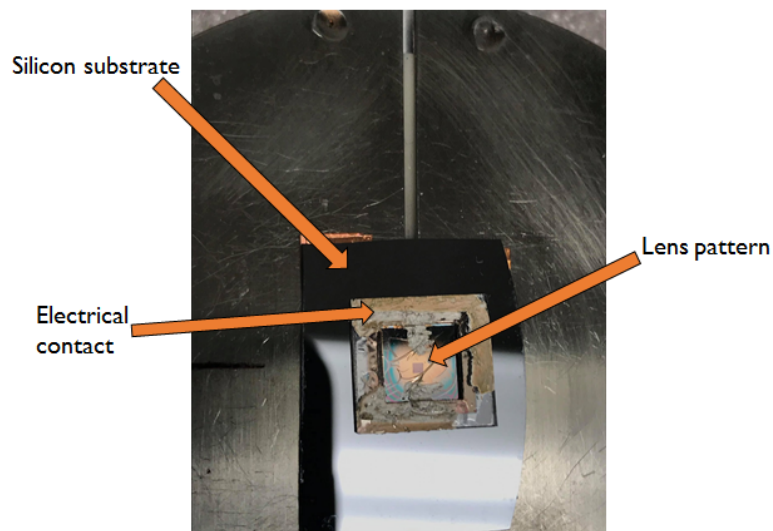


Figure 2.31. Experimental set up with removable lenses

The lens membrane consisted of 1 μm diameter holes. [Figure 2.32\(a\)](#) and [\(b\)](#) show the side view and top view of the SEM images of the etched features on silicon respectively where the etched features were measured to be roughly 97 to 100 nm. The features etched were larger than what was observed in previous work. The hypothesis was that optimizing the focusing voltage will result in smaller spot diameters. The lens diameter also plays a role in determining the final spot size. In order to estimate the correct focusing voltage, a model was designed and simulations were carried out for different lens diameters and different focusing voltages.

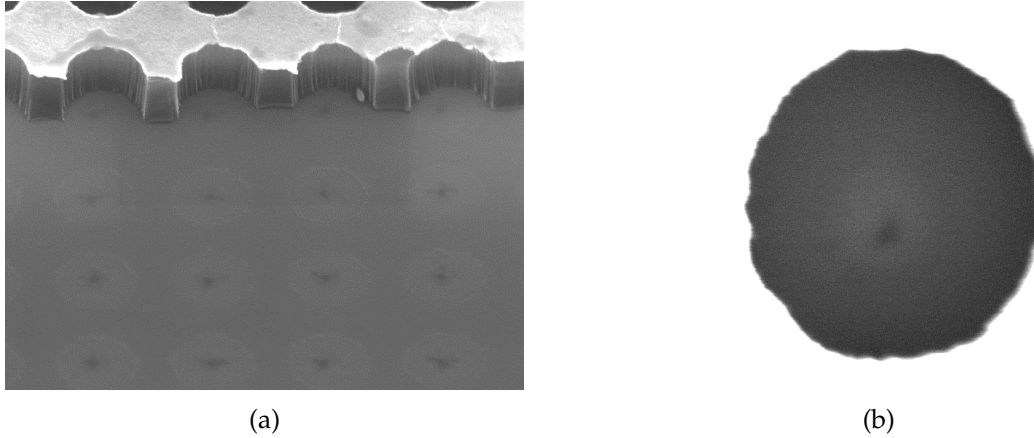


Figure 2.32. SEM image of (a) side view and (b) top view of 100 nm etched features on silicon.

To model the ion trajectories and compute the spot size as a function of lens geometry, applied potential, and ion energy spread, we use the commercial software SimIon, which uses finite differences to compute the potential field from a geometry description and then tracks ion trajectories as they traverse the field. The complete nanopantography system is large when compared to the size of an individual lens and it is not practical to model the entire system. Hence, we compute the trajectories of the ions in the domain near the lens, starting about three microns above the lens surface, and have developed an analytical solution outside of this domain where there are either no electric fields or where they field has a simple geometry.

Figure 2.33 shows a schematic used to derive the analytical solutions. Ions are emitted from the source at the left and drift a distance d_{sm} until they reach the grounded mesh placed before the lens array. When the ions pass through the space between the mesh and the electrode, d_{ML} , they slow down in the presence of the electric field, E , that is formed between these two surfaces by the applied potential V_L . Ions whose trajectory lies along the central axis of the system (where the velocity is only along the x -direction) are emitted from the upper point at the left of the diagram and pass through the mesh into the simulation domain at

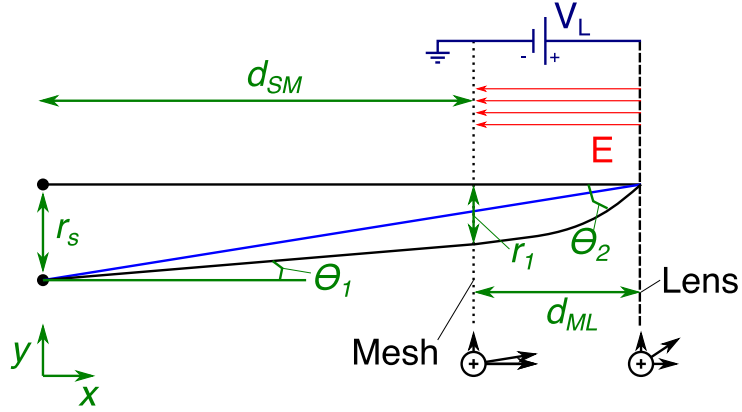


Figure 2.33. Schematic of the simulation domain, showing two trajectories of the ions can take to enter a lines in the Simlon domain.

normal incidence before entering the lens. Ions emitted at the source from a radial position r_s enter the mesh at an angle θ_1 and then enter the same lens opening at an angle θ_2 . It is important to note that the angle at which ions enter the lens opening is not a simple geometric extension to the source, as is shown by the blue line the diagram. To calculate the angles θ_1 and θ_2 , we note that the kinetic energy of the ions entering a lens, K_f , will be their initial kinetic energy, K_o , minus the energy lost traversing the electric field,

$$K_f = K_o - qV_L,$$

where q is the charge of the ion. We can rewrite this expression in terms of particle velocity as

$$\frac{1}{2}mv_{xf}^2 + \frac{1}{2}mv_{yf}^2 = \frac{1}{2}mv_{xo}^2 + \frac{1}{2}mv_{yo}^2 - qV_L.$$

Since the radial velocity is unaffected by the electric field, $v_{yo} = v_{yf} = v_y$, and

$$\frac{1}{2}mv_{xf}^2 = \frac{1}{2}mv_{xo}^2 - qV_L.$$

From this expression, we compute the final axial velocity as

$$v_{xf} = \sqrt{v_{xo}^2 - \frac{2qV_L}{m}}.$$

The force exerted by the electric field is

$$F_x = -q|E| = -q\frac{V_L}{d_{ML}} = ma_x,$$

which allows us to compute the axial acceleration as

$$a_x = -\frac{qV_L}{d_{ML}m}.$$

For ions entering the mesh at a radial position r_1 , the drift time from the mesh to the lens opening is

$$t = \frac{r_1}{v_y}.$$

Geometrically,

$$r_1 = r_s - d_{SM} \tan \theta_1$$

and so the final axial velocity can be written as

$$v_{xf} = v_{xo} + a_x t = v_{xo} + \frac{a_x r_1}{v_y} = v_{xo} - \frac{qV_L(r_s - d_{SM} \tan \theta_1)}{d_{ML}mv_y}.$$

With our previous derivation for v_{xf} , we can write

$$v_{xo} - \frac{qV_L(r_s - d_{SM} \tan \theta_1)}{d_{ML}mv_y} = \sqrt{v_{xo}^2 - \frac{2qV_L}{m}}.$$

The initial x and y velocities can be computed from the kinetic energy as

$$v_{xo} = \sqrt{\frac{2K_o}{m}} \cos \theta_1$$

and

$$v_y = \sqrt{\frac{2K_o}{m}} \sin \theta_1,$$

so that our expression becomes

$$\sqrt{\frac{2K_o}{m}} \cos \theta_1 - \frac{qV_L(r_s - d_{SM} \tan \theta_1)}{d_{ML}m\sqrt{\frac{2K_o}{m}} \sin \theta_1} = \sqrt{\left(\sqrt{\frac{2K_o}{m}} \cos \theta_1\right)^2 - \frac{2qV_L}{m}},$$

which reduces to

$$\sqrt{2K_o} \cos \theta_1 - \frac{qV_L(r_s - d_{SM} \tan \theta_1)}{d_{ML}\sqrt{2K_o} \sin \theta_1} = \sqrt{2K_o \cos^2 \theta_1 - 2qV_L}.$$

For convenience, we express the kinetic energy in electron volts, $\frac{K_o}{q} = K_{eV}$, which allows us to write the equation without q ,

$$2d_{ML} \sin \theta_1 \left(\sqrt{K_{eV}^2 \cos^2 \theta_1 - K_{eV} V_L - K_{eV} \cos \theta_1} \right) + V_L(r_s - d_{SM} \tan \theta_1) = 0$$

and we can solve for θ_1 numerically when given the ion energy, the lens potential, the source-to-mesh spacing and the mesh-to-lens spacing. The second angle can be computed from the ratio of the final velocities of the ions as they enter the lens. First, we express the final axial velocity in terms of energy as

$$v_{xf} = \sqrt{v_{xo}^2 - \frac{2qV_L}{m}} = \sqrt{\left(\sqrt{\frac{2K_o}{m}} \cos \theta_1 \right)^2 - \frac{2qV_L}{m}} = \sqrt{\frac{2K_o}{m} \cos^2 \theta_1 - \frac{2qV_L}{m}}$$

and the radial velocity as

$$v_y = \sqrt{\frac{2K_o}{m}} \sin \theta_1.$$

The angle then becomes

$$\theta_2 = \tan^{-1} \left(\frac{v_y}{v_{xf}} \right) = \tan^{-1} \left(\frac{\sqrt{\frac{2K_o}{m}} \sin \theta_1}{\sqrt{\frac{2K_o}{m} \cos^2 \theta_1 - \frac{2qV_L}{m}}} \right) = \tan^{-1} \left(\frac{\sqrt{K_o} \sin \theta_1}{\sqrt{K_o \cos^2 \theta_1 - qV_L}} \right),$$

and, as before, expressing the energy in eV allows us to remove the variable q ,

$$\theta_2 = \tan^{-1} \left(\frac{\sqrt{K_{eV}} \sin \theta_1}{\sqrt{K_{eV} \cos^2 \theta_1 - V_L}} \right).$$

The geometry of the lens is drawn within the SimIon software and the associated simulation parameters, such as the output file name and format, are set within the program. A python script then calls SimIon in batch mode to compute the potential field with for a specific lens potential. Next, the script determines the starting location and trajectories of the ions that enter into the simulation domain as follow. First, a random starting position at the source is generated and the associated landing angle, θ_2 , is computed using the analytical model. The radial position of the ion entering the lens domain is randomized and an

energy is assigned using a normal random number generator whose parameters are provided by the measured characteristics of the ion source. The energy of the ions is then scaled to take into account the energy loss by the electric field, and the location, angle, and energy of all of the ions is tabulated in an input file. This file is then read by the SimIon program to compute the final location of the ions within the domain, which are stored in an output file. This file is read by the script when the simulation is complete, and stored for analysis. This process is repeated for each lens potential and allows for an automated calculation of the final positions of all of the ions for all focusing voltages.

The geometry of the lens is drawn within the SimIon software and the associated simulation parameters, such as the output file name and format, are set within the program. A python script then calls SimIon in batch mode to compute the potential field with for a specific lens potential. Next, the script determines the starting location and trajectories of the ions that enter into the simulation domain as follow. First, a random starting position at the source is generated and the associated landing angle, is computed using the analytical model. The radial position of the ion entering the lens domain is randomized and an energy is assigned using a normal random number generator whose parameters are provided by the measured characteristics of the ion source. The energy of the ions is then scaled to take into account the energy loss by the electric field, and the location, angle, and energy of all of the ions is tabulated in an input file. This file is then read by the SimIon program to compute the final location of the ions within the domain, which are stored in an output file. This file is read by the script when the simulation is complete, and stored for analysis. This process is repeated for each lens potential and allows for an automated calculation of the final positions of all of the ions for all focusing voltages.

Three different diameters lenses (300 nm, 500 nm, and 1 μm), each with a

1 μm thick dielectric layer, were simulated to determine the distribution of the ions at the base of the lens as a function of the lens potential. The ion energy was based on measurements of the system and was 67 eV with a 3.5 eV FWHM. The source diameter was 5 mm and the spacing between the source and the grounded mesh was 60 cm. The distance between the mesh and the lens as 1.6 cm and the simulation domain started 3 μm above the lens opening and the number of ions tracked at each lens potential was 5×10^4 .

Figure 2.34 shows histograms of the ion position at the base of the 1 μm diameter lens openings for lens potentials ranging from 61 V to 67 V. Since the distribution is not normal, we determined its full-width at half-maximum (FWHM) from the location where the ion count exceeded half of the maximum on both sides of the distribution. The normal distribution with the corresponding FWHM value is also plotted as a blue line and shows that a good number of ions fall outside of the distribution. However, the FWHM is the best measure for the feature size that will be formed by the beam in the substrate. The best focus (i.e., smallest FWHM value) for this system is very close to the mean ion energy for this geometry, which means that many of the ions are not able to enter the lens at all: at 66.7 eV only half of the ions reach the substrate, while the other half is rejected. Also, the aberrations of the system limit the smallest image size to about 30 nm, which is about three times larger than the aberration-free value predicted by the ideal lens formulas.

Figure 2.35 shows the histograms for the 500 nm diameter lenses, where the minimum FWHM value is below 20 nm, or about twice as large as the aberration-free value, and it is formed at substantially lower lens potentials, at about 64.5 V. The smaller image size is attributed to the smaller numerical aperture (NA) of the lens: the NA is reduced from 0.44 for the 1 μm lens to 0.24 for the 500 nm lens. Since aberrations scale with NA, we were expecting smaller features with this lens

design at a cost of lower currents (the current scales with area of the lenses). The distributions for the 300 nm diameter lens are shown in [Figure 2.36](#), where the nominal focusing potential is around 62.7 V and the size of the image is reduced further to 15 nm for an NA of 0.15, about 1.5 times the aberration-free value.

The graph in [Figure 2.37](#) summarizes the findings by plotting the FWHM as a function of the lens potential for all three lens sizes. The smaller lenses yield smaller images due to their reduced numerical aperture and the focusing potential drops with lens diameter as well. One aspect of the smaller lenses is that the image size is less sensitive to the lens potential, making the system easier to use. The easiest way to reduce the feature size further is to reduce the size of the source, but the size will eventually be limited by the chromatic aberrations. Our simulations show that the minimum feature size imposed by the chromatic aberrations is 8 nm, 5 nm, and 4 nm for the 1 μm , 500 nm, and 300 nm diameter lenses, even if the size of the source was infinitely small (which would form an infinitely small image in an ideal lens). This implies that single nanometer sized features are possible when reducing the source size. Reducing the thickness of the dielectric layer will decrease the magnification and allow for smaller features with larger source sizes, but it requires better materials (the SU-8 can only realistically sustain about 70 V per μm of thickness). Lastly, lowering the ion energy reduces the requirements for the dielectric, but would require further optimization of the source to ensure sufficient current and a reduced energy spread.

Another experiment was run with the identical experimental set up as shown in [Figure 2.31](#). This lens membrane had lens diameters ranging from 0.8 μm to 1.6 μm . The substrate was highly doped silicon and the energy of the argon ion beam was measured to be 72.2 eV with an energy spread of 4.2 eV. The etch was run for 30 minutes at 71.2 V with peak leakage current of 0.16 μA . [Figure 2.38\(a\)](#) and (b) are the top down SEM images of the etched features where the diameter of

the spot size was measured to be roughly 28 to 30 nm for the 1 μm lens diameters. As per the simulation result in [Figure 2.37](#), where the FWHM for a 1 μm diameter lens is 30 nm at around 66.6 V for a beam energy of 67 eV. So the experimental results with the 1 μm lens diameter agrees with the predicted model with the required lens diameter and focusing voltage settings.

2.7 Conclusion

In this work we have manufactured removable, electrostatic lenses using free-standing 1 μm thick SU-8 membranes. We have characterised an anisotropic RIE process to manufacture these lenses. This work started by using SF_6 plasma to etch SU-8 using copper as a hard mask. But we observed that SF_6 etching left behind a deposition on the sidewalls of the SU-8 and hence we used oxygen plasma to etch the SU-8. We measured the etch rates and selectivities of the SU-8 and copper and identified that conditioning the RIE chamber with SF_6 plasma increases the selectivity between SU-8 and copper to around 50 from the previously measured value of 17. We successfully manufactured SU-8 lenses using oxygen RIE and also etched 30 nm features using these SU-8 membranes and demonstrated nanopantography using removable lenses. We carried out simulations with different lens diameters and lens potentials and concluded that the experimental results with 1 μm diameter lenses agree with the simulation results. Our future work in this project is to demonstrate nanopantography using smaller lens diameters of 500 nm and 300 nm which would result in etched features in the order of 10 nm to 15 nm as predicted by the simulation results.

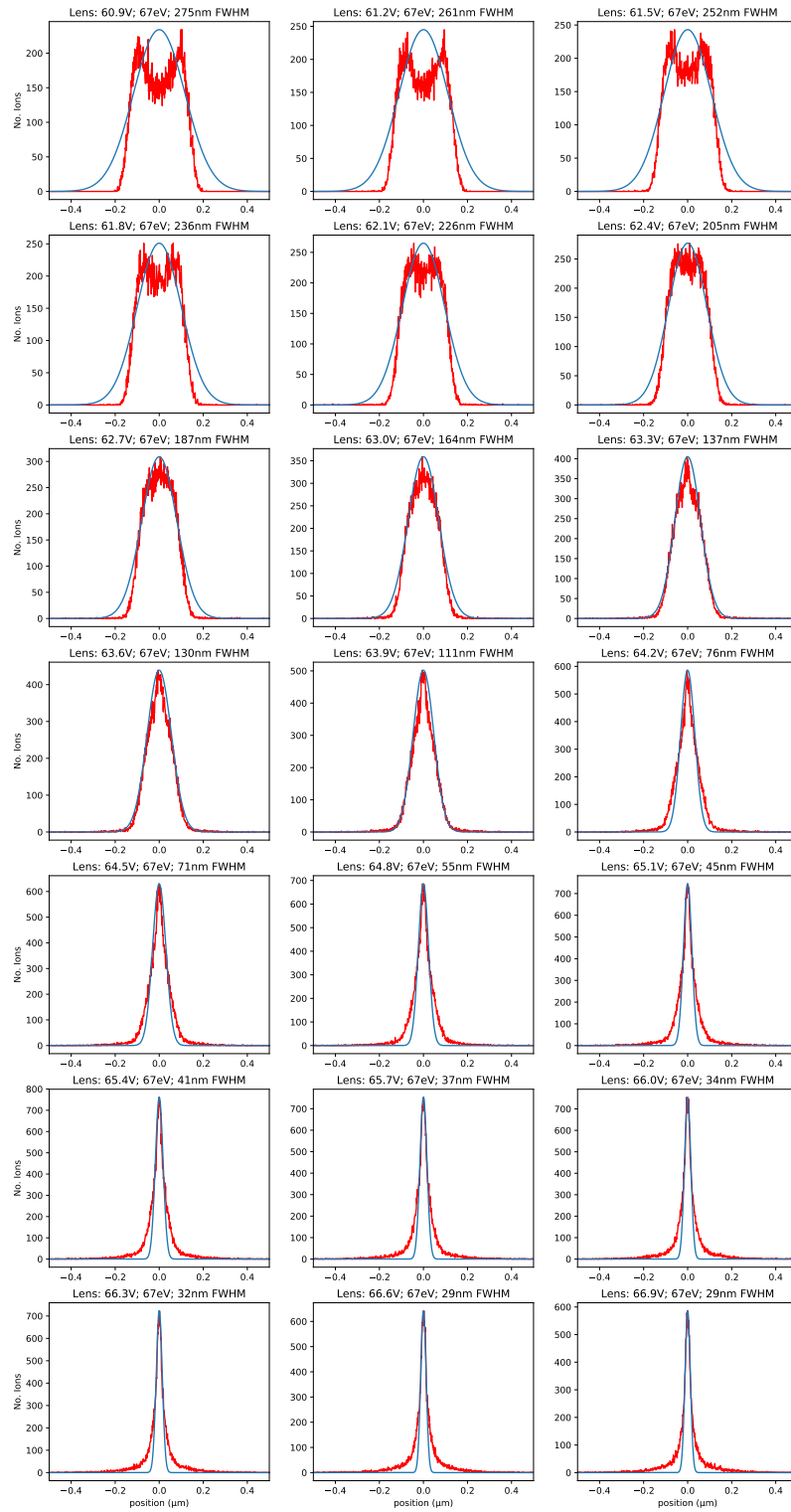


Figure 2.34. Histograms of the ions at the base of the lens as a function of lens potential for 1 μm diameter lenses.

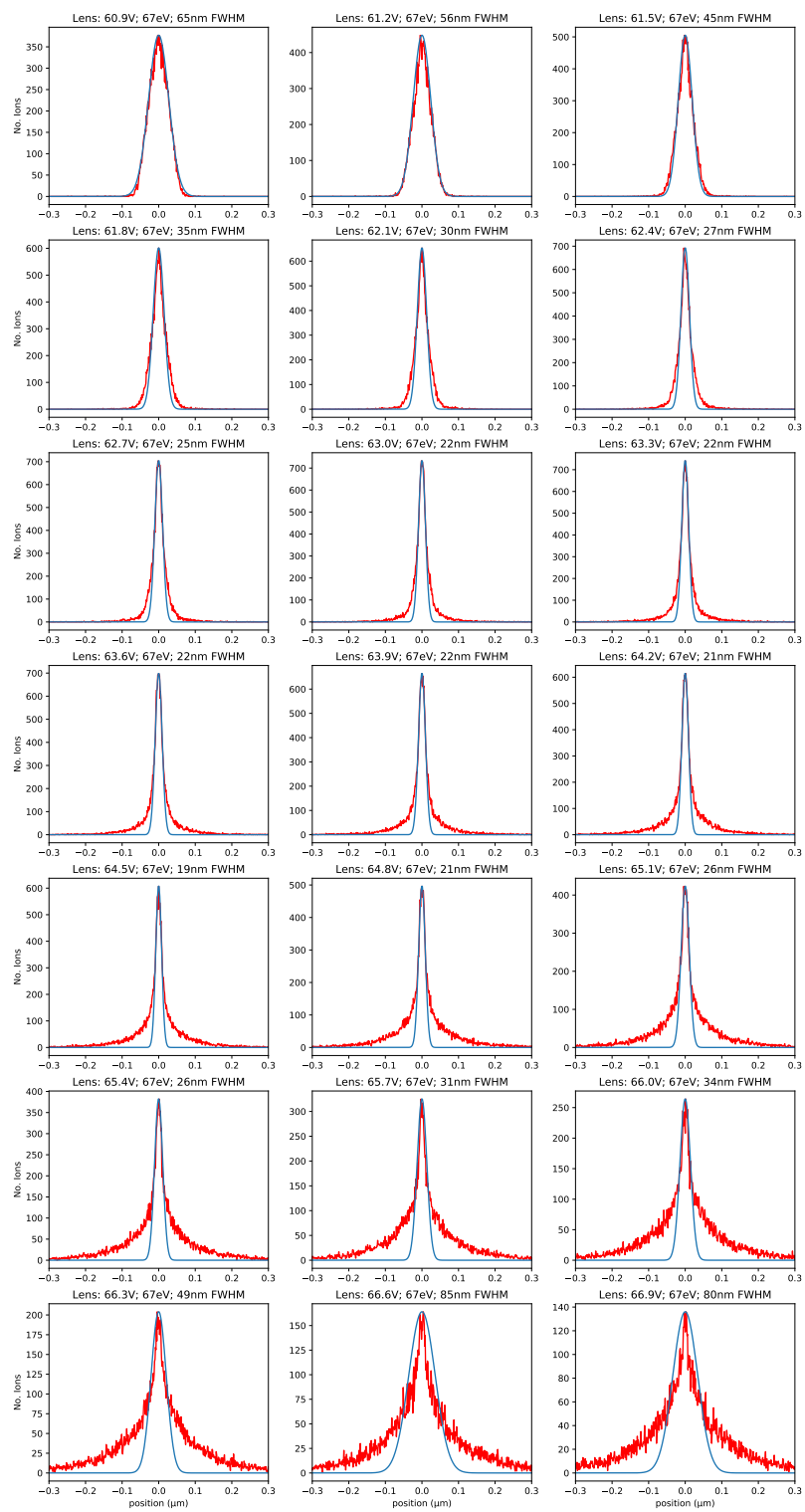


Figure 2.35. Histograms of the ions at the base of the lens as a function of lens potential for 500 nm diameter lenses.

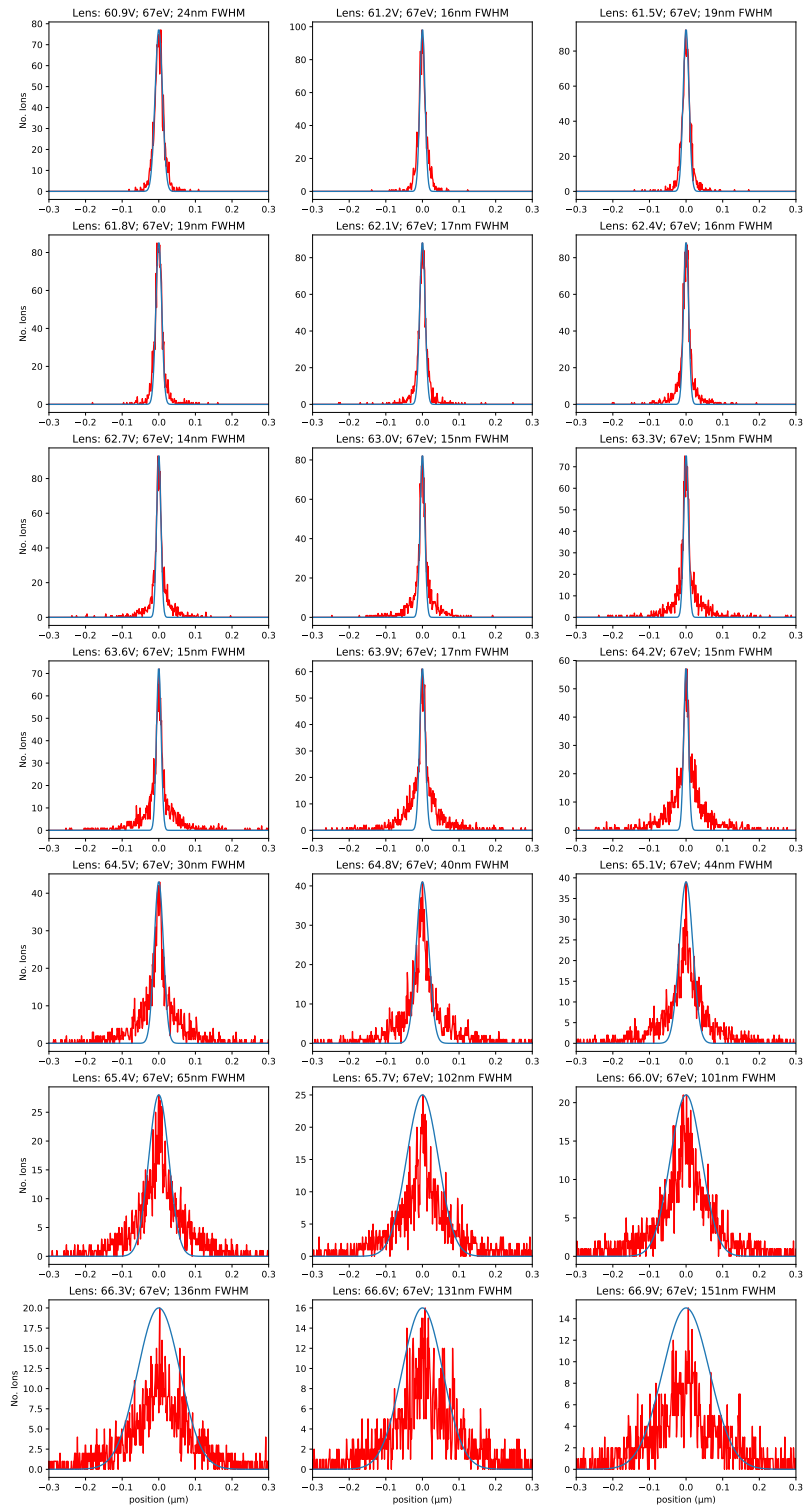


Figure 2.36. Histograms of the ions at the base of the lens as a function of lens potential for 300 nm diameter lenses.

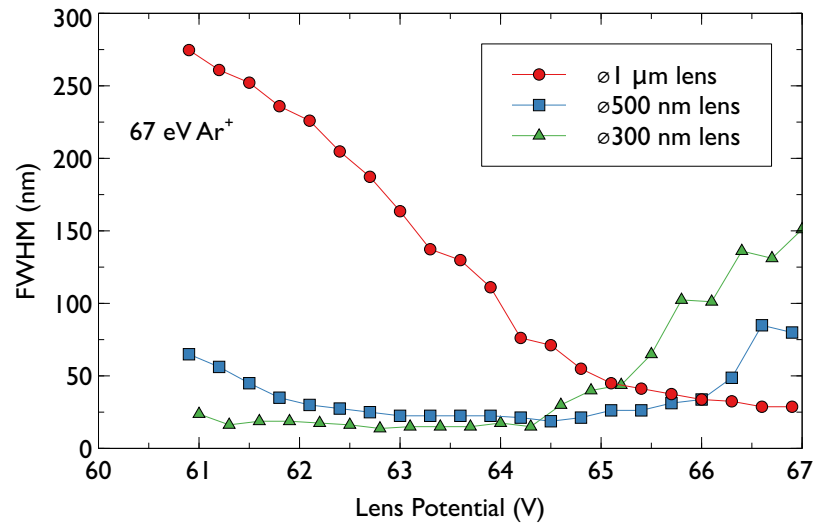


Figure 2.37. The FWHM of the images formed by the three lenses as a function of lens potential.

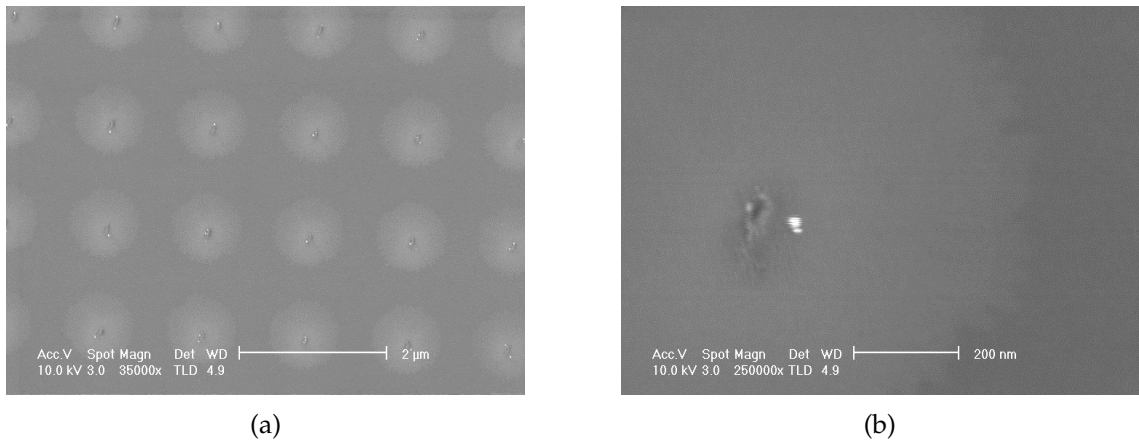


Figure 2.38. SEM images of (a) low magnification and (b) high magnification 28 nm etched features on silicon.

Chapter 3

Atom Beam Lithography Stencil Masks for the Development of Reusable Electrostatic Lenses

3.1 Introduction and Background

Atom beam proximity lithography is a low cost, high throughput printing technique capable of forming sub-100 nm features in a laboratory with minimal hardware requirements. In this process, a broad beam of atoms (neutrals) is extracted from a source and illuminates a stencil mask on the substrate in an exposure chamber. Atoms that strike the opaque regions of the mask are stopped, while those passing through the openings are used to damage the resist on a substrate that is placed underneath the mask. The tool can be operated with equipment at a reasonable cost, and because of its simplicity and high throughput it is far more user friendly in a university laboratory set up. One critical aspect of proximity lithography is that its ions/atoms have extremely small particle wavelengths (for instance, the de Broglie wavelength of 7.5 keV He^+ ions is just 1.6 Angstroms). For a mask to substrate gap of 100 μm , the blur of the system is around 35 nm.

A diagram of the atom beam lithography tool in our lab is shown in [Figure 3.1](#). A saddle field source generates a beam of mixed ions and atoms. Helium gas is flowed into the system. The source consists of an anode with a hole in its center is connected to a positive potential while a cylindrical cathode on both

sides of the anode is at ground potential. Electrons are accelerated to the anode and some will enter the aperture to then oscillate as they are trapped by the saddle-shaped electrostatic field that forms between the anode and the cathodes. The oscillating behavior of the electrons increases the electron path length, and therefore, the ionization probability, and the source can be operated at relatively low pressures; even though the source is only an inch in length, the distance traversed by the oscillating electrons can be several meters. The ions generated in the source are accelerated towards the cathode, where some can escape through a small aperture. There is a high probability of neutralization of the ions by charge-exchange collisions, and so the source emits a mixed beam of atoms and ions. A pair of deflector plates removes the ions from the beam, leaving behind the neutral helium beam. The broad beam of helium atoms illuminates a stencil mask (free standing polymer membrane).

The pattern in the stencil mask is replicated on the substrate we are patterning. It is worth noting that the ion trajectories curve as they experience the Lorentz force from the earth's magnetic field, and ions and atoms have two distinct landing angles on the mask, which results in two distinct images. It is for this reason that the ions are removed from the system. The proximity lithography system has the ability to utilize a technique called aperture array lithography (AAL), and it is suitable to print highly periodic patterns like arrays of software-controllable shapes. It works by stepping the mask with respect to the substrate in small increments to increase the density of the printed features so that large area patterns can be printed at a high density. Designing the stencil masks for this tool is a significant challenge and the next sub-section presents a review of the various types of stencil masks that were previously designed alongside their advantages and drawbacks.

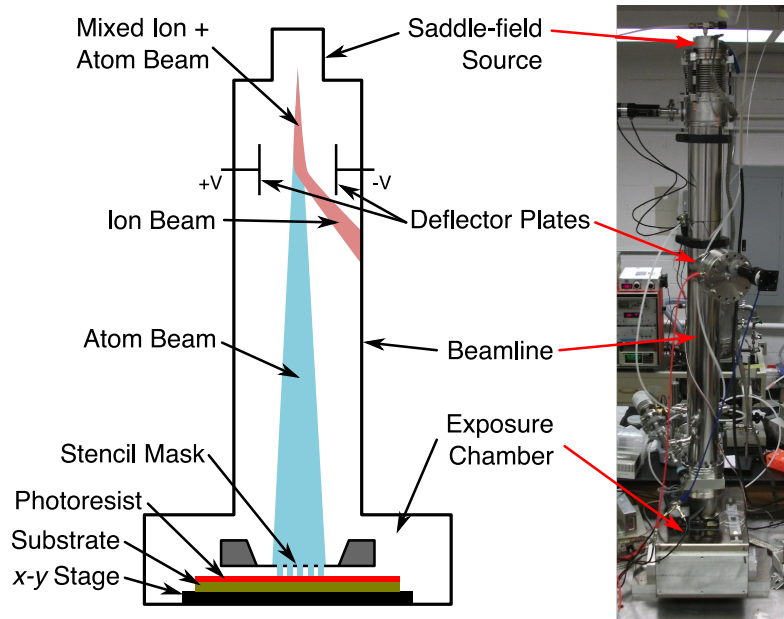


Figure 3.1. Schematic diagram of the atom beam lithography tool and the actual instrument in the lab.

3.1.1 Silicon Nitride Masks

One of the key components of atom beam lithography is the use of stencil masks. Stencil masks consist of a thin membrane of made of either a dielectric or silicon, and it consists of etched holes/openings of known dimensions [5]. The thickness of the membrane plays a big role in determining the smallest possible opening in the mask because there is a maximum aspect ratio that can be etched through the material of high quality. The membrane thickness also determines maximum energy of the incoming particles (atoms/ions) which it can block. Stencil masks made from silicon nitride (SiN_x) generally consist of a thin silicon nitride membrane that is around $0.5 \mu\text{m}$ to $1 \mu\text{m}$ thick and it consists of holes etched through the entire membrane thickness. In previous work, masked ion beam lithography (MIBL) using silicon nitride stencil masks at a $25 \mu\text{m}$ mask-to-sample gap had been used to replicate 80 nm lines and spaces in PMMA. The $1 \mu\text{m}$

thickness is sufficient to stop protons and SiN_x stencil masks which were $0.5\ \mu\text{m}$ thick were also suitable for stopping protons of 50 kV energy or helium ions. The most critical phase of mask fabrication is the reactive ion etching step, which creates the mask openings or etched holes in the silicon nitride.

Highly anisotropic etching is required to produce fine etched patterns in films thick enough to stop the ions. Etched profiles with nearly vertical sidewalls are necessary to minimize the scattering of ions through the edges of the mask openings. Figure 3.2 shows a schematic diagram of a stencil mask. Previous studies suggest that a stencil mask with a thickness of $0.5\ \mu\text{m}$ to $1\ \mu\text{m}$ were suitable for stopping protons or helium ions of energy 50 kV to 100 kV. In our system we have used stencil masks of thickness varying between 250 nm and 500 nm for a particle of energy 7.5-8.5 keV.

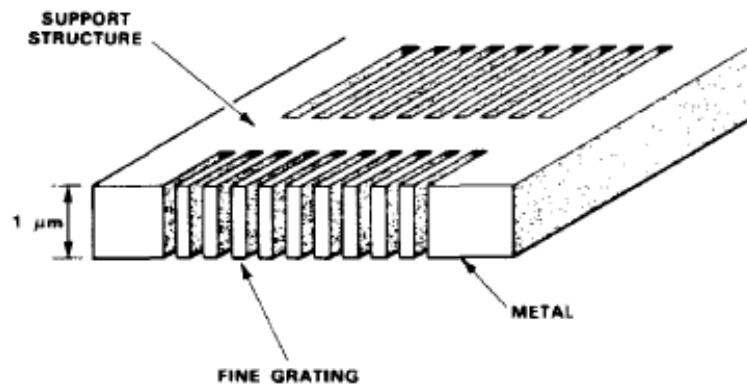


Figure 3.2. Schematic diagram of a stencil mask, taken from [5].

In earlier work [5], a reactive ion etch process for SiN_x used CF_4 as the etch gas with a 250 V self-bias potential. This process was used to etch a 320 nm-period grating through a $1\ \mu\text{m}$ thick SiN_x membrane. To define the patterns, around 80 nm of nickel was deposited as the hard mask by the lift off technique using x-ray lithography. The observed etch profile was highly isotropic, which is

problematic because ions can easily be scattered through the non-vertical edges of the transmission hole, which reduces the image contrast. Later, an improved RIE process was developed using CHF_3 as an etch gas and a 500 V self-bias potential. There were, however, several difficulties with this RIE process. The etching of very fine geometries (less than 0.3 μm line width) into a 1 μm thick film left a 10 nm to 40 nm thick polymer layer at the bottom of the transmission holes at the SiN_x -Si interface. This layer was not removed by continuous etching with CHF_3 and also survived the subsequent mask fabrication steps. This layer was due to polymer deposition which was known to occur in RIE processes which use CHF_3 as the etch gas. It was discovered that an additional RIE step with CF_4 removed this film without significantly affecting the etched mask openings. Another challenge associated with this process was that, for small mask openings, the etch rate decreased as the thickness of the mask increased. This was due to the slowdown of the RIE step due to aspect ratio dependant etching where the sidewalls of the mask gets charged by the impinging ions and the additional incoming ions gets repelled by the sidewall charging and cannot not reach the bottom of the trenches or mask openings. All these factors led to several incompletely etched masks through the entire fabrication process. The maximum aspect ratio that was achieved was approximately 6:1; therefore masks with 80 nm line-widths were fabricated from 0.5 μm thick membranes.

Another technique previously used to make stencil masks used palladium as the hard mask. In that process, a double side polished silicon wafer was coated with 250 nm SiN_x on both sides. A pattern of windows was etched through the silicon nitride on one side of the wafer using a magnetically enhanced reactive ion etching system (MERIE) using 0.8 mTorr carbon tetra fluoride (CF_4) and 0.2 mTorr oxygen (O_2) plasma and 85 W power and 250 nm thick free standing silicon nitride membranes were made. A palladium (Pd) layer (20 nm) was then deposited on

the membrane wafer using dc magnetron sputtering at a base pressure of 10 μ torr and an argon (Ar) gas pressure of 10 mTorr, followed by spin coating of 60 nm of FOX-12 (flowable oxide from DOW Corning). The wafer was then baked at 250 °C to obtain a uniform layer of silicon oxide. The reason for depositing a metal and an oxide layer is to effectively help transfer the resist pattern into the nitride membrane. PMMA (200 nm) was then spun on, and the desired pattern was printed using an electron beam writer.

After patterning, the resist was developed in a room temperature 3:1 solution of isopropyl alcohol (IPA): methyl isobutyl ketone (MIBK) for 45 seconds, rinsed in IPA for 30 sec and dried in nitrogen. The resist pattern was first transferred into silicon dioxide using 0.7 mTorr of trifluoromethane (CHF_3) gas at 70 W power. An argon ion-milling step further transfers the pattern into the thin Pd layer, the hard-mask for transferring the pattern into silicon nitride membrane. It should be emphasized here that the choice of metal layer (as a hard mask) to transfer the pattern into the nitride in the final step is extremely important. It was found that adding CF_4 suppresses the milling rates, likely due to the passivation of the Pd surface. Significantly, CF_4/O_2 RIE is a high-rate, anisotropic RIE process for etching SiN_x . In CF_4/O_2 RIE, Pd etches $150\times$ slower than the nitride, thus allowing the pattern to be transferred through the entire thickness of the silicon nitride membrane with minimum damage to the palladium hard-mask. For comparison, gold is removed about 20 times faster than palladium in CF_4/O_2 RIE, while the gold/palladium removal rates are similar in argon. That's why palladium was chosen instead of gold as the hard mask as it etches slowly in CF_4 .

However, SiN_x stencil masks had their drawbacks too. Thermal distortions in stencil masks were caused by mask heating due to the incoming ion beam. Because the stencil masks are in vacuum, there was no convection cooling. Even if the mask material was a good thermal conductor, such as silicon, the large areas of the

stencil masks compared to their relatively small thickness made conduction a poor method of removing heat and caused thermal gradients across the mask. Because of no convection and poor conduction, radiation cooling is non-negligible in stencil masks. Grid-support stencil masks [6], which employ a matrix of small mask openings instead of completely open areas, were used to eliminate most of the pattern restrictions associated with stencil masks, and to improve mask stability. [Figure 3.3](#) shows a grid support stencil mask where nickel was deposited using lift-off and the combination of the nickel layer together with 300 nm of PMMA as the photoresist comprised the mask for the RIE for the transmission holes.

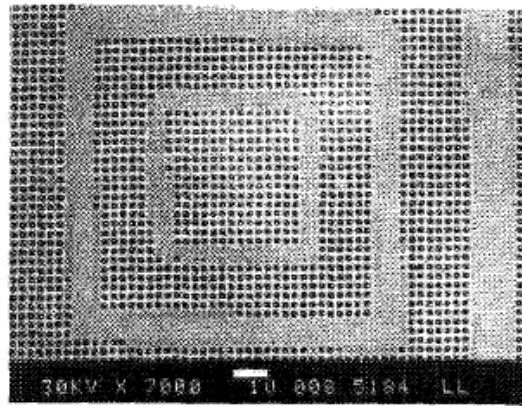


Figure 3.3. Fabrication of a grid support stencil mask, taken from [6].

The RIE step used CHF_3 as the etch gas at a self-bias potential of 500 V. A tetramethylammonium hydroxide (TMAH) etchant was used to remove the silicon from behind the mask membrane in these window areas. The silicon oxide layer was removed with HF solution. Finally a 20 nm thick nickel layer was deposited to prevent charging during exposure [6]. Holes etched in membranes usually resulted in variations in stress and therefore create mask distortions. These grid-support stencil masks reduced the mask distortions due to patterning. In these types of structures, high anisotropic etching of high aspect-ratio holes was formed in the membrane. The completely uniform array of holes allowed the stress in the

masks to be increased, which subsequently allowed the mask to be stiffer and more robust. The use of a grid support mask removed the pattern restrictions usually associated with stencil masks but the highest resolution and most precise line-width control still was obtained with simple stencil masks. Figure 3.4 shows the steps of fabricating a grid support stencil mask.

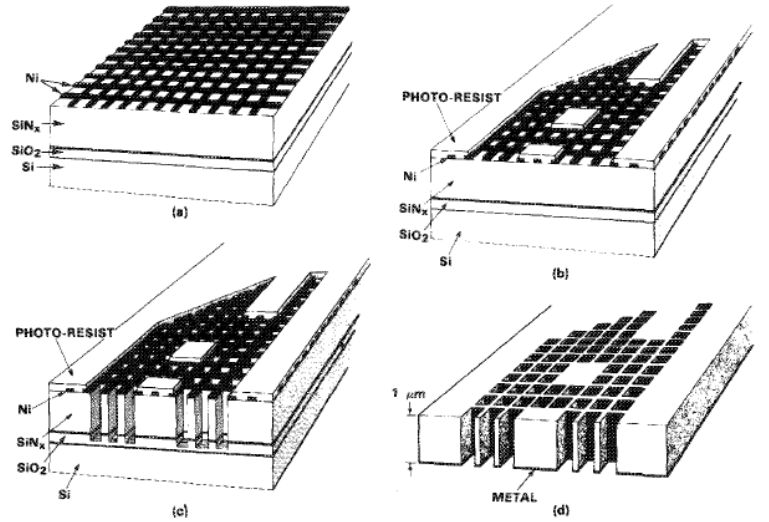


Figure 3.4. Diagram of a grid support stencil mask, taken from [6].

One major issue was that ions usually striking on the mask near the boundary of its openings and scattered laterally in the mask and escaped the mask through the sidewall of a hole at an arbitrary angle. Any ion striking very near a transmission hole may scatter laterally into its openings and escape the mask at an arbitrary angle. These scattered ions reduced the effective contrast of the mask. This scattering effect [7] produced a background exposure, which results the resist between the exposed lines to slowly develop, both thinning the resist and removing resist from the sides, thus increasing the line-width. Effective contrast in an ion beam stencil mask was defined as the ratio of the total incident ion flux to the flux of ions which strike but escape the mask. From the line-width data that were found it was clear that for simple stencil masks the contrast very large.

For grid-support masks, however, the situation was considerably different. The area of mask near transmission hole perimeters was significantly increased in grid-support masks. Therefore, a greater amount of ion scattering from this type of mask was expected.

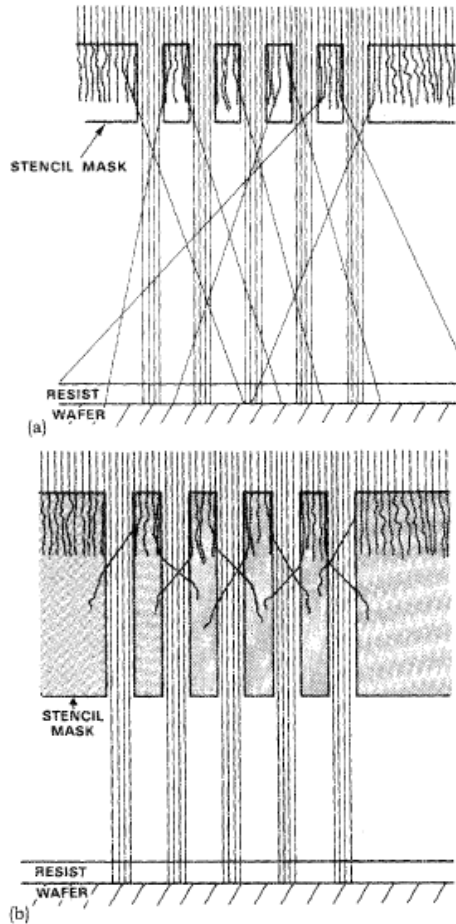


Figure 3.5. Diagram showing the ion scattering effect through a stencil mask, taken from [7].

Figure 3.5 shows a schematic diagram of ions striking a stencil mask and the ions scattering within the opaque regions escaped the mask openings through its sidewalls. The problem was that those ions that escaped would expose all regions of the resist, thereby decreasing the image contrast [7]. A mask whose thickness was similar to the ion range had scattered ions escape while a thicker mask with the same pattern and same ion energy would trap most ions in adjacent regions.

The previous mask fabrication processes, as explained in this chapter, mostly used CF_4 and CHF_3 as the etchants. However, as a result of this, the entire process was slow as the etch rates of SiN_x in CF_4 and CHF_3 were slow.

Another technique was implemented for pattern definition in semiconductor materials using stencil masks. Instead of using the conventional polymer resist and lithographic processing steps, features in the substrates were defined by dry etching through stencil masks [8]. These stencil masks, which consisted of free-standing SiN_x membranes covered with a thin metal layer and supported on Si substrates, were used to replicate high-resolution features with high fidelity. The stencil masks used in this study were 1 μm thick membranes with transmission openings as small as 60 nm and were similar to those used for masked ion beam lithography. SiN_x films were deposited on Si wafers by chemical vapor deposition. The transmission holes in the SiN_x membrane were etched by reactive ion etching (RIE) in CF_4 at 250 V and 5 mTorr. This etching condition resulted in vertical sidewalls in the SiN_x and selectivity larger than 40:1 with nickel as the etching mask. Si was removed from behind the SiN_x membrane by wet chemical etching. The passage of chemical solution through the SiN_x openings sometimes caused breakage of the membranes. This membrane breakage problem was avoided by having a silicon dioxide (SiO_2) layer between the SiN_x film and the Si substrate. An additional RIE step was required to clear the oxide layer after the Si substrate was removed. Typically, 100 nm thick nickel was evaporated at the back of the stencil masks to serve as a dry etch mask and to protect the SiN_x membrane from etching.

Figure 3.6 shows the etch profile of GaAs samples that were etched using stencil masks in direct contact with the substrates. Cl_2 was used as the etching gas at 250 V and 5 mTorr. Etch profiles obtained by using stencil masks in direct contact with the samples were similar to those using Ni masks defined by the

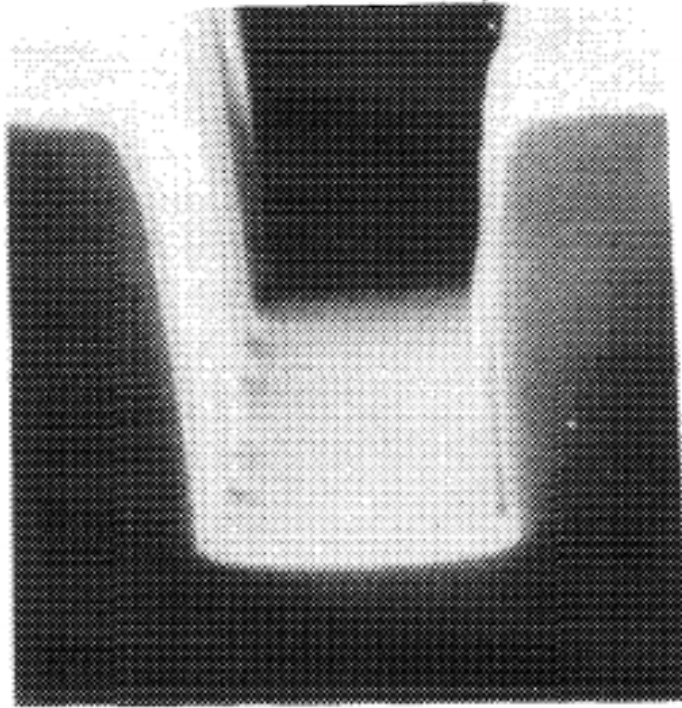


Figure 3.6. Diagram of the etch profile of GaAs in Cl_2 through a stencil mask, taken from [8].

conventional photolithography and liftoff technique. Similar profiles and vertical sidewalls were obtained as the chamber pressure varied between 2 and 10 mTorr. However, the etch profiles changed significantly when the stencil masks were not in direct contact with the samples. [Figure 3.7](#) shows the rounded profiles of GaAs etched in Cl_2 when the mask was separated from the sample by a $6.5 \mu\text{m}$ gap[8]. The rounded profiles and the increased width of the etched features are due to the divergence of the ion flux. There was always some degree of ion divergence which made it difficult to reproduce the exact mask openings for any reasonable gap (greater than $5 \mu\text{m}$) between the mask and the sample.

Another process to develop SiN_x stencil masks was designed to overcome the challenges associated with CF_4 and CHF_3 etching [9]. Firstly, $0.5 \mu\text{m}$ thick silicon nitride membranes were formed and additional layers were deposited on a whole wafer. The membranes were formed from double side polished four inch wafers coated with a 500 nm thick layer of SiN_x . Multiple openings or windows of

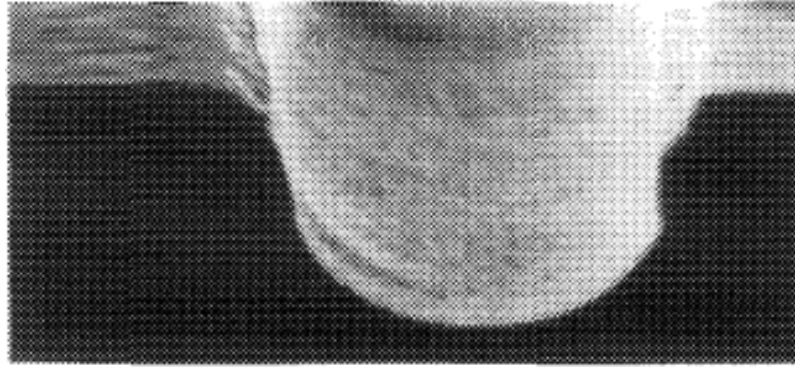


Figure 3.7. Diagram of the etch profile of GaAs in Cl_2 through a stencil mask at a gap of $6\ \mu\text{m}$, taken from [8].

roughly 4cm^2 size were etched into the SiN_x layer on one side of the wafer using transparency film as an etch mask. The gasses used were 0.2 mTorr of oxygen and 0.8 mTorr of CF_4 and a power setting of 30 W. To form the membranes, the silicon was etched in the exposed windows using a solution of potassium hydroxide (KOH) and water. A large beaker was filled with 2 liters of deionized water and 1 kg of KOH pellets. The KOH solution is set to $80\ ^\circ\text{C}$ using a temperature probe and stirred at 300 rpm. Once the KOH pellets have completely dissolved, the wafer was placed in the beaker. The process took about 8 hours to remove the full thickness of the wafer, and the wafer was kept in the solution another hour to remove any remaining KOH crystals from the membranes. The etched wafer was placed in pure deionized water at $80\ ^\circ\text{C}$ for 30 minutes. The wafer was then placed in room temperature deionized water for 30 minutes and vertically on a carrier and rinsed with isopropanol, and then drip dried. One of the first techniques of membrane patterning during the mask fabrication process that was tried during was the wet etch process. However, the choice of the hard mask is critical in this process and copper was chosen as the hard mask because it can be etched with a suitable liquid etchant, citric acid. In this process, the SiN_x membrane of $0.5\ \mu\text{m}$ thickness had to be coated with copper and PMMA which is a positive

tone resist. After exposing the PMMA to ion/electron beam lithography and developing, the copper had to be etched using citric acid followed by reactive ion etching of the nitride membrane using 0.8 mTorr of SF₆ and 0.2 mTorr of oxygen. The selectivity between silicon nitride and copper in SF₆ was the critical parameter for the etch to be successful.

In this process, 10 nm of copper was evaporated on the nitride and 70 nm of PMMA was spun over the copper. The wafer was then baked at 180 °C for one hour to drive out the solvents from the PMMA. The lines printed were 1 μm lines and they were developed in a 3:1 solution of isopropanol and methyl isobutyl ketone and rinsed with isopropanol. The first step consisted of transferring the pattern into the copper followed by RIE of the nitride in SF₆ and O₂. Based on the etch rates of copper in citric acid (33 nm per minute), the silicon nitride wafer was immersed in the citric acid solution for 18 seconds in order to etch 10 nm of copper. From the results however it was evident that the PMMA wasn't protecting the copper due to poor adhesion between copper and PMMA or copper and silicon nitride. The next process that was carried out was annealing the PMMA at its glass transition temperature which is 105 °C. Glass transition temperature of a polymer at which, the mechanical behavior of the polymer changes from rigid and brittle to tough and leathery and the behavior we define as plastic behavior. This was done in order to improve the adhesion between PMMA and copper. The PMMA was heated to its glass transition temperature after spin coating on 10 nm of copper and baking. This was followed by 5 minutes of citric acid etch to transfer the patterns from PMMA to copper followed by RIE in SF₆ and oxygen for 30 minutes to etch the nitride. From the results it was clear that the 1 μm lines were not straight and a certain degree of roughness existed. This roughness was a result of poor adhesion between PMMA and copper (or between copper and SiN_x) during the copper etch and the copper got exposed and the vast

majority of the copper were lost as a result of that. Even after annealing the PMMA to its glass transition temperature, the adhesion issue was not solved. The wet etch technique consisted of three steps: reactant transport to the surface, selective and controlled reaction of the film to be etched, and transport of byproducts away from the surface. The main drawbacks that affected pattern dimensions and prevented line width control were mainly, poor photoresist adhesion. This is what was experienced which led to the hard mask getting exposed and ultimately led to mask failure.

The unreliability of the wet etch led to the dry etch techniques for the mask fabrication process. This process chiefly consisted of two etching steps: the first being the argon milling step (or sputtering) to etch the patterns in the hard mask followed by reactive ion etching in SF_6 and oxygen to etch it into the SiN_x . Previous works have dealt with CF_4 and oxygen, but that process was too slow due to the etch chemistry of CF_4 where a polymer formation took place and subsequently slowed the etch process. In this work however only SF_6 and oxygen were used for the SiN_x etches. The choice of the hard mask is the key step in this process and also the selectivities between the hard mask and PMMA and also the selectivity between the hard mask and the SiN_x is also critical for the process to work. The role of the hard mask is that it protects the silicon nitride below it from getting exposed to the SF_6 and oxygen. That's why we need two pattern transfer processes instead of directly transferring the pattern from PMMA to the nitride. Previously, nickel, chromium, or palladium was used as the hard mask. Here palladium and copper were used to find out which metal would be used as the hard mask. The selectivity between copper and PMMA was 1.5 compared to that of 4.1 between palladium and PMMA in argon. Also the selectivity between copper and SiN_x was 200 compared to 135 between palladium and SiN_x . The argon milling step was carried out at a process pressure of 1 mTorr and at a power of 13 watts while the

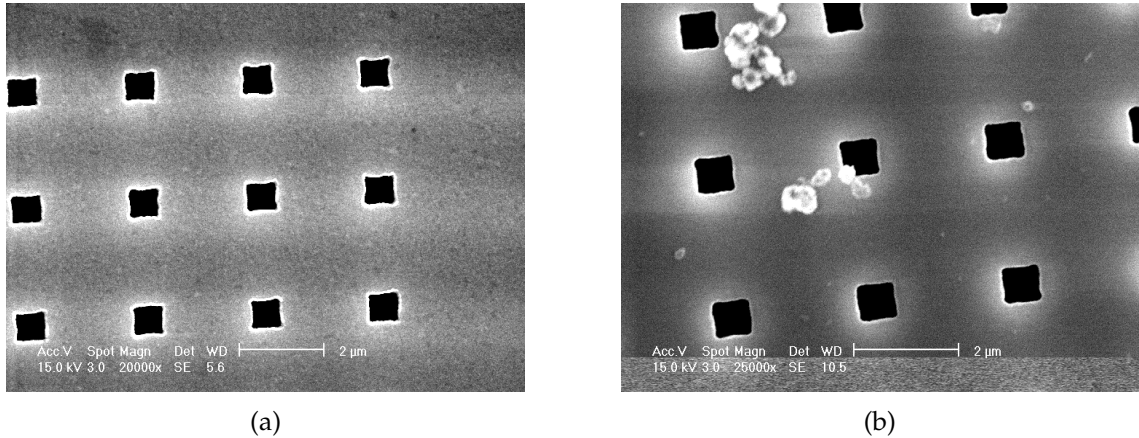


Figure 3.8. SEM image of (a) front side (b) back side of silicon nitride mask showing 700 nm square patterns.

RIE of SiN_x was carried out in 0.8 mTorr SF_6 and 0.2 mTorr of oxygen at 15 W. Based on the etch rate characterization for the two processes it was clear that copper should be chosen as the hard mask. After the membranes were made and coated with 20 nm of copper and 200 nm of PMMA, patterns ranging from 5 μm to 100 nm were printed on the membrane and developed using a 3:1 solution of isopropanol and methyl isobutyl ketone and rinsed with isopropanol. The first step consisted of etching the patterns into the copper layer by argon milling for 10 minutes followed by reactive ion etching in 0.8 mTorr SF_6 and 0.2 mTorr of oxygen for an hour to etch through the nitride membrane at a power of 15 watts. The reason for this hour long etch for a membrane is largely due to the fact that the membrane gets heated up due to its poor thermal conductivity and so the etch slows down. To overcome this the hour long etch was tried.

The unreliability associated with the wet etch was definitely overcome by the dry etching techniques. [Figure 3.8](#)(a) and (b) show the SEM images front and back side of a SiN_x mask with 700 nm etched square openings respectively where the patterns are clearly etched all the way into the SiN_x as no secondary electron signals are seen coming out of the etched openings implying high fidelity etch.

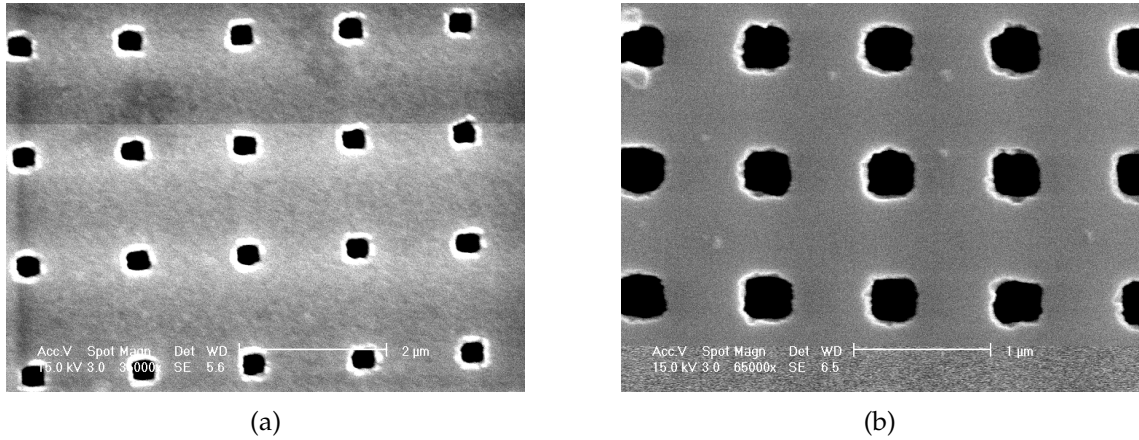


Figure 3.9. SEM image of (a) front side (b) back side of silicon nitride mask showing 300 nm square patterns.

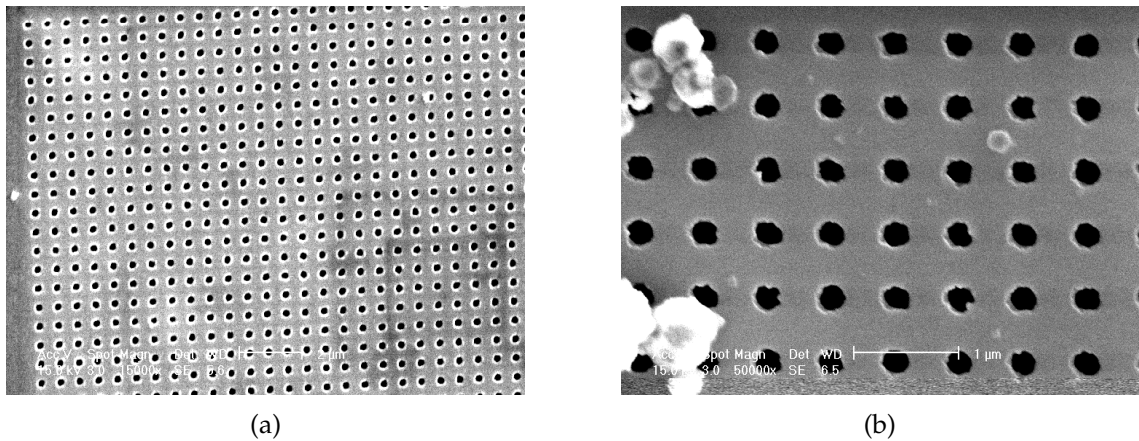


Figure 3.10. SEM image of (a) front side (b) back side of silicon nitride mask showing 200 nm square patterns.

Similar results are shown in [Figure 3.9\(a\)](#) and (b) with front and back images of 300 nm square openings respectively and in [Figure 3.10\(a\)](#) and (b) with front and back images of 200 nm square openings respectively. The biggest advantage of the dry etch process is that it does not suffer from poor photoresist adhesion problems which was in the case of wet etch. Also, the other noticeable thing about the dry etch process is that the etch profile is anisotropic in nature and generally gives straight etch profiles and practically suffers from no undercutting like the wet etch process. The significant challenge faced during this process was

the etch uniformity on the membrane due to the center of the membrane getting heated up by thermal conduction. Moreover, the entire lithography and pattern transfer processes were carried out on the SiN_x membrane itself rather than on the substrate. So, the yield of the process was questionable considering the fragile nature of the SiN_x membranes.

3.1.2 Other Notable Works on Stencil Masks

Apart from SiN_x stencil masks, stencil masks fabricated from silicon membranes were also implemented. Silicon membranes were fabricated using the electrochemical etch-stop technique [10]. With this technique, single-crystal membranes were produced from p-type substrates. Etching was carried out using anisotropic etching solutions such as KOH. A bias voltage was applied to the n-layer to form a reverse-biased junction. Electrical contact to the p type base wafer was maintained through the solution with the use of counter electrodes. Since the applied potential appeared across the junction, the p-type silicon remained at open circuit potential and etched as it would in the unbiased case. When the etching reached the junction, the silicon surface passivated due to the formation of an anodic oxide layer. Using this technique, large area membranes could be made with highly uniform thickness. Membranes have been made in diameters up to 95 mm (on 125 mm wafers) with thicknesses ranging from 1.5 to 5 μm .

Thin membranes 0.4 μm thick can be made with 25 mm diameters. Two types of membrane were processed. Firstly, large area samples with a circular membrane of 95 mm in diameter (on 125 mm wafers) and thicknesses between 2 and 5 μm and secondly, thin samples for high-resolution proximity printing, with a 1 cm^2 square membrane and 0.75 μm thickness. The high-resolution membranes had 90 nm thick evaporated SiO which oxidized to SiO_2 in the evaporator at room temperature. Resist patterns were defined by 30 kV electron beam lithography.

Reactive ion etching was carried out in a magnetically enhanced system. The evaporated SiO₂ was patterned by RIE in CBrF₃ at a bias potential of 130 V and a pressure of 2 mTorr. Silicon was then etched at a pressure of 1.25 mTorr and a self-bias potential of 90 V. The etch rate was 45 nm/min and the selectivity for silicon with respect to thermal SiO₂ is 65:1. However it was observed that there was some irregularity in the diameter of holes on this scale. This was due to ion scattering effects during RIE. The real drawback with the silicon membranes was that it required expertise in etching the membrane and the entire process was challenging. Due to this it was an unreliable process.

In another notable work with stencil masks, a polymer stencil mask made of poly(methyl methacrylate) (PMMA) was used for fabricating high-performance graphene devices by patterning the thin film of PMMA by e-beam lithography [11]. A patterned PMMA film as a free-standing stencil mask was fabricated by spin coating the resist, e-beam exposure, suspension, and drying. Firstly, a layer of 5% polyvinyl alcohol (PVA) in water was spin-coated onto a SiO₂/Si substrate at 100 rpm for 10 seconds, followed by 5000 rpm for 50 seconds, and then baked for 90 seconds at 110 °C. The PVA layer was a release layer that was dissolved in a water bath to release the PMMA resist layer from the substrate. Secondly, the PMMA resist was spin-coated on top of the PVA layer at 100 rpm for 10 seconds, followed by 5000 rpm for 50 seconds, and baked for 90 seconds at 100 °C. Then a TEM grid was placed on top of this PMMA layer and another PMMA layer was spin coated to increase the rigidity of the PMMA stencil mask and its adhesiveness to the TEM grid. After spin-coating the PMMA film, the pattern was written by exposure to e-beam lithography and developed. The sample was placed in DI water at 50 °C for 2 hours to dissolve the PVA layer and to release the PMMA layer from the substrate. The PMMA mask was aligned with the graphene flakes underneath and without additional alignment equipments. After alignment, 5 nm

of titanium and 55 nm of gold were e-beam evaporated as contacts through the PMMA mask. The simplicity of the fabrication process showed a lot of promise and it was implemented in our lab too for fabricating lithography masks.

3.2 Fabrication of PMMA Stencil Masks

The major drawbacks of the SiN_x stencil masks were that they were difficult to reproduce and the SiN_x membrane used to get heated up during the pattern transfer step into the copper using argon with PMMA as the masking layer. The reason being that the thermal conductivity of the SiN_x membrane is lower than the thermal conductivity of the SiN_x substrate. This resulted in the SiN_x membrane getting heated up during this step and as a result the PMMA would reflow if the temperature exceeded its glass transition temperature of 105 °C. The hypothesis was that the reflow of the PMMA would cause the patterns to distort and result in a low yield process. Silicon nitride stencil masks also required expertise in etching. However the transition to polymer membranes was seen as an alternative to overcome these limitations. PMMA (a positive tone resist) was initially used as the polymer to process these stencil masks. The real benefit of having PMMA membranes as stencil mask was that the patterns were produced as a result of exposing the PMMA to the e-beam lithography followed by developing and rinsing. There wouldn't be any pattern transfer steps when compared to the nitride mask fabrication process. The expectation was that the PMMA mask patterns would be very high quality in terms of resolution since they would be directly from the e-beam writer exposure. This was the key attribute we were trying to exploit in our process. Also the PMMA membranes of 500 nm thickness were found to be very robust and reproducible.

In this process as shown in [Figure 3.11](#), 300 nm PMGI was spin-coated on a silicon wafer as a release (lift off) layer, followed by 500 nm of PMMA. We

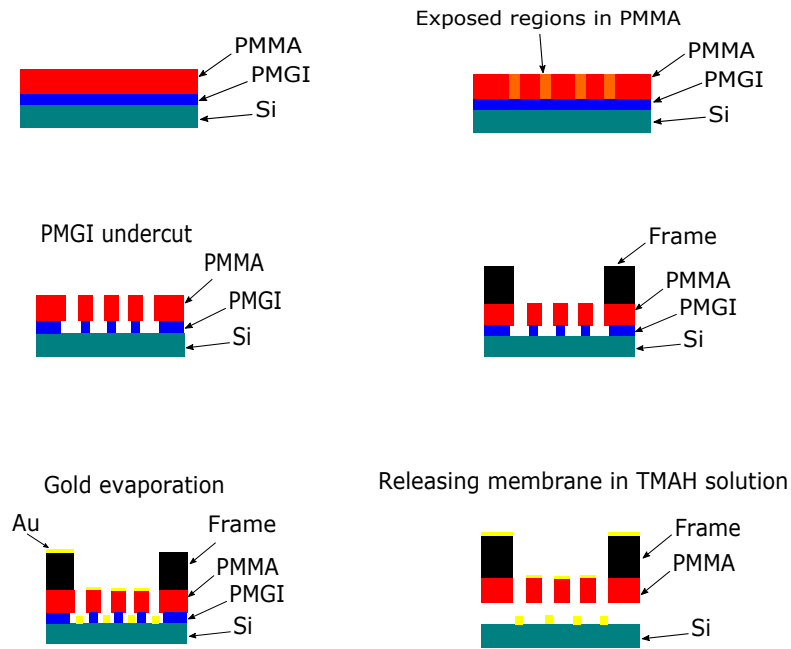


Figure 3.11. Initial flow diagram of PMMA stencil mask fabrication.

purchased 950PMMAC9 from Microchem Inc., which contains 9% solids dissolved in chlorobenzene. To spin-coat the film to the 300 nm thickness, we further diluted the solution with chlorobenzene with a 1:1 ratio, which allowed us to form the desired thickness with a 3000 rpm rotational speed. The PMMA was exposed by electron beam lithography and developed in a 2:1 solution of Isopropanol and DI water for 1 minute. The next critical step was to undercut the PMGI using TMAH solution. The significance of this step was to prevent clogging of the PMMA openings after the gold evaporation step. But one of the limiting factors of this process was to control the PMGI undercut. If the PMGI was completely removed, then the PMMA patterns collapse against the silicon wafer, which also results in the membrane collapsing. Incomplete clearing and undercut of the PMGI results in the clogging of the openings during the gold deposition. After the undercut process, a laser-cut acrylic frame of dimensions 0.8 cm by 0.8 cm was bonded to the PMMA PMGI stack with a 50 μm thick adhesive. The frame was set to rest for 40 minutes on the stack by pressurising with a heavy object to ensure a strong

bonding between the adhesive and the substrate. After this 100 nm of gold was evaporated on the PMMA. In the final step, the PMMA membrane is released from the substrate by immersing in a TMAH solution.

However as shown in [Figure 3.12](#) the effect of backscattered electrons during the e-beam exposure plays a significant role in determining the outcome of the process. Due to proximity effect the unpatterned areas of the PMGI underneath the PMMA receive an additional dose due to backscattered electrons. In [Figure 3.12](#) we see that R_O is the vertical etch rate of the PMMA using the developer and R_L is the lateral etch rate of the PMGI due to backscattered electrons in the TMAH release solution. Due to this lateral etching of the PMGI the undercut is very difficult to control and leads to an unreliable and low yield process where the PMGI gets completely removed and the PMMA membrane collapses. Due to the downside of the PMGI undercut step which is difficult to control and reproduce an alternative process was designed to fabricate PMMA masks.

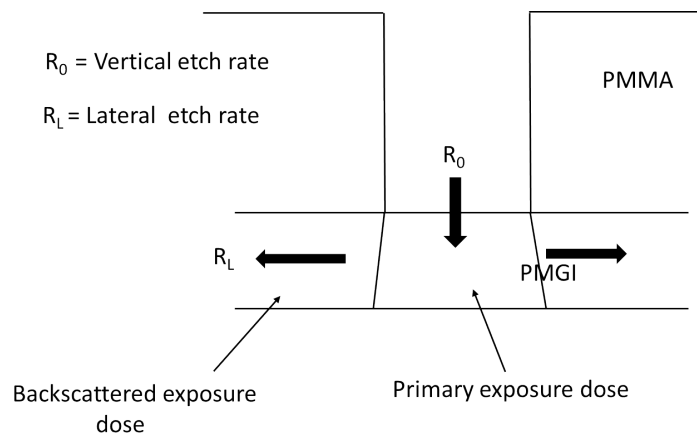


Figure 3.12. Effect of backscattered electrons on PMMA PMGI bilayer.

In a new process, shown in [Figure 3.13](#) 300 nm PMGI is spin-coated on a silicon wafer as a release (lift off) layer followed by 500 nm of PMMA. The PMMA is exposed by electron beam lithography and developed as in the previous process and an acrylic frame is bonded to the stack. Next the PMMA membrane is released

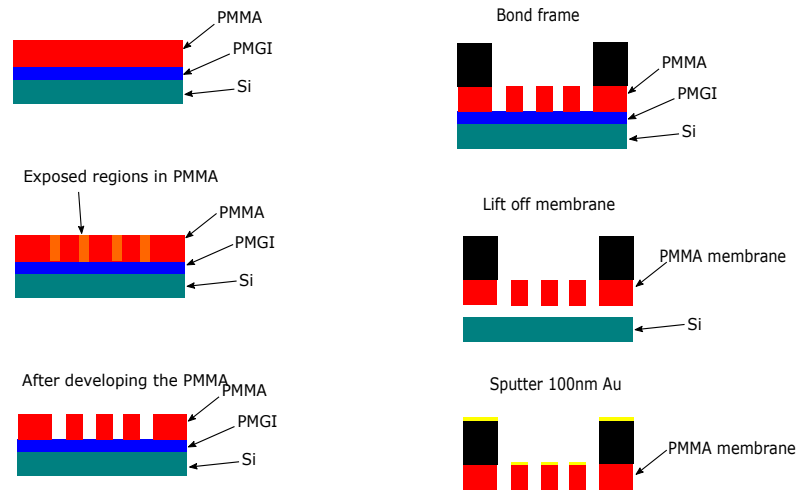


Figure 3.13. Final flow diagram of PMMA stencil mask fabrication.

by dissolving the release layer (PMGI) in TMAH solution. Finally, 100 nm of gold is thermally evaporated. However, after inspecting the patterns, the patterns were heavily distorted due to PMMA reflow during the thermal evaporation step. Since the glass transition temperature of PMMA is around 105 °C, the excessive heat from the evaporation step causes the polymer to reflow and hence the patterns were distorted. Therefore an alternative approach was to sputter deposit the 100 nm gold. The 100 nm of gold was sputter deposited in the cleanroom in the sputtering tool. The SEM images of the front and back of the PMMA mask was taken after sputter deposition.

From the SEM images of the front and back of the PMMA mask as shown in [Figure 3.14\(a\)](#) and [\(b\)](#) respectively, we see that the 200 nm plus sign patterns are rounded at the edges implying that there was some reflow of the PMMA during the sputtering process as well. Similarly, the 300 nm plus sign patterns are rounded at the edges as seen from the front and back SEM images of the mask in [Figure 3.15\(a\)](#) and [\(b\)](#) respectively. Hence we can conclude that sputtering improves the process compared to thermal evaporation of gold but there is some amount of PMMA reflow that does take place signifying that the polymer does

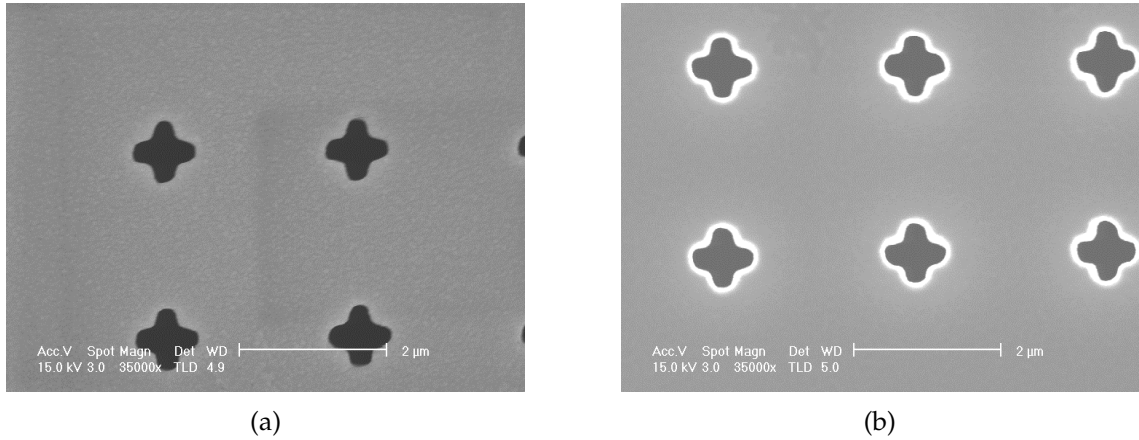


Figure 3.14. SEM image of (a) front side and (b) back side of a 500 nm PMMA mask showing 200 nm plus sign with an aspect ratio of 4.

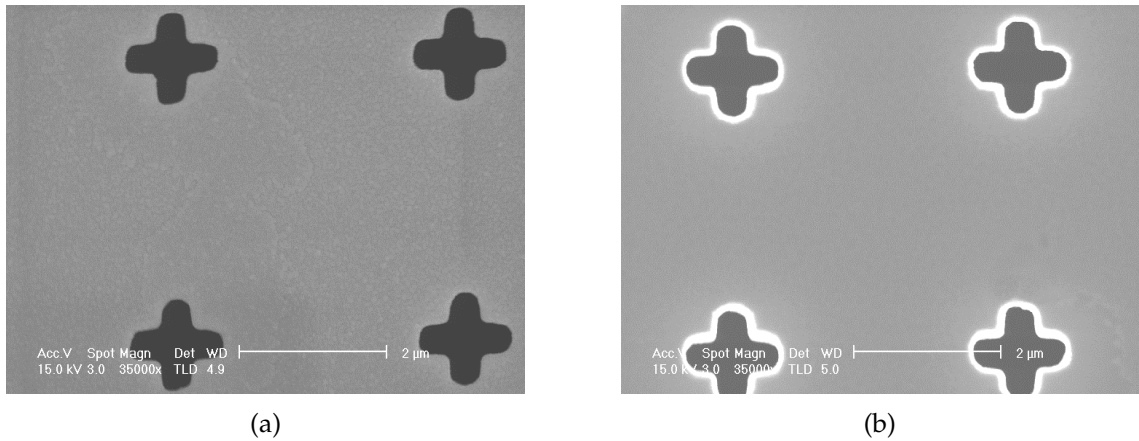


Figure 3.15. SEM image of (a) front side and (b) back side of a 500 nm PMMA mask showing 300 nm plus sign with an aspect ratio of 4.

get overheated around its glass transition temperature even during the sputtering step. Therefore the PMMA masks, with as much promise as they showed in the simplicity of the fabrication, were not particularly reliable and were abandoned.

3.3 SU-8 Stencil Masks

Due to the drawbacks of the PMMA mask process involving controlling the PMGI undercut, SU-8 was chosen as an alternative material to design the stencil membranes. In SU-8 stencil masks, the SU-8 is not exposed to the e-beam writer

and hence the PMGI underneath does not receive any additional proximity dose. The process flow diagram in this chapter describes that aspect.

3.3.1 Fabrication of 500 nm SU-8 Stencil Masks

Initially, 500 nm of SU-8 was considered to be the membrane thickness because 500 nm PMMA was found to be mechanically robust and henceforth the hypothesis was that 500 nm of SU-8 would be equally robust, if not more. We were using Microchem SU-8 2005 which was diluted to 1:2 ratio with the solvent cyclopentanone and spun at 3000 rpm to get the desired thickness. The original stock concentration of Microchem SU-8 2005 was 45% by solids for 5 μm thickness at 3000 rpm. The 500 nm SU-8 solids concentration is 14%. Therefore SU-8 2005 was diluted to 1:2 ratio to get the desired thickness at 3000 rpm. The SU-8 mask fabrication sequence consisted of coating a three-inch polished silicon wafer with 300 nm release layer PMGI, 500 nm thick SU-8 layer, 40 nm of copper and 100 nm PMMA as the resist.

As seen in [Figure 3.16](#) the first step consists of patterning the PMMA (lithographic step) followed the development of the resist. The lithography was carried out by electron beam lithography system. An acrylic frame was bonded on the substrate prior to the pattern transfer steps. After that the patterns were transferred into the copper in an argon milling step where the energy of the ion beam is 600 V and the beam current is 120 mA. The final pattern transfer step consisted of reactive ion etching into SU-8 in oxygen plasma at a power of 30 W and ion energy of 250 V. The rates of PMMA and copper in argon were measured to be 35 nm/min and 30 nm/min, respectively, suggesting that the selectivity is about 1:1. However, prior to running the oxygen etch of SU-8 with copper as the hard mask, the RIE chamber was conditioned with SF_6 plasma for a couple of hours to reduce the copper rates and improve the selectivity as explained in Chapter

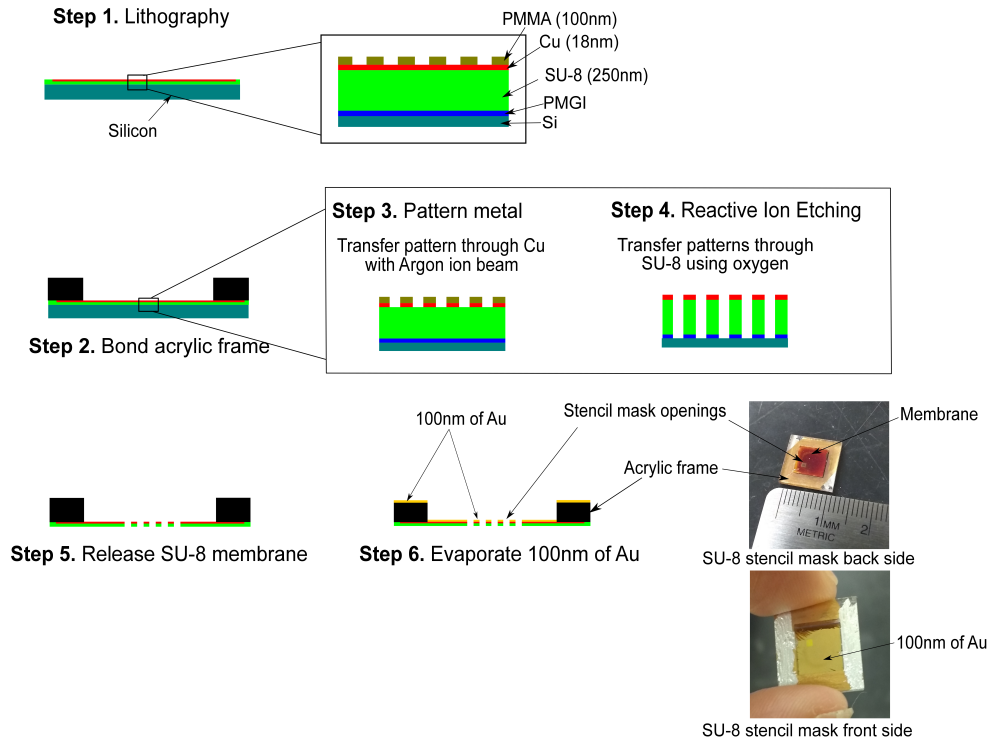


Figure 3.16. SU-8 mask fabrication process flow using copper as hard mask.

2. After the pattern transfer was complete, the free standing SU-8 membrane supported by an acrylic frame was formed by dissolving the PMGI in TMAH solution. Finally, 100 nm of gold was thermally evaporated on the SU-8 membrane. Unlike PMMA, fully cross-linked SU-8 has a glass transition temperature greater than 200 degree centigrade. Thus SU-8 does not reflow as the PMMA masks did. That was a major improvement in the mask fabrication process. The membrane area is $0.7 \times 0.7 \text{ cm}^2$ and the patterned area is 1 mm^2 . The patterns were written by the e beam writer at two separate current settings of 1 nA and 10 nA.

From the SEM image as shown in Figure 3.17(a) and (b) we see that the front and back side images of the 200 nm plus sign patterns written with 1 nA current have sharper edges compared to the front and back side images of the 100 nm plus signs written with 10 nA current in Figure 3.18(a) and (b) respectively where the edges of the plus signs are rounded, implying that the lower spot size in the e-beam

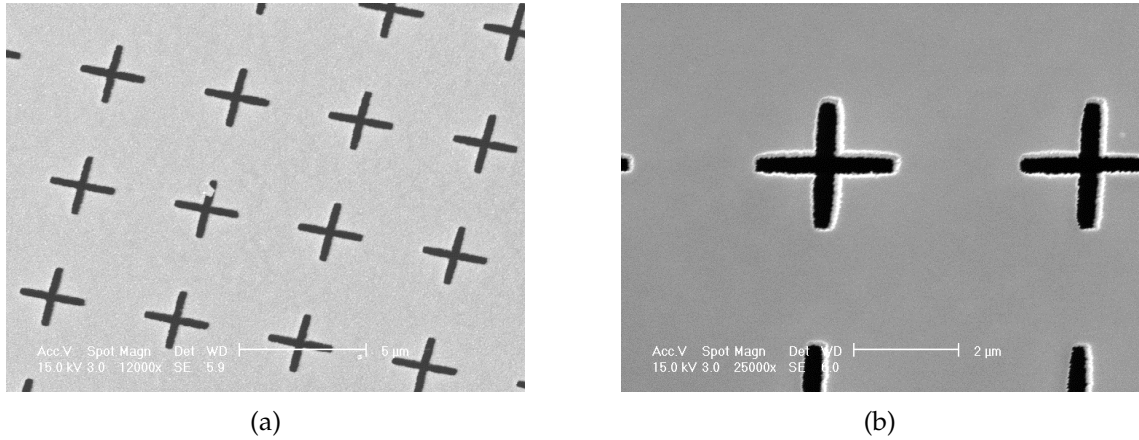


Figure 3.17. SEM image of (a) front side and (b) back side of a 500 nm SU-8 mask showing 200 nm plus sign with an aspect ratio of 12 written at a current of 1nA.

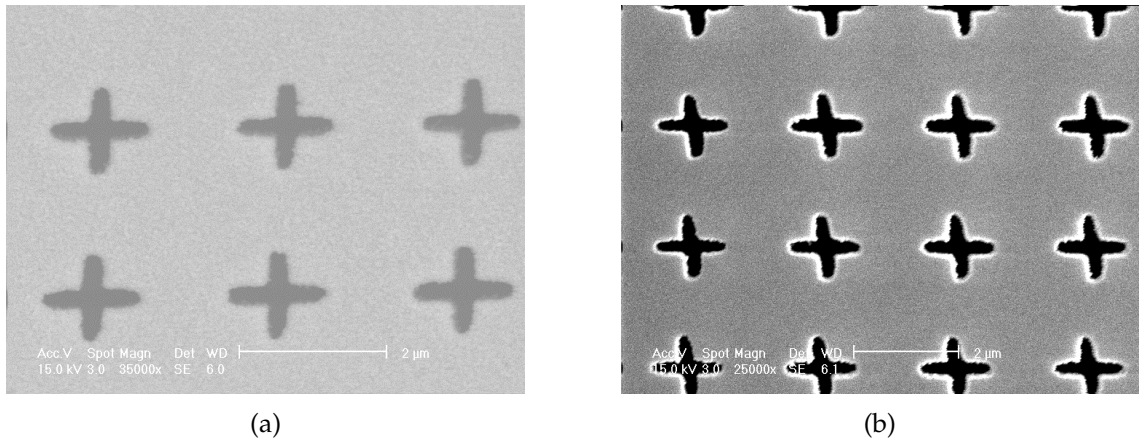


Figure 3.18. SEM image of (a) front side and (b) back side of a 500 nm SU-8 mask showing 100 nm plus sign with an aspect ratio of 12 written at a current of 10nA.

writer improves the resolution of the patterns. In [Figure 3.19\(a\)](#) and [\(b\)](#) we see the front and back side SEM images of a chiral pattern which, due to improper rinsing of the stencil mask, has a residue clogging over the pattern area. We hypothesize that the residue could be either the TMAH solution or some of the un-etched release layer (PMGI) could be clogging the patterned areas. As a result, we used a second rinsing step in TMAH solution where both the front and back side of the released membrane was immersed for 15 minutes each followed by immersing in room temperature DI water for a few hours. The temperature of the TMAH

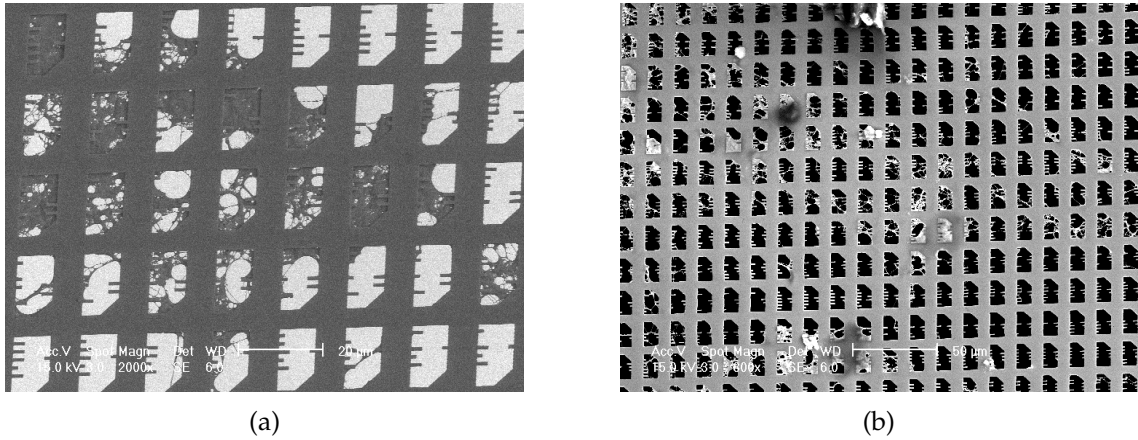


Figure 3.19. SEM image of (a) front side and (b) back side of a 500 nm SU-8 mask showing chiral patterns written at a current of 10nA.

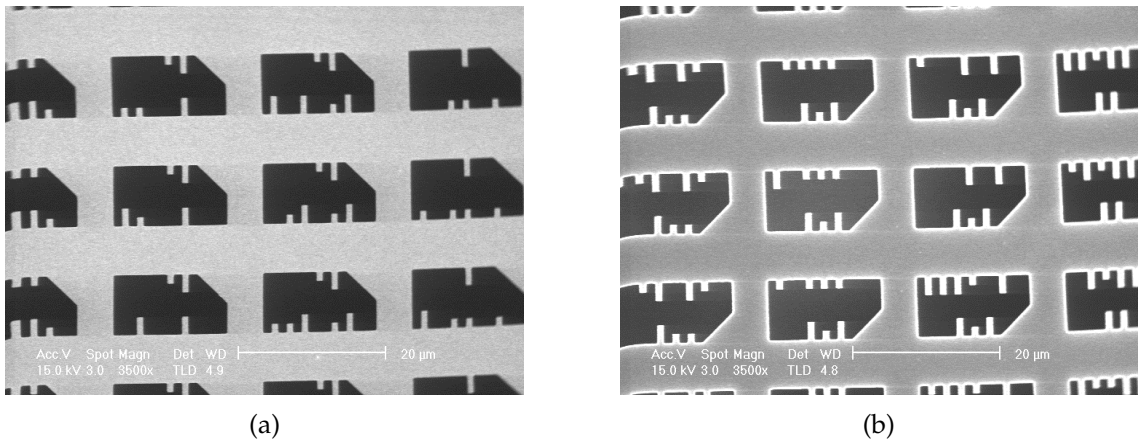


Figure 3.20. SEM image of (a) front side and (b) back side of a 500 nm SU-8 mask showing chiral patterns written at a current of 10nA after proper rinsing.

solution baths were set at 40 °C. This improved the rinsing process drastically and the future mask patterns did not have the same problem as encountered here as seen in [Figure 3.20](#)(a) and (b) where both the front and back side SEM images of the same chiral patterns do not have any residue clogging over the pattern areas.

3.3.2 Fabrication of 250 nm SU-8 Stencil Masks

3.3.2.1 Fabrication of 250 nm SU-8 Stencil Masks Using Copper as the Hard Mask

We observed that a 500 nm SU-8 membrane is more mechanically robust than a 500 nm PMMA membrane. Therefore, the Microchem SU-8 2005 was diluted to 1:4 ratio with the solvent chlorobenzene and spun at 3000rpm to get 250 nm. A few blank 250 nm SU-8 membranes were released and were found to be just as robust as 500 nm of PMMA. The reason for lowering the thickness was to overcome the aspect ratio dependant RIE while etching small features through 250 nm SU-8 as opposed to 500 nm. The process flow for 250 nm SU-8 masks was exactly the same as the 500 nm process as shown in [Figure 3.16](#). Only difference is that the thickness of copper used as hard mask was 20 nm instead of 40 nm for the previous process. We etched 250 nm SU-8 masks as per the process flow and inspected the patterns in the SEM. [Figure 3.21](#)(a) and (b) show the front and back side of the mask respectively having 100 nm plus signs with an aspect ratio of 12 implying the length of the arms of the plus sign is 12 times its width. Similarly, [Figure 3.22](#)(a) and (b) show the front and back side of the mask respectively having 50 nm plus signs with an aspect ratio of 4 and [Figure 3.23](#)(a) and (b) show the front and back side of the mask respectively having 75 nm plus signs with an aspect ratio of 10. In all the images we see the edges of the plus signs are very sharp and have no rounding associated with them implying high resolution e-beam patterning with 1 nA beam current.

This 250 nm stencil mask was used to print patterns using the atom beam proximity lithography on a substrate consisting of 300 nm PMGI and 100 nm PMMA. The patterns were printed on the PMMA and developed in 3:1 MIBK:IPA for 30 seconds followed by rinsing in IPA for another 30 seconds. The PMGI was

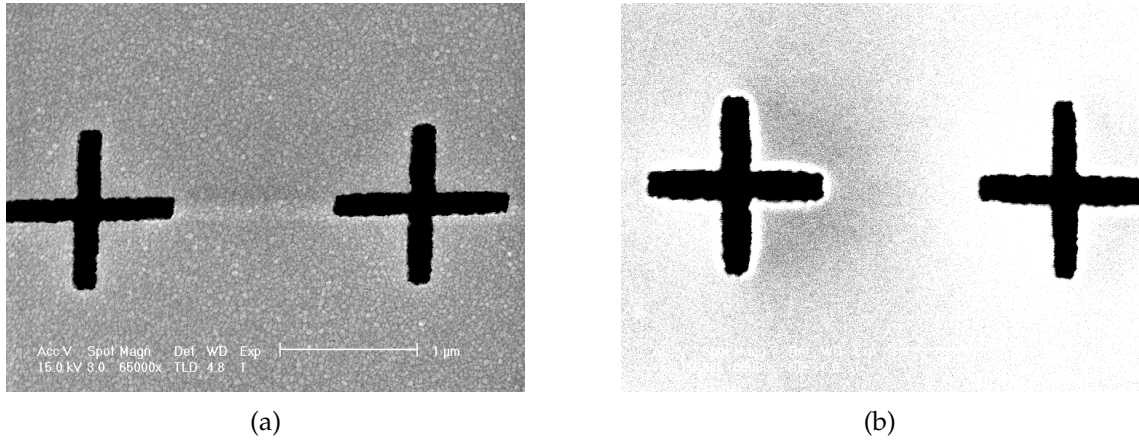


Figure 3.21. The (a) front side and (b) back side of 250 nm SU-8 mask showing 100 nm plus sign pattern with aspect ratio of 12.

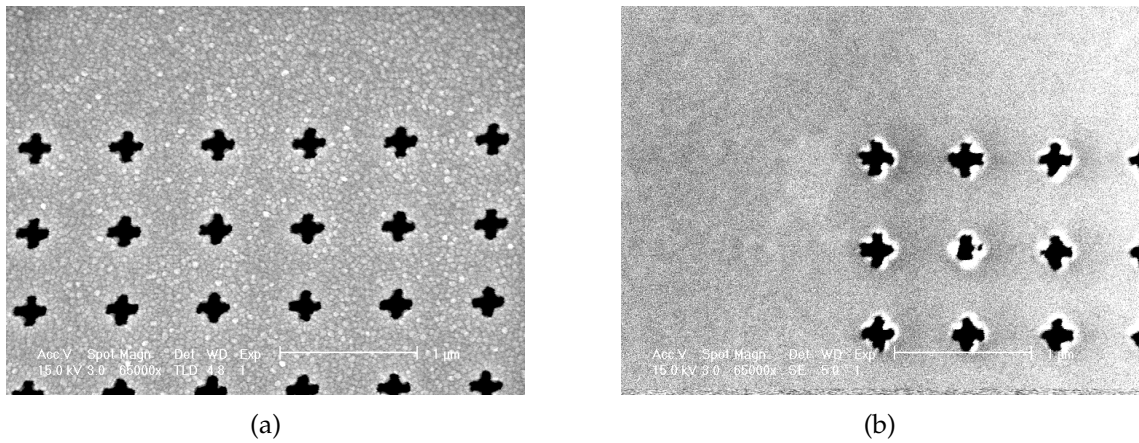


Figure 3.22. The (a) front side and (b) back side of 250 nm SU-8 mask showing 50 nm plus sign pattern with aspect ratio of 4.

undercut in TMAH for 20 seconds and 20 nm of gold was thermally evaporated. The PMMA was etched off in acetone and we were left with the gold on the developed patterns on the PMGI. From [Figure 3.24\(a\)](#) and (b) we see that the resulting printed images of 75 nm and 100 nm plus signs respectively have a same rounding due to blur at the edges. The edges of the plus signs have an element of rounding which results in the image being blurred. The resolution of the atom beam lithography system is limited by the finite source size which casts a shadow on the edge of the mask openings resulting in a blur. The blur (*b*) is the full-width

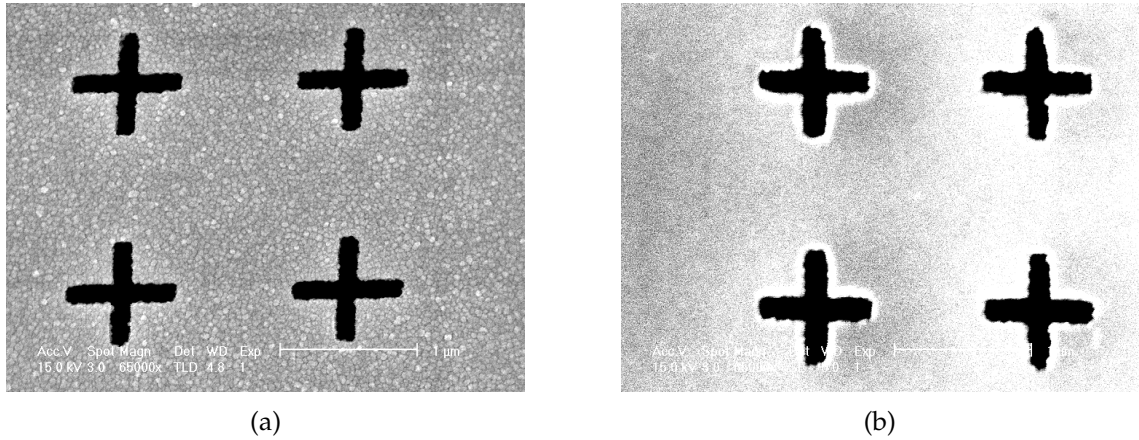


Figure 3.23. The (a) front side and (b) back side of 250 nm SU-8 mask showing 75 nm plus sign pattern with aspect ratio of 10.

at half-maximum (FWHM) of the image distribution and is given by

$$b = \frac{g}{l} \cdot \text{FWHM}, \quad (3.1)$$

where g is the gap and l is the beamline length. [Figure 3.25](#) shows the formation of blur due to the finite source size. The blur is essentially a one to one projection of the FWHM of the source. The resolution of the patterns printed with a gap is given by

$$R = k_1 \sqrt{\lambda g}, \quad (3.2)$$

where λ is the wavelength of the atoms and k_1 is a constant and g is the gap. The significance of this equation is that since the order of the wavelength is very small for atoms and by printing with a 50 nm gap we are not printing the patterns at the diffraction limit.

In order to analyze each of the pattern transfer steps the same process was carried out on a separate sample with the entire mask fabrication stack except that the membrane wasn't released. [Figure 3.26\(a\)](#) shows the 100 nm plus sign patterns after e-beam lithography and development in 2:1 IPA:DI water. The plus signs

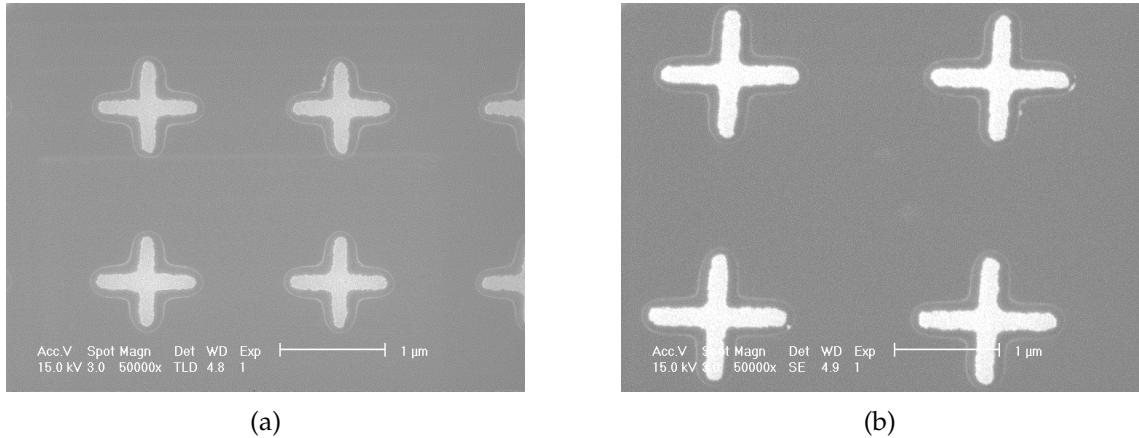


Figure 3.24. Printed image of (a) 75 nm plus sign pattern with aspect ratio of 12 and (b) 100 nm plus sign pattern with aspect ratio of 12 using a 250 nm SU-8 mask in the atom beam lithography tool after removing PMMA and evaporating 20 nm gold.

appear very close to the nominal linewidths with high resolution patterning at 1 nA current. [Figure 3.26\(b\)](#) shows the patterns post argon milling and we can observe that the linewidths of the 100 nm plus signs are larger than the ones seen in [Figure 3.26\(a\)](#). [Figure 3.26\(c\)](#) shows the patterns post RIE in oxygen and we can observe that the linewidths of the 100 nm plus signs remain larger than the nominal size as in [Figure 3.26\(b\)](#). [Figure 3.26\(d\)](#) show the patterns post 100 nm gold evaporation and we can observe that the linewidths of the 100 nm plus signs actually shrink and appear smaller compared to [Figure 3.26\(b\)](#) and [Figure 3.26\(c\)](#). This is due to the fact that the patterns shrink by 50 nm after evaporating 100 nm gold on the side of the mask consisting of the patterned area.

In [Figure 3.26\(b\)](#) we observe that the patterns after the argon milling have an increase in the linewidth of around 80 nm as per our data analysis where the approximate width of the patterns were examined using ImageJ. This is largely attributed by the milling process which involves faceting at the edges of the pattern and subsequently increases in the linewidth due to ion bombardment at an angle. The concept is demonstrated in [Figure 3.27](#). After the RIE step the patterns remain wider by the same margin indicating that the limiting step of this process is the

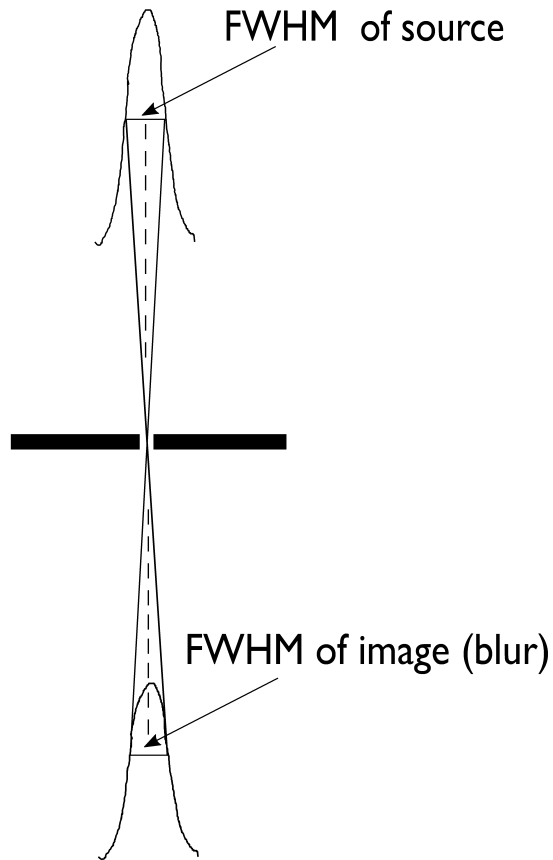


Figure 3.25. Diagram showing the formation of blur in helium atom beam proximity lithography.

ion milling step. Data was collected from each of the process steps and the width of the patterns after argon milling came out to be 175 nm which roughly remained the same at 172 nm after oxygen RIE but reduced to 119 nm after 100 nm gold evaporation. So, as per the measurements from the data it was evident that the argon milling step caused the patterns to increase by around 75 to 80 nm.

3.3.2.2 Fabrication of 250 nm SU-8 Stencil Masks Using Tungsten as the Hard Mask

Due to the challenges encountered due to the ion milling step as described in the previous sub-section, where the etched patterns had an increase in linewidth

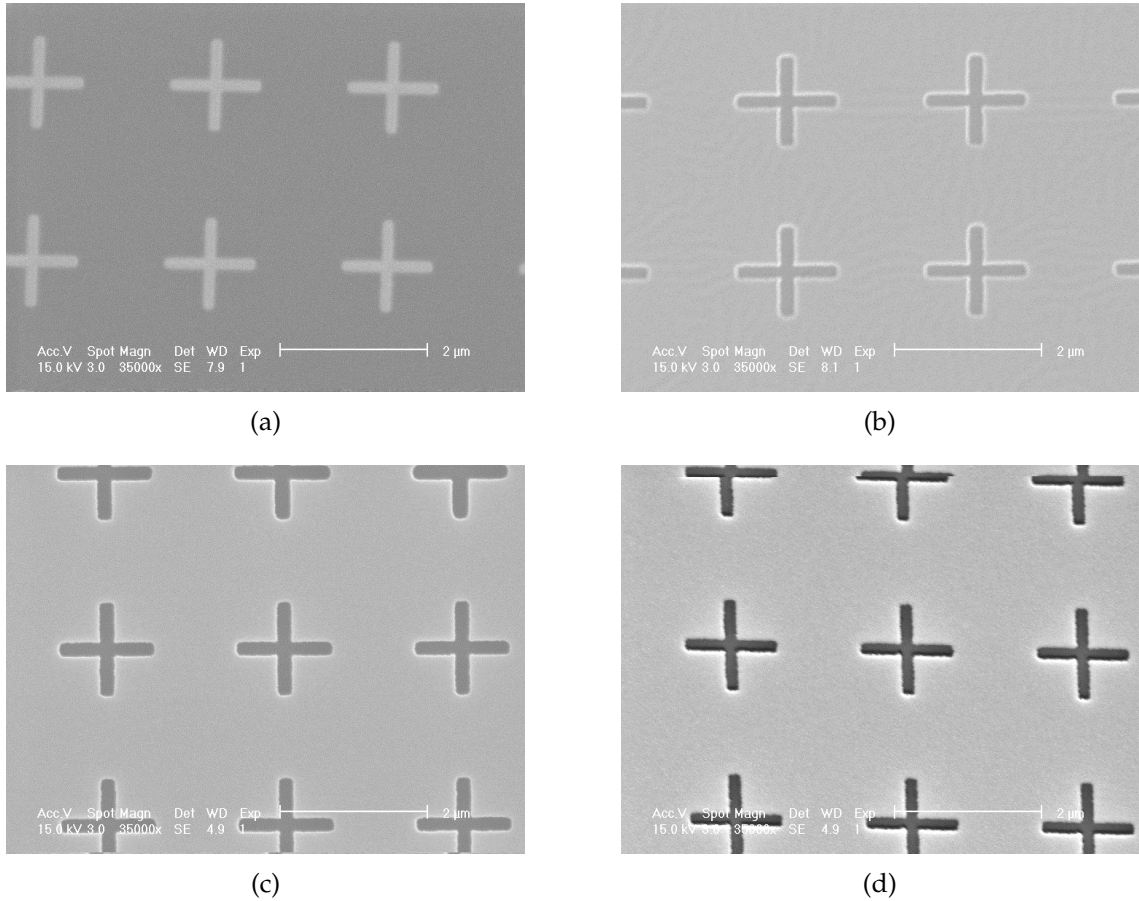


Figure 3.26. SEM image of 100 nm plus sign pattern with aspect ratio of 12 after (a) lithography and development (b) argon milling (c) RIE in oxygen and (d) 100 nm gold evaporation.

by 80 nm, tungsten was used as the hard mask. The purpose of using tungsten was to eliminate the ion milling process and to employ two RIE steps in the lens fabrication process. The new mask fabrication sequence, as shown in [Figure 3.28](#) consisted of coating a three-inch polished silicon wafer with a release layer PMGI, a 250 nm thick SU-8 layer, 10 nm of tungsten and 100 nm PMMA as the resist (imaging layer). The first step consisted of exposing the stack to the atom beam proximity printer using a stencil mask with test patterns on it. This was followed by reactive ion etch step in SF₆ plasma for 40 seconds at 15 W and RIE into SU-8 in the oxygen plasma for 3 minutes at 30 W which accounted for a 50% over etch into the SU-8. An acrylic frame was bonded on the substrate prior to the pattern

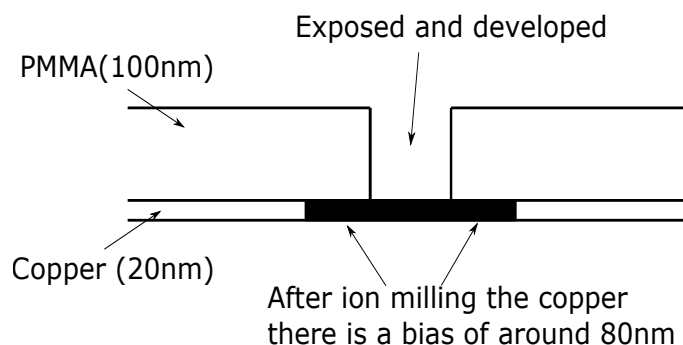


Figure 3.27. Schematic diagram showing the effect of increase in linewidth by ion milling.

transfer steps. The selectivity between tungsten and SU-8 was measured to be around 240 in the oxygen RIE. After the pattern transfer was complete the free standing SU-8 membrane supported by an acrylic frame was released by dissolving the PMGI in TMAH solution.

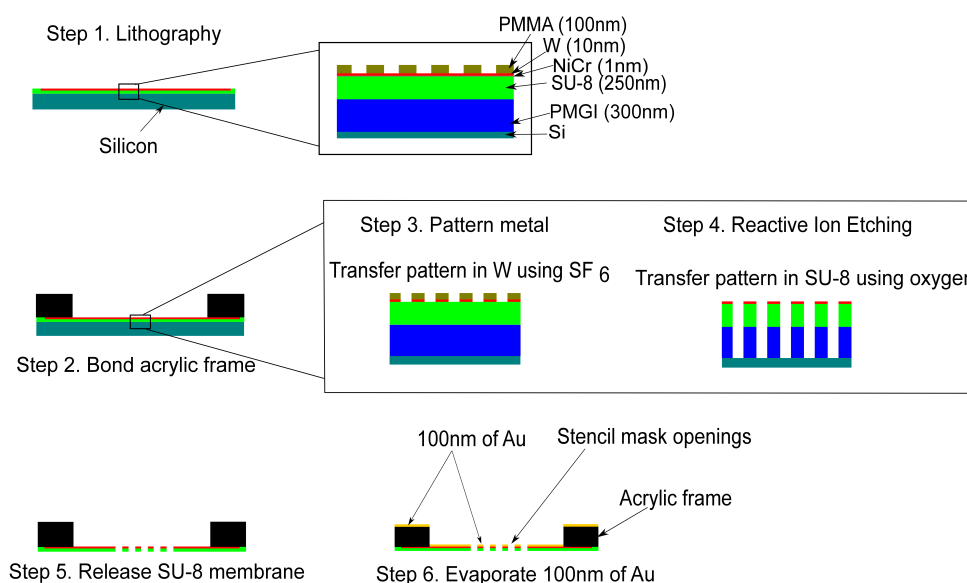


Figure 3.28. Flow diagram of SU-8 stencil mask fabrication using tungsten as the hard mask.

Figure 3.29(a) shows that the resulting etched chiral patterns suffer from micro-masking, which resulted in the formation of long un-etched regions that

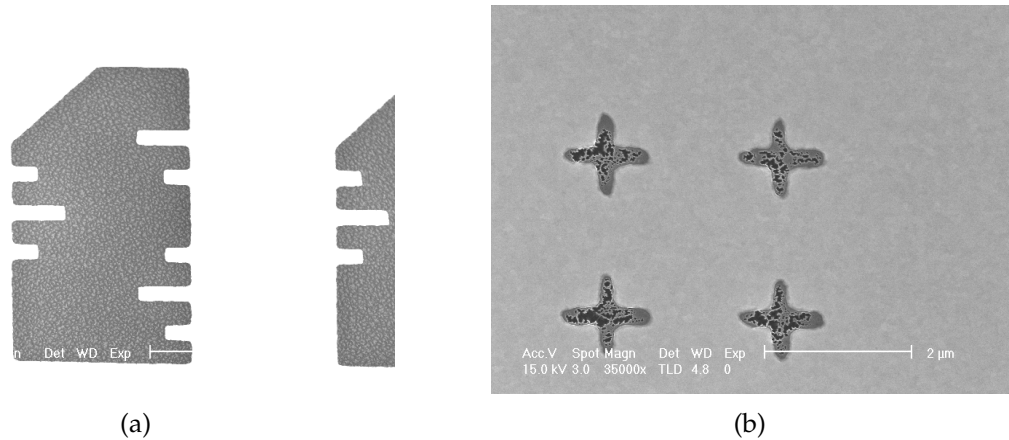


Figure 3.29. SEM image of (a) chiral patterns after 40 seconds of SF_6 and (b) 100 nm plus signed patterns after 40 seconds of SF_6 etch.

protrude outwards. The entire etched area in the pattern has a dense region of micro-masked features. [Figure 3.29\(b\)](#) shows a 100 nm plus sign where the features are not etched all the way through. This most probably is the result of incomplete tungsten etching in the SF_6 RIE. Therefore, another sample was processed using the same conditions with the only difference being that the SF_6 etch was 50 seconds instead of 40 seconds. In [Figure 3.30\(a\)](#) and (b), we see the effect of micro-masking in the features. However, increasing the SF_6 RIE from 40 seconds to 50 seconds improved the pattern transfer in the tungsten significantly. During the ion milling step, if the hard mask was not completely milled, it left behind long protrusions resulting in defects as seen in [Figure 3.31](#) and during the RIE process the incoming ions reflect off these protrusions and hence these defects are left behind and are un-etched. This is the cause of micro-masking effect. Therefore to overcome this effect an intermediate argon milling step was carried out for 30 seconds and 1 minute at 30 W after the 50 seconds SF_6 RIE. The SEM images of the chiral patterns and 100 nm plus sign patterns with 1 minute and 30 seconds argon milling are shown in [Figure 3.32\(a\)](#) and (b) respectively where we see that the longer milling time of 1 minute results in more micro-masking and more dense un-etched defects

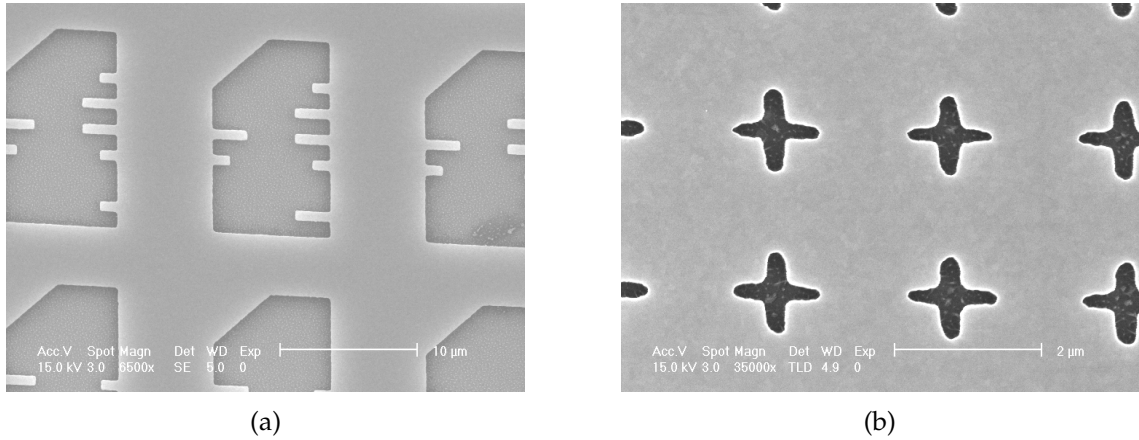


Figure 3.30. SEM image of (a) chiral patterns after 50 seconds of SF₆ and (b) 100 nm plus sign patterns after 50 seconds of SF₆ etch.

between the pattern regions than the shorter 30 second milling time. In order to inspect the patterns more precisely the samples were tilted in the SEM and from [Figure 3.32\(c\)](#) and (d) we see that the effect of micro-masking is more pronounced in the sample which had undergone 1 minute of intermediate argon milling than the sample with 30 seconds of intermediate milling time to clear the defects. Hence, another test sample was conducted with the whole stack and a dose series was written on the resist using e-beam lithography. After developing the patterns in 2:1 IPA:water solution, the patterns were etched into tungsten in SF₆ plasma for 50 seconds at 15 W followed by 30 seconds of argon milling at 30 W and finally oxygen RIE into the SU-8 for 3 minutes (50 percent over-etch) at 30 W. A 100 nm thick layer of gold was thermally evaporated on the samples and inspected in the SEM.

From the SEM images shown in [Figure 3.33\(a\)](#), (b) and (c), we see that the patterns written in the e-beam writer were 50 nm, 75 nm and 100 nm respectively. The challenges observed in the process involving copper milling where the patterns appeared larger by around 80 nm was overcome in this process where the 50 nm, 75 nm and 100 nm wide plus sign patterns had final dimensions of 58 nm, 80 nm

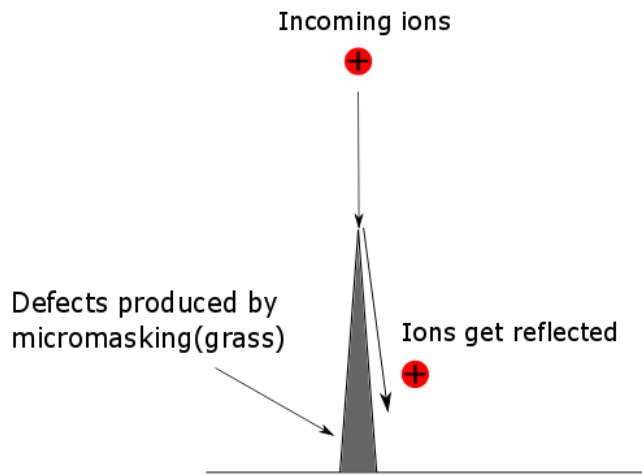


Figure 3.31. Schematic diagram showing the micromasking effect.

and 108 nm respectively, as seen in [Figure 3.33\(a\)](#), (b) and (c). We can conclude that the two RIE steps involving SF_6 plasma and oxygen plasma overcomes the drawbacks associated with the increment in linewidth associated with ion milling. Hence, another sample with the entire stack was exposed to the e-beam writer and different circles of varying diameter were patterned and developed. After development in a 2:1 IPA:water solution, the acrylic frame was bonded and the patterns were etched into tungsten in SF_6 plasma for 50 seconds at 15 W, followed by 30 seconds of argon milling at 30 W, and finally, oxygen RIE into the SU-8 for 3 minutes (50 percent over-etch) at 30 W. The membrane was released as a stencil mask after immersing in TMAH solution followed by thorough rinsing as previously explained. Finally, 100 nm of gold was thermally evaporated on the mask.

[Figure 3.34](#) is a top down tilted front side image of a SU-8 mask with 700 nm etched patterns where we see that there is some un-etched material that is left over on the base of the etched features. The image was tilted at 30 degrees and

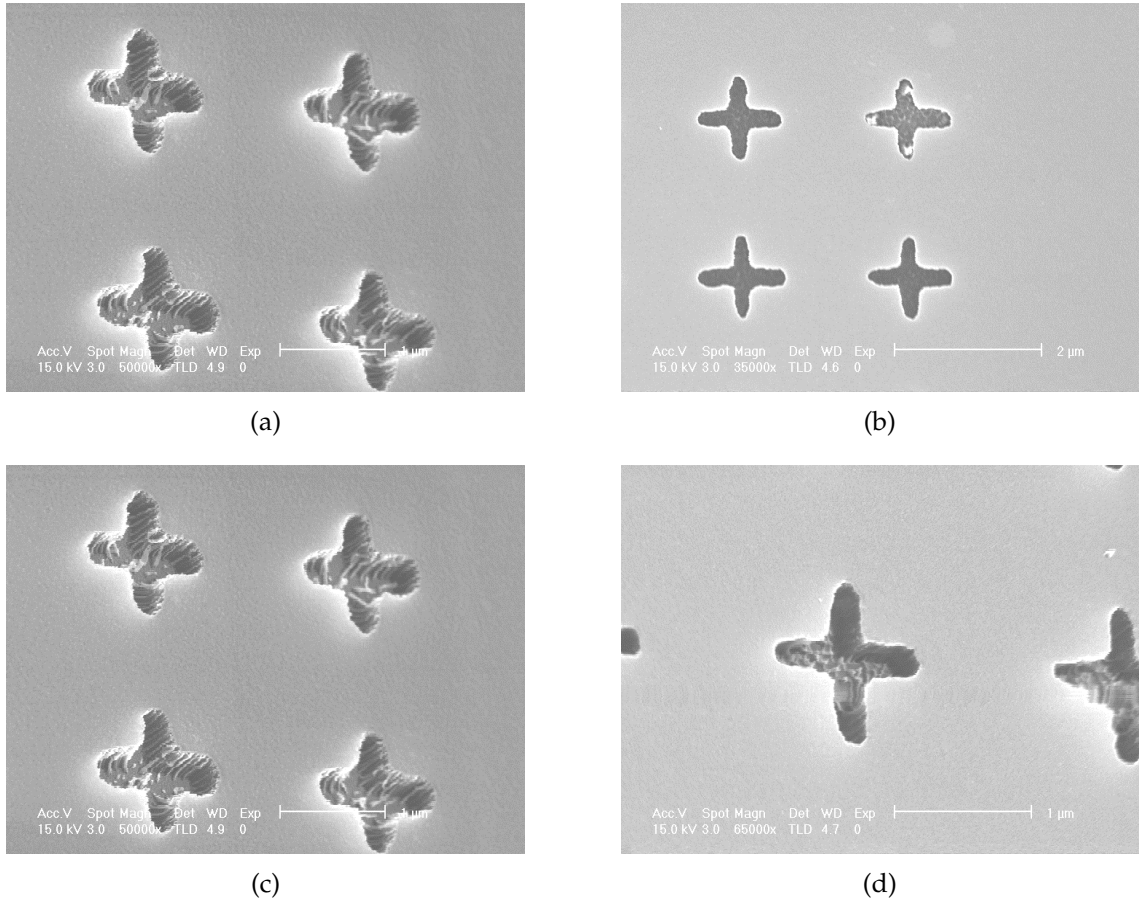


Figure 3.32. SEM image of 100 nm plus sign patterns (a) with 1 minute intermediate argon milling step (b) with 30 seconds intermediate argon milling step (c) with 1 minute intermediate argon milling step and tilting the sample and (d) with 30 seconds intermediate argon milling step and tilting the sample.

the actual height of the etched feature in the SEM is calculated to be 120 nm. Since we evaporated 100 nm of gold on the front side of the mask, the total depth of the etched feature was approximately 220 nm. Our hypothesis was that the 250 nm of SU-8 did not faithfully etch all the way in oxygen RIE and the cause of this slowdown could be that the tungsten hard mask did not etch resulting in the slowdown of the SU-8 RIE in the subsequent step. We carried out several experiments where we characterised tungsten and PMMA rates in SF₆ RIE at 15 W. The tungsten rates measured during these experiments were varying a lot, as is seen in [Figure 3.35\(a\)](#) and (b), where the range of the rates was between

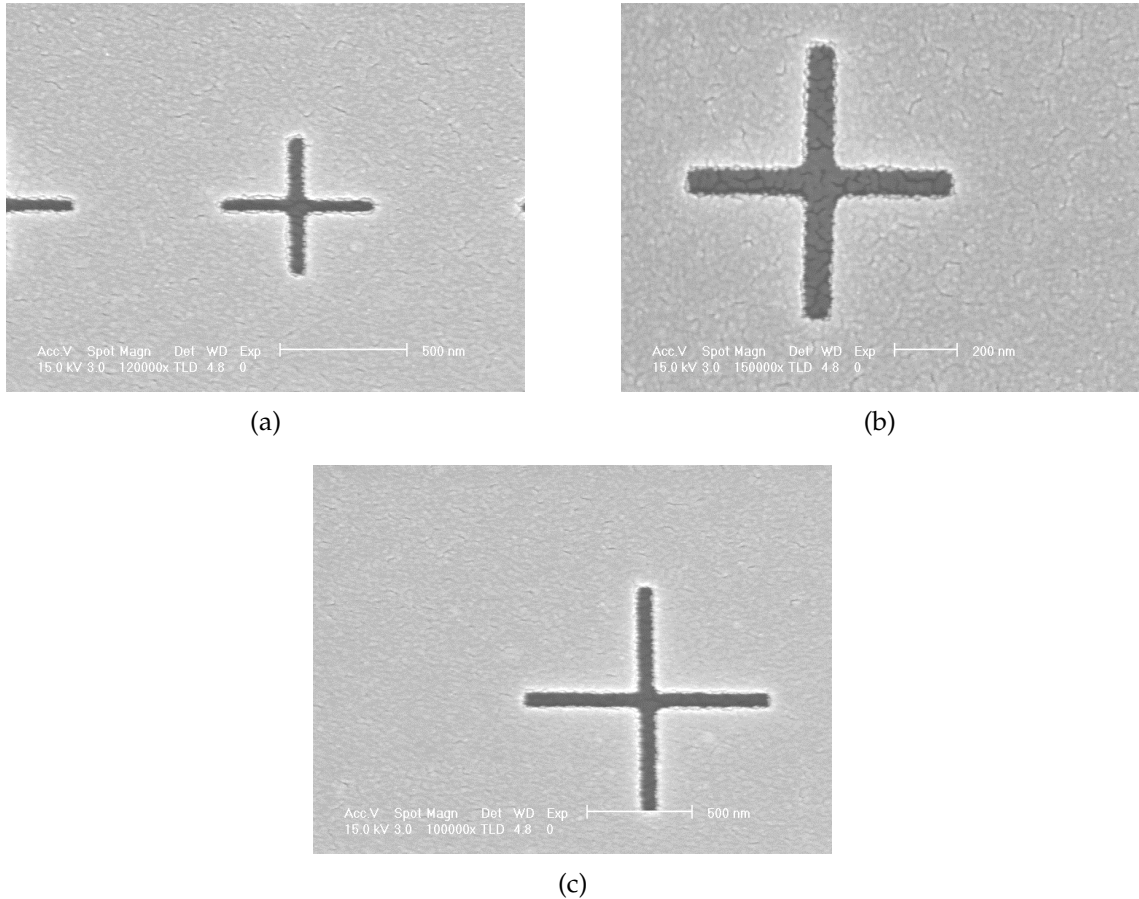


Figure 3.33. SEM image of e beam written and etched (a) 50 nm plus sign patterns with an intermediate argon milling step for 30 seconds (b) 75 nm plus sign patterns with an intermediate argon milling step for 30 seconds and (c) 100 nm plus sign patterns with an intermediate argon milling step for 30 seconds.

40 nm/min to 140 nm/min. The PMMA rates, however, were relatively stable, between 90 nm/min to 110 nm/min. The selectivity (ratio of the PMMA rate to tungsten rate) was also varying quite a lot between 0.5 to 2 as seen in [Figure 3.35\(c\)](#) and (d).

Our hypothesis was that the cause of the incomplete RIE of SU-8 was that the tungsten was not etched completely in the SF₆ RIE. The variability in the tungsten etch rates also supported that hypothesis. The average etch rate of tungsten in SF₆ came out to be 67 nm/min and the tungsten was etched for 14 seconds in SF₆ which was a 50% over-etch. The PMMA left after 14 seconds of SF₆ RIE would

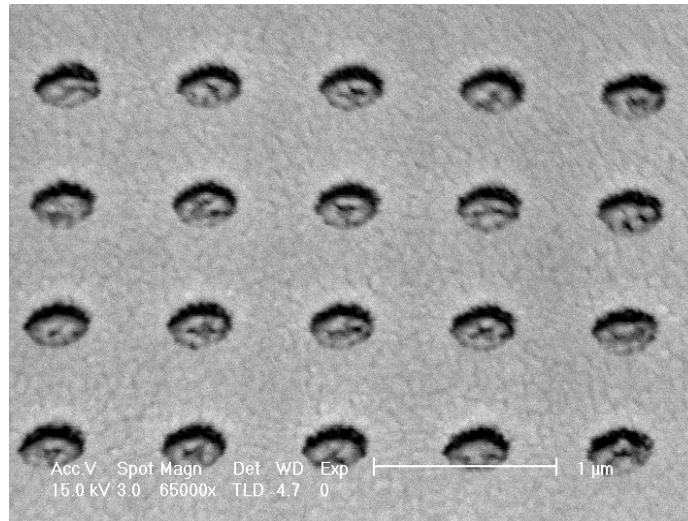
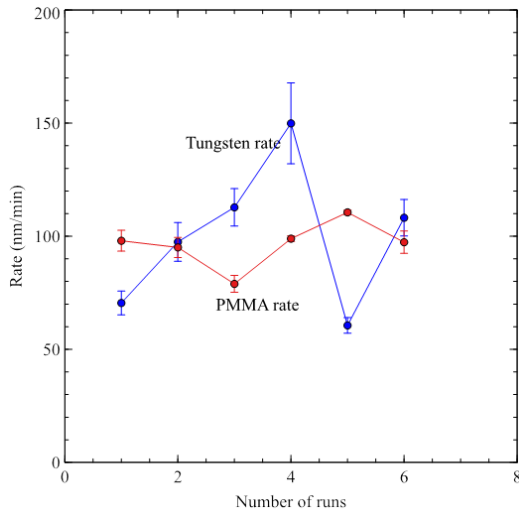


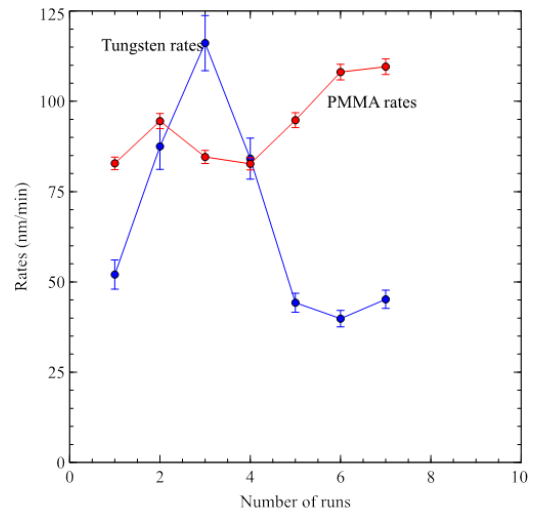
Figure 3.34. SEM image of front side of SU-8 mask with 700 nm circles tilted at an angle of 30 degrees.

be around 75 nm/min. However if we hypothesize that the tungsten rate was 40 nm/min, which was the lowest among all the measured rates, then after 14 seconds of etching the tungsten in SF₆, the thickness of tungsten etched would be around 9 nm as shown in step one of [Figure 3.36](#). Hence it would lead to an incomplete tungsten etching with 1 nm tungsten still un-etched. The next step was a short 30 seconds Ar milling step in order to sputter the 1 nm thick nichrome adhesion layer. But since there was 1 nm of tungsten left over, the 30 seconds of Ar milling would etch another 0.5 nm of tungsten since the tungsten sputter rate in Ar is around 1 nm/min at 200 V energy. Hence, we would be left with approximately 0.5 nm thick tungsten and the 1 nm nichrome as shown in step two of [Figure 3.36](#).

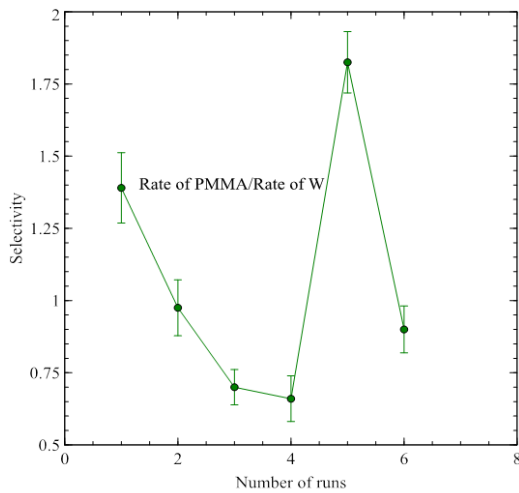
We had already estimated that the total thickness of SU-8 etched was 220 nm. The 250 nm thick SU-8 was etched for a 50% over-etch in oxygen and the SU-8 rate in oxygen RIE came out to be 120 nm/min implying that it takes around 3 minutes and 50 seconds to etch 250 nm thick SU-8 with a 50% over-etch and the oxygen RIE was run for that length of time. However, it takes 1 minute and 50



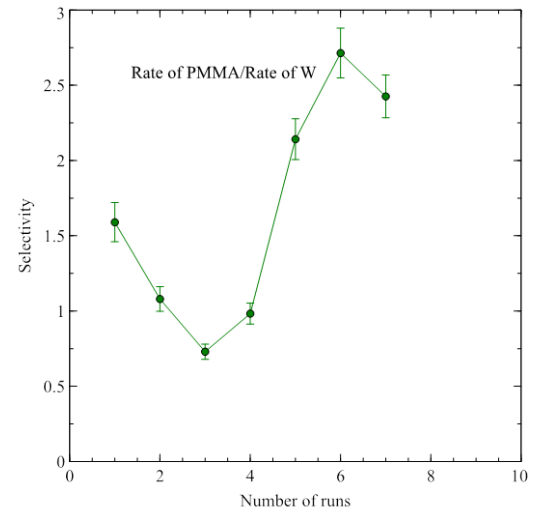
(a)



(b)



(c)



(d)

Figure 3.35. (a) Rate of PMMA and tungsten in SF₆ RIE at 15 W (b) Rate of PMMA and tungsten in SF₆ RIE at 15 W for another set of experiments (c) Selectivity between PMMA and tungsten in SF₆ RIE at 15 W for (a) (d) Selectivity between PMMA and tungsten in SF₆ RIE at 15 W for (b).

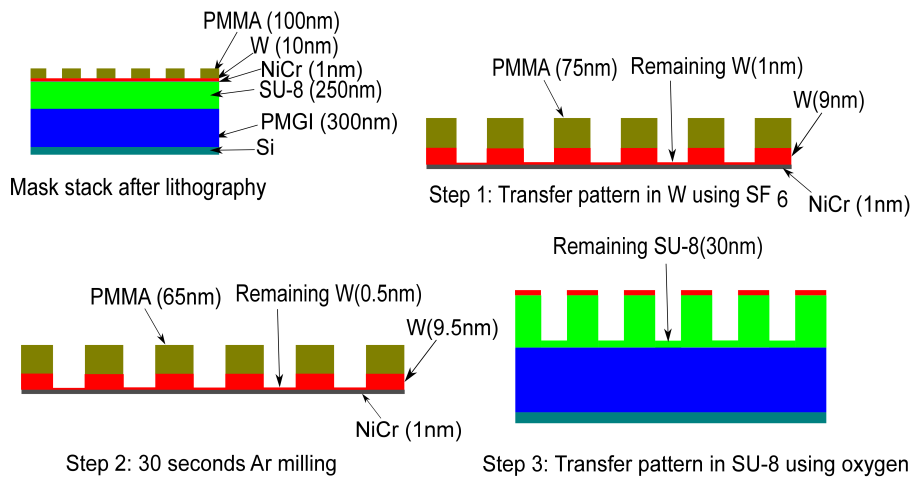


Figure 3.36. Schematic diagram of the step by step process flow demonstrating the SU-8 etch slowdown.

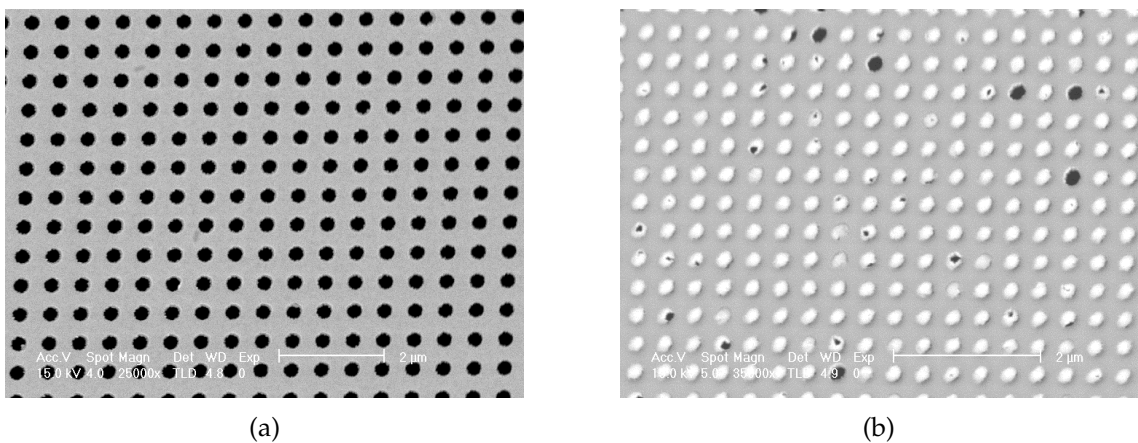


Figure 3.37. SEM image of back side of a SU-8 mask with (a) 200 nm circular patterns (b) 300 nm circular patterns.

seconds to etch 220 nm of SU-8 at 120 nm/min and therefore the first two minutes of oxygen RIE was consumed in sputtering the 1.5 nm thick layer of un-etched tungsten and nichrome. Therefore after the oxygen RIE we were left with around 30 nm of un-etched SU-8 as shown in step three of [Figure 3.36](#). Our hypothesis that the tungsten rates varies in SF₆ and that this particular mask sample saw the lowest tungsten etch rate supports the observation of the incomplete etching of the SU-8 mask.

Further two mask samples were etched with the same recipe as the one shown in [Figure 3.34](#). The SEM images of the back side of the mask are shown in [Figure 3.37\(a\)](#) and (b) where we see that in [Figure 3.37\(a\)](#) the mask is completely etched all the way through implying that in that particular run, the tungsten rates were nearly equal to or higher than the average estimated rate of 67 nm/min. It must be notified that the oxygen RIE for both these results were run at a 250% over-etch for 7 minutes. But as seen in [Figure 3.37\(b\)](#), the mask did not etch all the way through and the bright secondary electron signal on the back side confirms that there was un-etched material left even after a 250% over-etch into the SU-8. This can also be hypothesized that the tungsten rates varied for the result in [Figure 3.37\(b\)](#) as opposed to the one in [Figure 3.37\(a\)](#) since both these samples were run exactly for the same process times. Since a 250% over-etch of the SU-8 in oxygen did not etch the SU-8 all the way through, we can assume that the tungsten rates for this particular experiment was equal to or even lower than the lowest measured rate of 40 nm/min. That would lead to the similar outcome as shown in the three steps of [Figure 3.36](#) and also explained in the previous paragraph.

[Figure 3.38\(a\)](#) shows the SEM image of the back side of the SU-8 mask with 1 μm circles after 500% over-etch into the SU-8 where we can see that the mask is completely etched. A 500% over-etch was carried out in the SU-8 using oxygen plasma which consumed no more than 6 nm of tungsten. [Figure 3.38\(b\)](#) show the back side SEM images of the mask with 200 nm by 3 μm rectangles after 500% over-etch into the SU-8 with the same etch recipe as used in [Figure 3.34](#) and [Figure 3.37\(a\)](#) and (b). We can observe that the patterns are etched all the into the SU-8 as there are no secondary electron signals coming out of the etched openings implying that the etching into the SU-8 was with high fidelity.

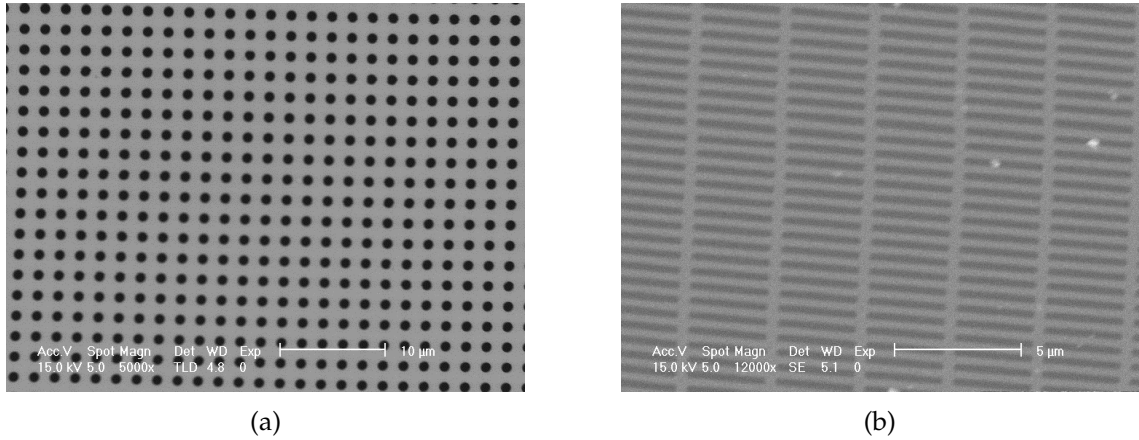


Figure 3.38. SEM image of (a) back side the SU-8 mask with e-beam written 1 μm circles after 500% over-etch into SU-8 (b) back side the SU-8 mask with e beam written 200 nm by 3 μm rectangles after 500% over-etch into SU-8.

3.3.2.3 Formation of a second image in the atom beam lithography tool

One major challenge we encountered was that we observed the formation of a second image in the etched features as shown in the SEM images in [Figure 3.39\(a\)](#) and (b) where 1 μm circles were etched into SU-8. The patterns were printed in PMMA using atom beam lithography and were transferred into copper and gold using argon milling and etched into SU-8 using oxygen plasma. The second image had certain offset in both x and y directions relative to the primary image as shown in [Figure 3.39\(a\)](#) and (b). Since we print with only helium atoms and the ions are deflected away by the deflector plates, the formation of the second image could come from particles reflecting off the beam column.

We measured the offset of the second image in the x and y direction which came out to be 6.5 μm and 2.5 μm respectively, implying that the resultant shift in the second image relative to the primary image was around 7 μm . The patterns were printed at a gap of approximately 100 μm between the mask and the substrate and radius of the beam column was 5 cm. Based on these measurements and using the schematic diagram in [Figure 3.40](#) we calculated the position of the beam

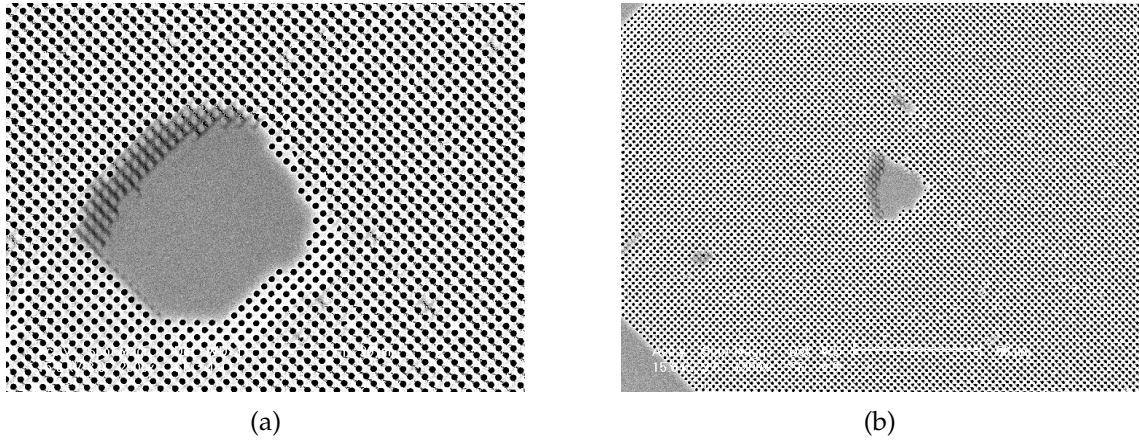


Figure 3.39. SEM image of (a) etched features showing a second image in high magnification (b) etched features showing a second image in low magnification.

column from where the reflected particles appeared to originate. Using two similar triangles, the height of the reflected particles came out to be around 70 cm from the mask, which was somewhere around the center of the beam column. Using these calculations, we estimated that the second particle beam originated near the source as shown in [Figure 3.41\(a\)](#) and reflected off the beam column before reaching the substrate. We overcame this challenge by installing a shielded aperture near the source that blocked the second beam as shown in [Figure 3.41\(b\)](#) and observed that the subsequent prints with the tool did not give rise to a second image as seen in the SEM images of [Figure 3.42\(a\)](#) and (b).

3.4 Conclusion

We have carried out stencil masks of PMMA and SU-8 in our lab of varying thicknesses. The PMMA stencil masks had the simplicity in its fabrication process and the patterns were formed from the e-beam exposure rather than etching them and transferring them into underlying substrates. But the downside was our ability to control the PMGI undercut and the evaporation of gold on the membrane as the PMMA re-flowed due to the temperature getting above its glass

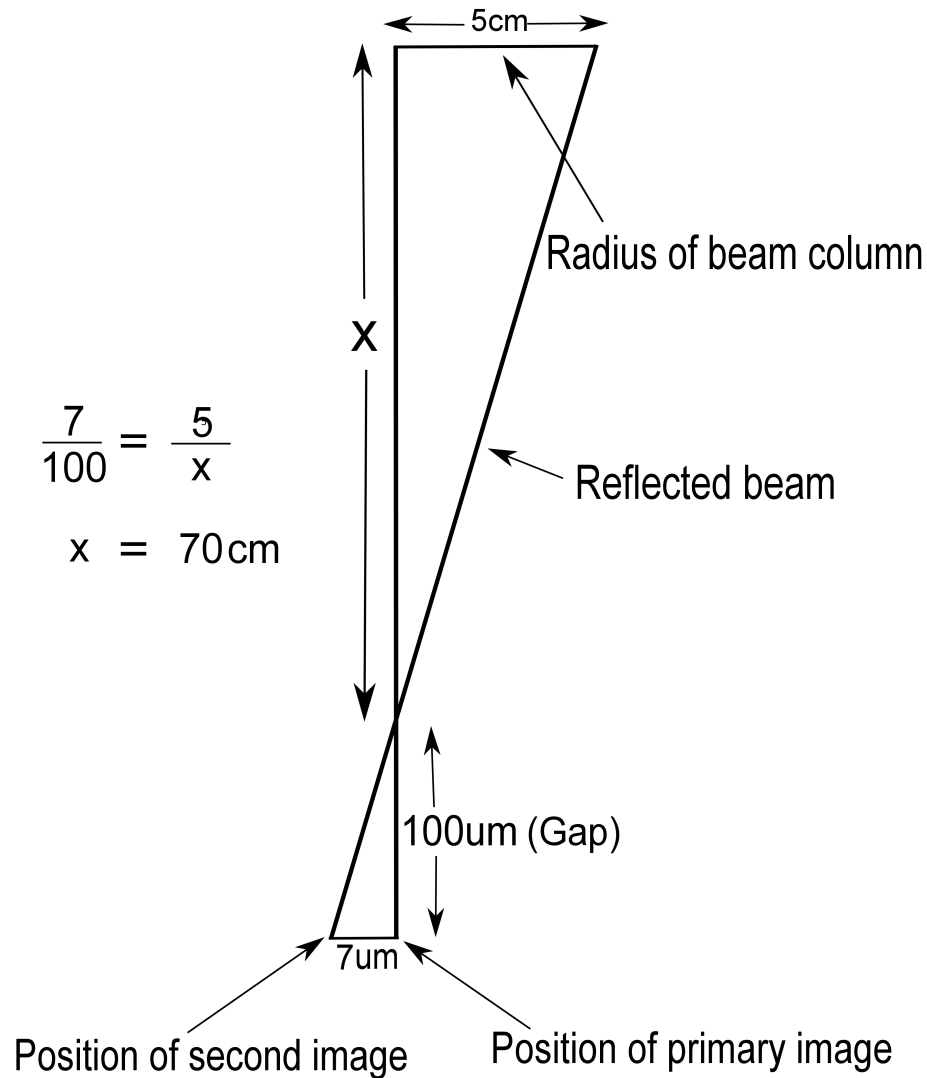


Figure 3.40. Schematic diagram of the analysis of the second image formation in the atom beam lithography tool.

transition temperature. Therefore, the process showed a lot of promise but was abandoned due to challenges in reproducibility. The SU-8 stencil masks were more mechanically robust than PMMA membranes, even when only 250 nm thick. But the first fabrication process involving milling the patterns into the copper had the drawback of increasing in the linewidth by 80 nm. This we hypothesized that this is due to the ion milling step. Therefore, a new process, where plasma etching the patterns into tungsten as the hard mask, showed more promise than the copper

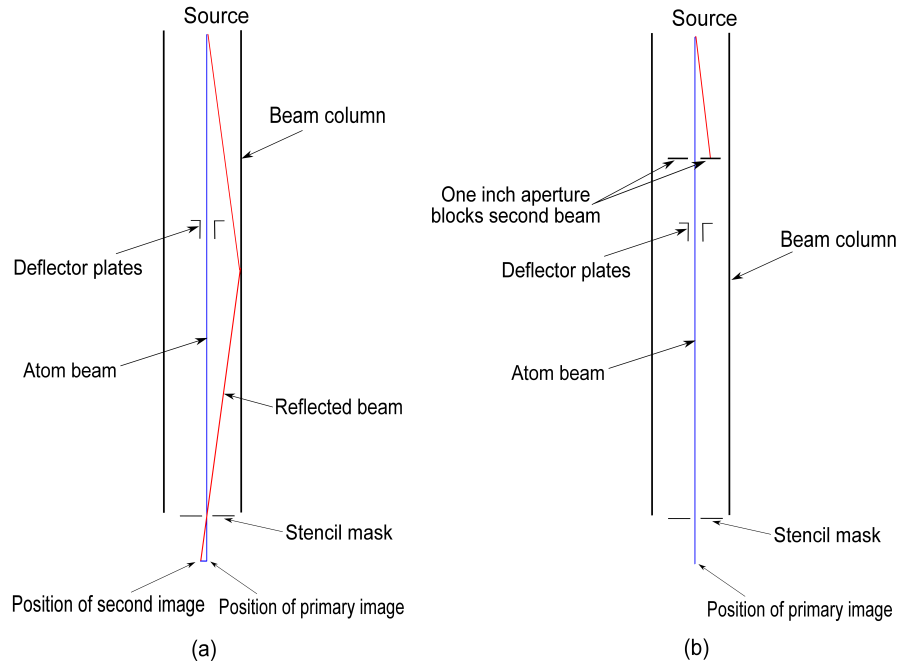


Figure 3.41. Schematic diagram of the (a) reflected second beam originating from the source in the atom beam lithography tool and (b) one inch aperture blocking the second beam and second image.

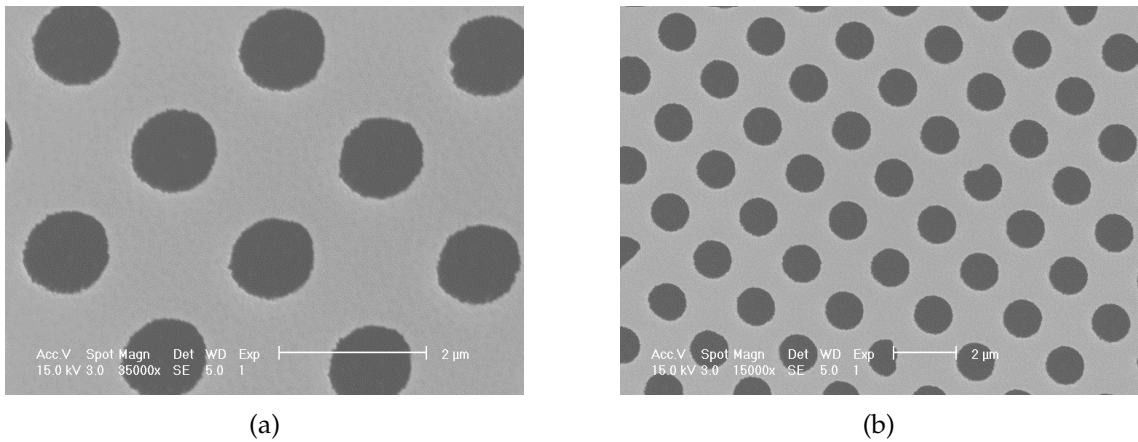


Figure 3.42. SEM image of (a) printed features in atom beam lithography after shielding the second image in high magnification and (b) in low magnification.

milling process. But this process had a downside of the varying tungsten rates in SF_6 RIE and therefore it needed either an aggressive over etch of 500% into the SU-8 to etch the patterns all the way or an increase in the tungsten etching process from a 50% over-etch to a 100% over-etch in SF_6 which we haven't tried in

these experimental runs yet. Also, monitoring the exact tungsten rates in SF₆ by introducing witness samples of tungsten in the course of the actual mask etching steps could be an alternative to overcome this limitation of the varying tungsten rates. Hence, as per the results and discussions and analysis done, we can conclude the 250 nm SU-8 stencil masks using tungsten as the hard mask material are the best choice so far based on the yield of the process and the resolution of the patterns we can expect from these stencil masks and also based on our ability to print those patterns faithfully using the helium atom beam lithography with a small gap of 50 to 100 μm.

Chapter 4

Summary and Future Work

In this dissertation, we have described the development of robust, free-standing SU-8 membranes with thickness varying between 250 nm and 1000 nm and with 0.5 cm² area. These membranes were developed for two separate applications, the first addressing the need for nanopantography lenses that could be placed directly against a conducting surface, allowing a large variety of substrates to be patterned using this technique. The second application was to develop stencil masks for printing nano-scale features by atom beam lithography. For both of these, we developed an anisotropic RIE process for transferring patterns through the SU-8 membrane using a metal hard mask that served to provide the selectivity needed to etch through the membrane and also served as a conducting film for the nanopantography lenses.

Initially, a SF₆ plasma etch process was explored, as it showed excellent selectivity between copper, which we proposed to use as a hard mask and electrode material, and the underlying polymer. However, this etch left behind a sidewall deposition, and was replaced with an oxygen etch process. During the switching between the etch gasses, we discovered that the etch chamber was conditioned by the SF₆ process to subsequently provide high selectivity when running the oxygen plasma, and so the two processes were integrated to allow for the formation of both nanopantography lenses and stencil masks.

We successfully manufactured reusable, mechanically robust nanopantogra-

phy lenses with free-standing 1 μm thick SU-8 membranes using an oxygen RIE process with a copper hard mask and gold electrode that sustained potentials greater than 80 V, and also demonstrated nanopantography using the free-standing membranes. We used silver paint to paint the sidewalls of the acrylic frame and the gold electrode to make proper electrical connections to the membrane and while carrying out nanopantography, we had to place the membranes on the silicon substrate while ensuring that they do not tear or rupture during that process. We used SU-8 as the lens dielectric over other polymers like PMMA and PMGI because of its high dielectric strength and its robustness as a free-standing membrane.

For the nanopantography lenses, we characterized the current-voltage breakdown characteristics of dielectric prior to releasing them from the substrate as well as free-standing nanopantography lenses. We applied a lens potential up to 100 V by ramping up the voltage and observed that for the lenses fabricated on the substrate, breakdown occurred at a potential between 80-90 V, and for the free-standing membranes, the leakage current remained around 50 nA even at a potential of 150 V. The reason why the membranes had a lower leakage current was that they did not make 100% contact with the substrate and hence many of the defected areas on the membrane surface did not make contact with the substrate and they survived the breakdown test with a much lower leakage current. Therefore, we concluded that the free-standing membranes were better suited to withstand the higher lens potentials.

We developed a model for the nanopantography process using the commercial simulation tool SimIon and demonstrated nanopantography using reusable lenses made of SU-8 membranes can etch features as small as 30 nm using 1 μm lens diameters which agreed with the measured results. Smaller lens diameters (300 nm and 500 nm), also with a 1 μm thick dielectric layer, were also simulated, and each simulation computed the distribution of the ions at the base of the lens as

a function of the lens potential to determine the smallest size of the feature that could be formed and the sensitivity to the focusing potential. The smallest spot size possible with 1 μm diameter lenses is about 30 nm, which is about three times larger than the aberration-free thin lens model. The experimental results with the 1 μm diameter lens agreed with the simulation model when 30 nm features were successfully etched into silicon as predicted by the model. The ion energy was based on measurements of the system and was 67 eV with a 3.5 eV FWHM. Using simulations we are able to predict that it is possible to etch features as small as 15 nm and 20 nm with lower numerical aperture lenses of 300 nm and 500 nm diameters respectively.

In order to manufacture the nanopantography lenses, we needed stencil masks to print the lens patterns using the helium atom beam lithography tool. Our stencil mask process started with 500 nm thick PMMA membranes. These had the simplicity in terms of the fabrication process but suffered from drawbacks. The main downside was our ability to control the PMGI undercut and the evaporation of gold on the membrane as the PMMA re-flowed due to the temperature getting above its glass transition temperature. Therefore that process showed a lot of promise but was abandoned due its unreliability. We shifted to developing lithography stencil masks using 500 nm thick SU-8 membranes which were mechanically robust and had the same manufacturing process as that of the nanopantography lenses using copper as the hard mask. But in order to etch sub 100 nm features and to overcome the aspect ratio RIE, we reduced the thickness of the SU-8 to 250 nm and successfully manufactured stencil masks of varying features.

We successfully printed features of approximately 100 nm using the stencil masks in the atom beam lithography tool. However, the pattern transfer into the copper using Ar milling required 1:1 selectivity between PMMA and copper, which was not reproducible and resulted in low process yield. This was attributed

to humidity fluctuations in the cleanroom, which were beyond our control. To improve the robustness of the process, we transitioned to a tungsten hard mask that is less sensitive to humidity fluctuations in our facilities and does not suffer from linewidth broadening, which was observed in the copper process. We have demonstrated that openings as small as 50 nm could be etched in the stencil masks with high fidelity using tungsten as the hard mask that overcomes the linewidth broadening problem associated with the previous process involving argon milling of copper. We also successfully eliminated a second image formation using the atom beam lithography tool. A second image was seen at an offset of 7 μm from the primary image. We calculated the height of the reflected second beam to be 70 cm from the mask and we installed a one inch shielded aperture below the deflector plates to eliminate the second image as was seen from the subsequent prints.

The nanopantography simulation results showed that by reducing the lens diameter to 300 nm and 500 nm and thereby reducing the numerical aperture we can obtain etched features as small as 15 to 20 nm. The future goal is to develop nanopantography lenses of 300 nm diameter using tungsten as the lens electrode and etch 15 nm features using these smaller diameter lenses and demonstrate that the experimental results are in agreement with the simulation results. One of our other goals is to develop a second generation stencil mask process using tungsten as the hard mask and with 250 nm thick SU-8. In order to overcome the variability in the tungsten rates we can either introduce test samples of tungsten during the course of the actual mask RIE and increase the tungsten RIE to a 50% over-etch. The other future goal to consider would be developing second generation stencil masks by patterning with the first generation stencil masks using the atom beam lithography tool. The patterns in the first generation masks would be replicated in the second generation masks with high fidelity and the resolution of the features

in the second generation masks would also be studied and analyzed in future works. Finally, printing sub 100 nm features with the second generation masks using the helium atom beam proximity printer would summarize this work in the future.

References

- [1] L. Xu, D. J. Economou, V. M. Donnelly, and P. Ruchhoeft, "Extraction of a nearly monoenergetic ion beam using a pulsed plasma," *Applied Physics Letters*, vol. 87, no. 4, p. 041502, 2005.
- [2] L. Xu, A. Nasrullah, Z. Chen, M. Jain, P. Ruchhoeft, D. J. Economou, and V. M. Donnelly, "Etching of nanopatterns in silicon using nanopantography," *Applied Physics Letters*, vol. 92, no. 1, p. 013124, 2008.
- [3] S. Tian, V. M. Donnelly, P. Ruchhoeft, and D. J. Economou, "Sub-10 nm nanopantography," *Applied Physics Letters*, vol. 107, no. 19, p. 193109, 2015.
- [4] S. Tian, V. M. Donnelly, and D. J. Economou, "Transfer of nanopantography-defined patterns using highly selective plasma etching," *Journal of Vacuum Science & Technology B, Nanotechnology and Microelectronics: Materials, Processing, Measurement, and Phenomena*, vol. 33, no. 3, p. 030602, 2015.
- [5] J. Randall, D. Flanders, N. Economou, J. Donnelly, and E. Bromley, "Silicon nitride stencil masks for high resolution ion lithography proximity printing," *Journal of Vacuum Science & Technology B: Microelectronics Processing and Phenomena*, vol. 1, no. 4, pp. 1152–1155, 1983.
- [6] J. Randall, D. Flanders, N. Economou, J. Donnelly, and E. Bromley, "Masked ion beam resist exposure using grid support stencil masks," *Journal of Vacuum Science & Technology B*, vol. 3, no. 1, pp. 58–61, 1985.

- [7] J. Randall, L. Stern, and J. Donnelly, "The contrast of ion beam stencil masks," *Journal of Vacuum Science & Technology B: Microelectronics Processing and Phenomena*, vol. 4, no. 1, pp. 201–204, 1986.
- [8] S. Pang, M. Geis, W. Goodhue, N. Efremow, D. Ehrlich, R. Goodman, and J. Randall, "Pattern transfer by dry etching through stencil masks," *Journal of Vacuum Science & Technology B: Microelectronics Processing and Phenomena*, vol. 6, no. 1, pp. 249–252, 1988.
- [9] P. Basu, "Optimization of reactive ion etching to fabricate silicon nitride stencil masks in SF₆ plasma," Master's thesis, 2013.
- [10] S. Sen, F.-O. Fong, J. Wolfe, J. J. Yen, P. Mauger, A. R. Shimkunas, H. Löschner, and J. N. Randall, "Fabrication of low-stress silicon stencil masks for ion beam lithography," *Journal of Vacuum Science & Technology B: Microelectronics Processing and Phenomena*, vol. 7, no. 6, pp. 1802–1805, 1989.
- [11] F.-Y. Shih, S.-Y. Chen, C.-H. Liu, P.-H. Ho, T.-S. Wu, C.-W. Chen, Y.-F. Chen, and W.-H. Wang, "Residue-free fabrication of high-performance graphene devices by patterned pmma stencil mask," *AIP Advances*, vol. 4, no. 6, p. 067129, 2014.